HOLLOW FIBRE BIOREACTOR DELAYED START-UP, PH GRADIENTS AND CHO CELL PRODUCT HARVESTING

By

YI-TA LEE

B.Eng., McGill University, 1994
M.Eng., McGill University, 1996

A THESIS SUBMITTED IN PARTIAL FULFILMENT OF
THE REQUIREMENT FOR THE DEGREE OF

DOCTOR OF PHILOSOPHY

In

THE FACULTY OF GRADUATE STUDIES

MICHAEL SMITH LABORATORIES

And

DEPARTMENT OF CHEMICAL AND BIOLOGICAL ENGINEERING

We accept this thesis as conforming
to required standard

.....

.....

.....

.....

.....

.....

THE UNIVERSITY OF BRITISH COLUMBIA

November 2004

Abstract

Hollow fibre bioreactors (HFBRs) are widely used for monoclonal antibody production. Compared to spinners inoculated in parallel, ultrafiltration HFBR start-up lags are often significantly longer and HFBRs have a higher frequency of failure. A number of potential causes of these problems were identified, including inhibitory residual by-products of the HFBR manufacturing process and the loss of the inoculum by cells settling into hypoxic manifold regions of the extracapillary space (ECS). Besides these primary effects, a number of secondary phenomena were also identified, e.g., factors released by the death of settled cells can decrease viable cell growth rates. Increased thermal degradation of L-glutamine to ammonium during the prolonged startup further contributed to decreasing cell growth. A combination of these effects can explain the higher frequency of HFBR startup failures.

Chinese hamster ovary (CHO) cells producing tissue plasminogen activator (t-PA) were cultured to tissue-like density in a HFBR. A sharp decline in the product concentration was observed after 20 days. Another t-PA producing CHO cell line was cultured in a HFBR and a similar decline in the harvest product concentration was observed when the ECS was filled with cells. The harvested product concentrations were significantly lower than the ECS concentration measured at the end of the run. Large amounts of t-PA were recovered from inside the HFBR cartridge at the end of the runs, using a cell lysis buffer and a lysine analog. These results demonstrate that mass transport can become hindered in a packed HFBR to such an extent that the ability to harvest protein product is severely compromised.

A mathematical model of HFBR mass transport was developed to describe the effects of CO_2 and lactate production on the ECS cell culture environment, in particular the pH. This mathematical model, using a set of previously reported diffusion coefficients along with some generalized assumptions for the specific lactic acid production rate (*sLPR*) and carbon dioxide evolution rate (*sCER*), predicted intracapillary space (ICS) pH levels similar to experimentally measured values. The variables that had the greatest impact on the ECS pH gradients were *sLPR*, the thickness of the ECS annulus and the ICS inlet pH. This model can therefore be a useful tool in determining the operating conditions needed to maintain a favourable pH environment in the ECS of an HFBR.

Contents

Tables

Figures

Acknowledgements

I am sincerely grateful to Dr. Bruce D. Bowen and Dr. James M. Piret for their support and guidance. They showed me the proper way to think and write. I am also extremely thankful to my parents and my sisters for their love and encouragement. Special thanks to all my colleagues in the Michael Smith Laboratories (formerly Biotechnology Laboratory) for their help and friendships. Lastly, I am indebted to my wife, Ju-Nee, the pillar of strength in my life, without whom this degree would not be possible.

Chapter 1

INTRODUCTION

Hollow fibre cartridges are widely used and have many applications. A typical hollow fibre cartridge is composed of a bundle of hundreds or thousands of polymeric membrane tubules arranged essentially parallel to each other. The bundle of tubules is sealed inside a cylindrical cartridge with the inside of each tubule, or lumen, opening to manifolds at both ends of the cartridge. The tubular membranes divide the volume inside the hollow fibre cartridge into two separate compartments: the volume outside the bundle of tubules, or extracapillary space (ECS) and the volume inside the tubules, or intracapillary space (ICS). Due to the arrangement of the hollow fibres in the cartridge, the membrane area per unit volume is relatively large (e.g. 2 x 10^4 m^2/m^3). Figure 1.1 shows a schematic diagram of a hollow fibre bioreactor cartridge.

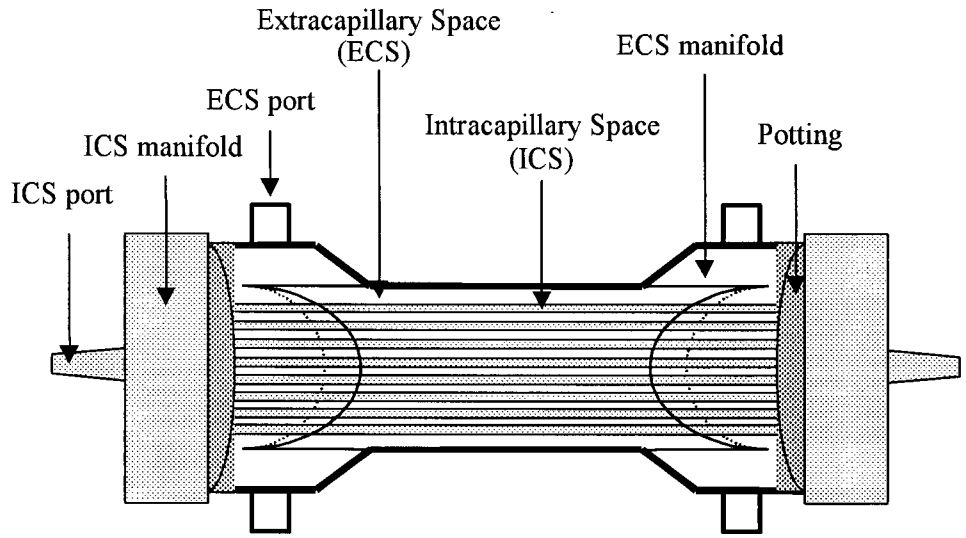

Figure 1.1 Schematic diagram of a hollow fiber bioreactor. (Note that there are thousands of fibres in an actual hollow fibre cartridge.)

Hollow fibre cartridges are commercially used in filtration and reverse osmosis processes (Breslau *et al.* 1980; Michaels 1980). For example, cartridges with permeable microporous membranes are utilized in the removal of very fine particulates during water purification (Jacangelo *et al.* 1989). Ultrafiltration membrane hollow fibre cartridges are also used for extracorporeal treatment of blood such as for hemodialysis (Colton and Lowrie 1981; Sigdell 1981; Bosch and Setin 1993), hemofiltration and hemodiafiltration (Colton *et al.* 1971; Henderson *et al.* 1986), plasma separation and fractionation (Zydney and Colton 1982; Yoshikawa *et al.* 1992) and blood oxygenation (Sueoka and Takakura 1991).

An important application of hollow fibre cartridges is their use as bioreactors, first proposed by Rony (1971) and Knazek *et al.* (1972). Specifically, hollow fibre bioreactors (HFBRs) have been used to culture mammalian cells, such as hybridoma cells (Heifetz *et al.* 1989; Evans and Miller 1990; Piret and Cooney 1990b; van Erp *et al.* 1991a; van Erp *et al.* 1991b; Handa-Corrigan *et al.* 1992a; Jobses *et al.* 1992; Kurkela *et al.* 1993; Lowrey *et al.* 1993; Lowrey *et al.* 1994; Brotherton and Chau 1995; Czirbik *et al.* 1996; Jackson *et al.* 1996), baby hamster kidney (BHK) cells (Ryll *et al.* 1990; Inoue *et al.* 1996a; Inoue *et al.* 1996b; Tanase *et al.* 1997), Chinese hamster ovary (CHO) cells (Treat *et al.* 1997; Thelwall and Brindle 1999), hepatoma cells (Liu *et al.* 1991), and lymphocytes (Knazek *et al.* 1990; Freedman *et al.* 1994; Hillman *et al.* 1994). In addition, hollow fibres have been utilized in biomedical applications as artificial organs, such as the bioartificial pancreas (Chick *et al.* 1975; Jaffrin *et al.* 1988; Pillarella and Zydney 1990) and the bioartificial liver (Shatford *et al.* 1992; Li *et al.* 1993; Nyberg *et*

al. 1993; Rozga *et al.* 1993; Bader *et al.* 1995; Catapano 1996; Sheil *et al.* 1996; Wu *et al.* 1996; Ohshima 1997; Takagi *et al.* 1997).

The usefulness of mammalian cell HFBRs in producing diagnostic and biopharmaceutical products has motivated many experimental and theoretical studies to better understand the conditions inside the hollow fibre cartridge and to improve the overall productivity of the process. Within the ECS of HFBRs, where the cells are normally cultured, there are significant nutrient and metabolite gradients (Waterland *et al.* 1975; Vilker *et al.* 1981; Piret *et al.* 1991). This discovery has led to many theoretical models describing the mass transfer, hydrodynamics, and cell growth within HFBRs, e.g. solute transport in the ECS (Noda and Gryte 1979), convective and diffusive transport (Ross 1974; Ma *et al.* 1985; Salmon *et al.* 1988), hydrodynamic analysis (Bruining 1989; Labecki *et al.* 1995), time-dependent transport of glucose and insulin (Pillarella and Zydney 1990), oxygen limitations (Piret and Cooney 1991), membrane porous medium (Yoshikawa *et al.* 1992), protein transport in the ECS without the presence of cells (Taylor *et al.* 1994; Patkar *et al.* 1995; Labecki *et al.* 1996), protein transport in the ECS in the presence of cells (Koska *et al.* 1997), and transient growth of cells in the ECS (Kumar and Modak 1997).

One of the recognized but not widely published problems encountered in the production of recombinant proteins and antibodies in HFBRs is the delayed start-up of cell growth and, in some instances, complete failure to establish a viable culture. Thus, one of the primary aims of the research proposed here is to identify and investigate factors causing the delayed start-up and to attempt to eliminate these factors. In addition, factors affecting the subsequent harvesting of recombinant proteins from cell-packed HFBRs

will be studied. Finally, pH gradients in HFBRs, created by the generation of carbon dioxide and lactic acid from the cells in the ECS, will be assessed using mathematical model simulations. Armed with a better understanding of the factors influencing the lag-phase, the ability to harvest product proteins and the maintenance of appropriate pH conditions, the overall productivity of HFBRs could be significantly improved.

The overall goals of this project therefore are to identify factors that affect cell growth in HFBRs and to determine operating conditions that will help improve HFBR protein production. Chapter 2 begins with a review of previous work in the areas specific to these topics. The specific objectives of identifying factors that can cause a prolonged start-up in HFBRs and developing means to improve the growth and productivity are discussed in Chapter 3. Investigations on the impact of packed cell density on product harvest and the effectiveness of culturing Chinese hamster ovary (CHO) cells in HFBRs are presented in Chapter 4. Chapter 5 presents a theoretical model of pH distribution in HFBRs, which could be used as a quantitative tool to further improve their operating conditions. Finally, the last chapter contains the conclusion and outlines possible future extensions of this work.

Chapter 2

BACKGROUND AND PREVIOUS WORK

The objectives of this chapter are two-fold. The first is to provide the background necessary to understand the challenges offered by culture variables that can influence the performance of HFBR cultures. The second objective is to discuss the transport of chemical species that affect the distribution of pH in cell-packed HFBRs.

2.1. Hollow Fibre Mammalian Cell Culture

2.1.1. Cell Types

Mammalian cell types can be grouped into two categories: anchorage dependent and anchorage independent. Anchorage-dependent cells require a surface substrate for attachment and growth; while anchorage-independent cells are able to grow in suspension without a surface for attachment. Fibroblast and epithelial cells are commonly used anchorage-dependent cells while lymphoblast and haematopoietic cells are typical anchorage-independent cells (Butler and Dawson 1992). Chinese hamster ovary (CHO) cells, derived from partially inbred female adult Chinese hamsters (Puck *et al.* 1958), are frequently used in recombinant protein production. Another widely used cell line for recombinant protein production is the NS0 cell, which was derived from plasmacytoma cells. HeLa cells, a type of human cervical cancer cell, are mostly used in research. Baby hamster kidney (BHK) is a type of fibroblast cell used for the production of clotting

factors and veterinary vaccines (Ryll *et al.* 1990; Griffiths and Racher 1994; Inoue *et al.* 1996b; Jurlander *et al.* 2001). Vero are African green monkey kidney cells used to produce polio and rabies vaccines (Montagnon 1985; Montagnon 1989). Many anchorage-dependent cells, under typical cell culture conditions, grow to form adherent monolayers. As a result, systems having large surface to volume ratios, such as micro-carriers, ceramic bioreactor, and hollow-fibre modules, can be useful devices for cultivating anchorage-dependent cells (Griffiths 1986; Griffiths 1990). Some anchorage-dependent cells can also grow in multilayers (Tharakan and Chau 1986) or form aggregates or clumps which allow them to be grown in suspension (Cartwright 1994).

Non-primary cell lines are usually transformed such that their phenotypes change due to heritable changes in the genome and gene expression. Transformed cell lines are usually immortal (where in theory they can be cultivated *ad infinitum* under proper conditions). These transformed cell lines tend to grow at faster rates, have less stringent growth requirements, and lose their anchorage-dependence and contact inhibition. Finally, transformed cells can be tumourigenic (Freshney 1994). Hybridoma cells are transformed since they result from the fusion of an antibody-producing B lymphocyte and a myeloma cell (Kohler and Milstein 1975). Hybridoma cells are the most commonly used in HFBR cultures. They are anchorage-independent though some do attach to surfaces when in contact.

2.1.2. Extracellular Matrix

Extracellular matrix (ECM) is a mixture of proteins and carbohydrate-rich molecules that provides a static, structural support for cells. ECM is a critical component in the formation and differentiation of most tissues *in vivo* (Keehan *et al.* 1990; Ashkenas *et al.* 1996) Most cells in mammalian cell culture produce and deposit ECM. Transformed cells usually have a decrease in the amount of ECM produced per cell, and, as a result, can have reduced anchorage-dependence (Ashkenas *et al.* 1996). Three major components of ECM are collagens, which form insoluble protein fibrils; glycoproteins, such as fibronectin, vitronectin, and laminin, which are conjugated protein molecules in which the non-protein group is a carbohydrate; and proteoglycans, composed mostly of polysaccharides known as glycosaminoglycans, bound to a core protein (Barnes 1984; Keehan *et al.* 1990). Glycosaminoglycans have a net negative charge and, as a result, bind mainly cations and large amounts of water. In connective tissue, the glycosaminoglycans act as shock absorbers for tissues *in vivo* (Junqueira *et al.* 1986). Fluid flow through solid tissues was found to obey Darcy's Law, such that a linear relationship exists between the flow rate and the applied pressure gradient. In addition, Swabb *et al.* (1974) reported that the glycosaminoglycan content relates directly to the hydraulic permeability of the tissue. The combined effects of collagen fibrils, glycosaminoglycan, and the proteoglycan core proteins account for the main fluid flow resistance and the low hydraulic permeabilities of most tissues (Levick 1987).

Based on their harvest data, Ryll *et al.* (1990) reported that protein yields from HFBR cultures of baby hamster kidney (BHK) cells decreased with time, and hypothesized that the packing of cells became so extreme in the ECS that the ability to harvest the protein

product became compromised. In mathematical model simulations, it was shown that, when a culture grows to packed-cell density, with cells and ECM filling the ECS volume, the product protein becomes difficult to harvest using standard procedures (Koska *et al.* 1997). Although packed-cell densities similar to those of solid tissues *in vivo* are typically observed in hybridoma HFBR cultures, they do not produce ECM, probably explaining why problems with hybridoma product recovery have not been reported.

2.1.3. Growth Requirements

Nutrients and metabolites

The nutritional requirements of cells *in vitro* differ considerably from the nutritional requirement of cells *in vivo*. In bioreactors, the availability/transport of nutrients to the cells can become an important factor which influences cell growth. Some of the essential nutrients required for mammalian cell culture are oxygen, carbohydrates, amino acids, lipids, fatty acids, vitamins, salts and trace elements (Freshney 1994). Oxygen, glucose, and L-glutamine are the three nutrients most consumed by transformed cells. Glucose is metabolized to provide both energy and a carbon source. The amino acid L-glutamine is the primary source of nitrogen, as well as a source of carbon and energy (Pardridge *et al.* 1978). For both oxygen and glucose, the range of uptake rates by mammalian cells has been reported to be $0.16\text{-}4.7\text{x}10^{-10}$ mmol $cell^{-1}$ h^{-1} (Henzler and Kauling 1993). L-glutamine is utilized at a rate 5 to 10 times higher than other amino acids (Butler *et al.* 1983), but at a third to a quarter of the glucose utilization rate (Adamson *et al.* 1987; Davis *et al.* 1991). Oxygen, as an essential nutrient, functions as a terminal electron acceptor in the electron transport chain and, as such, serves as a driving force for energy

production via oxidative phosphorylation. For animal cells, a major concern is to provide sufficient oxygen in the culture environment. Also, the optimal condition for cell growth can be different from that for optimal protein production. For example, the optimal dissolved oxygen tension for hybridoma cell growth has been reported to be 50-60% of air saturation, while the maximum monoclonal antibody production was obtained at 25% air saturation (Reuveny *et al.* 1985; Ryan *et al.* 1994).

The cellular metabolic waste products and their inhibitory effects vary depending on the cell line, type of medium used, and other cell culture conditions (Piret and Cooney 1990b). The metabolites produced at the highest rates are lactic acid, ammonia and CO_2 (Thomas 1990). Lactic acid is mainly converted from glucose since the rate of utilization of the glycolytic intermediates is less than the rate of glycolysis (Zeilke *et al.* 1984; Batt and Kompala 1989). Lesser amounts of lactic acid are produced from L-glutamine metabolism (Zeilke *et al.* 1984). Lactic acid can inhibit cell growth by medium acidification, but lactate inhibition has also been observed in a constant pH environment (Ozturk *et al.* 1992). Chresand *et al.* (1988b) reported that 10 mM sodium lactate decreased the growth of Ehrlich ascite tumor cells by approximately 50%, and they suggested that the build-up of lactate in HFBR cultures would become inhibitory. However, it has also been reported that a hybridoma cell line can tolerate lactate levels of 40 mM without any growth-inhibitory effects (Glacken *et al.* 1988), but with a 25% decrease in the cell specific monoclonal antibody production rate (Glacken 1987).

Ammonia is mainly produced by the deamination of L-glutamine to form L-glutamate. It was reported that cell specific antibody production rates were decreased by 50% at an

ammonium ion level of 10 mM (Glacken 1987). Other studies have reported that antibody production rates were not affected by ammonium concentrations up to 4 mM (McQueen and Bailey 1990; Ozturk *et al.* 1992). Ammonium, in the range of 2-10 mM, was observed to inhibit hybridoma cell growth by approximately 35%, due to changes in the intracellular pH (Ozturk *et al.* 1992). It should be noted that the reported discrepancies concerning the inhibitory effects of metabolites are likely due to the differences between individual hybridoma cell lines.

Serum supplements

Growth media for mammalian cells have traditionally contained fetal bovine serum (FBS). The major function of FBS is to stimulate cell growth and other activities by providing the cells with carrier proteins (e.g. albumin or transferrin), binding factors (required by anchorage-dependent cells), growth factors (e.g. interleukin-2), and hormones (e.g. insulin) (Jager 1991). FBS enhances cell attachment by providing proteins such as collagen and fibronectin. It has also been reported that serum can increase the apparent specific growth rate by acting as a shear-protecting agent that decreases the rate of cell death (Ozturk and Palsson 1991). Other benefits of serum include reduction of pH fluctuations due to its buffering capacity, neutralization of toxic heavy metals, and binding to proteases (Cartwright 1994). Despite these benefits, the use of serum has several drawbacks. Serum is an expensive medium component with considerable lot-to-lot variability. The presence of serum proteins and peptides also greatly complicates downstream processing. Contamination with viruses, prions, and mycoplasma results in potential safety problems (Brown 1987; Freshney 1994). Although, for ultrafiltration membrane HFBRs, the use of serum is largely confined to

the ECS, the addition of serum to the ICS can also be needed to compensate for the lower molecular weight serum components that leak through the membrane from the ECS to the ICS (Gramer and Poeschl 1998).

pH and temperature

The viability and productivity of a culture is dependent on the proper setting and control of pH and temperature. The optimal pH range for transformed mammalian cells is approximately 7.0-7.4 (Eagle 1973). pH values below 6.8 are usually inhibitory to cell growth (Griffiths 1986), though a suboptimal growth pH may increase specific antibody production (Miller *et al.* 1988; Handa-Corrigan *et al.* 1992a). Some hybridoma cells have been adapted to higher pH, i.e. 7.7, eventually reaching maximal growth and antibody production rates (Miller *et al.* 1988). Variations in pH are expected to occur in the culture as a result of cell metabolic activities, such as the formation of lactic acid and ammonia from glucose and L-glutamine consumption, respectively. In order to reduce the accumulation of lactic acid, the glucose concentration of the medium can be maintained at a relatively low level (Griffiths 1986).

The buffer used in the medium is another important factor that can affect the pH of the culture. For example, the pH gradients in a hollow-fibre culture of CRL-1606 hybridoma cells were shown to decrease when N-2-hydroxyethylpiperazien-N'-2-ethane sulphonic acid (HEPES) was used as the buffer instead of sodium bicarbonate (Piret *et al.* 1991). Three major strategies are used to control pH in HFBRs: the adjustment of the fraction of CO_2 delivered through the oxygenator/ventilator, the addition of a base ($NaHCO_3$ or NaOH), and the variation of the medium supply rate (Andersen and Gruenberg 1987;

Handa-Corrigan *et al.* 1992b). The main challenge lies, however, not as much in the regulation of the ICS medium pH as in the prediction, measurement, and ultimately minimisation of local pH gradients which arise in the heterogeneous environment of a hollow-fibre bioreactor ECS, especially in the presence of significant mass transfer limitations at high cell densities. Piret *et al.* (1991) reported a pH difference of 0.5 between the measured values of the ECS and ICS samples using bicarbonate buffered medium.

The temperature of the bioreactor is usually controlled in the range of 36-37°C, the typical cultivation temperature for most mammalian cells (Freshney 1994). It is important to avoid temperatures above 39°C, or hyperthermic conditions, which will result in cell death. It has been reported that a deviation from the optimal temperature, or a thermal shock, can result in increased protein production (Glacken *et al.* 1988; Kretzmer *et al.* 1998). In some cases, thermal degradation of product proteins may be reduced at lower temperature, thus leading to improved product characteristics (Mather and Tsao 1990). The bioreactor temperature can also affect the stability of nutrients in the medium; in particular, L-glutamine undergoes chemical decomposition at 37°C with a half-life of approximately one week (Ozturk and Palsson 1990). It has been suggested that the optimal operating temperature for each cell line be determined experimentally after a period of adaptation (Mather and Tsao 1990). In addition, temperature fluctuations, as a result of non-uniform heating or poor control, can influence transport phenomena in HFBRs. In particular, an approximately 2% change in fluid viscosity and solute diffusivities will result from each 1°C of temperature variation (Labecki *et al.* 2001).

2.2. Bioreactor Operation

2.2.1. Conventional System Setup

Numerous HFBR designs have been developed (Tharakan *et al.* 1988). The most commonly used design entraps cells in the ECS of a cylindrical ultrafiltration membrane cartridge while the cell culture medium recirculates through the ICS. The conventional setup of a HFBR cell culture system is shown schematically in Figure 2.1. The ICS medium is recirculated by a recycle pump through a continuous circuit composed of a bioreactor (HF cartridge), an oxygenator, and a medium reservoir. The oxygenator, located downstream of the HFBR cartridge and upstream of the ICS reservoir, aerates the ICS medium with up to 10% CO_2/balance air, to buffer the pH and to provide an adequate supply of oxygen. The sampling ports enable off-line monitoring of the pH, nutrient, and metabolite levels in the recycle stream, although commercial systems (not shown) are often equipped with probes and feedback control units to maintain temperature, pH, oxygen concentration and reservoir medium volume at specified values. The ICS medium is periodically replenished using a feed pump (Figure 2.1), and the waste medium is collected in a waste container. Low molecular weight nutrients and metabolites are exchanged between the ECS and ICS. Higher molecular weight proteins, which do not readily pass from the ECS to the ICS, are periodically supplied by pumping fresh medium into the ECS via the upstream ECS port, while the product proteins are simultaneously harvested via the downstream ECS port. Ultrafiltration membranes, having a suitable molecular weight cutoff, concentrate protein products in the ECS prior

to the product harvest. The ECS ports remain closed during operation and are opened only for harvesting. When the ECS ports are closed, an axial pressure drop in the ICS induces a secondary flow in the ECS called the Starling flow. It has been reported that ECS-retained cells and proteins accumulate in the downstream end (with respect to the ICS flow direction) due to the Starling flow (Waterland *et al.* 1975; Piret and Cooney 1990a). As a result of this polarization, the overall concentrations of serum and growth

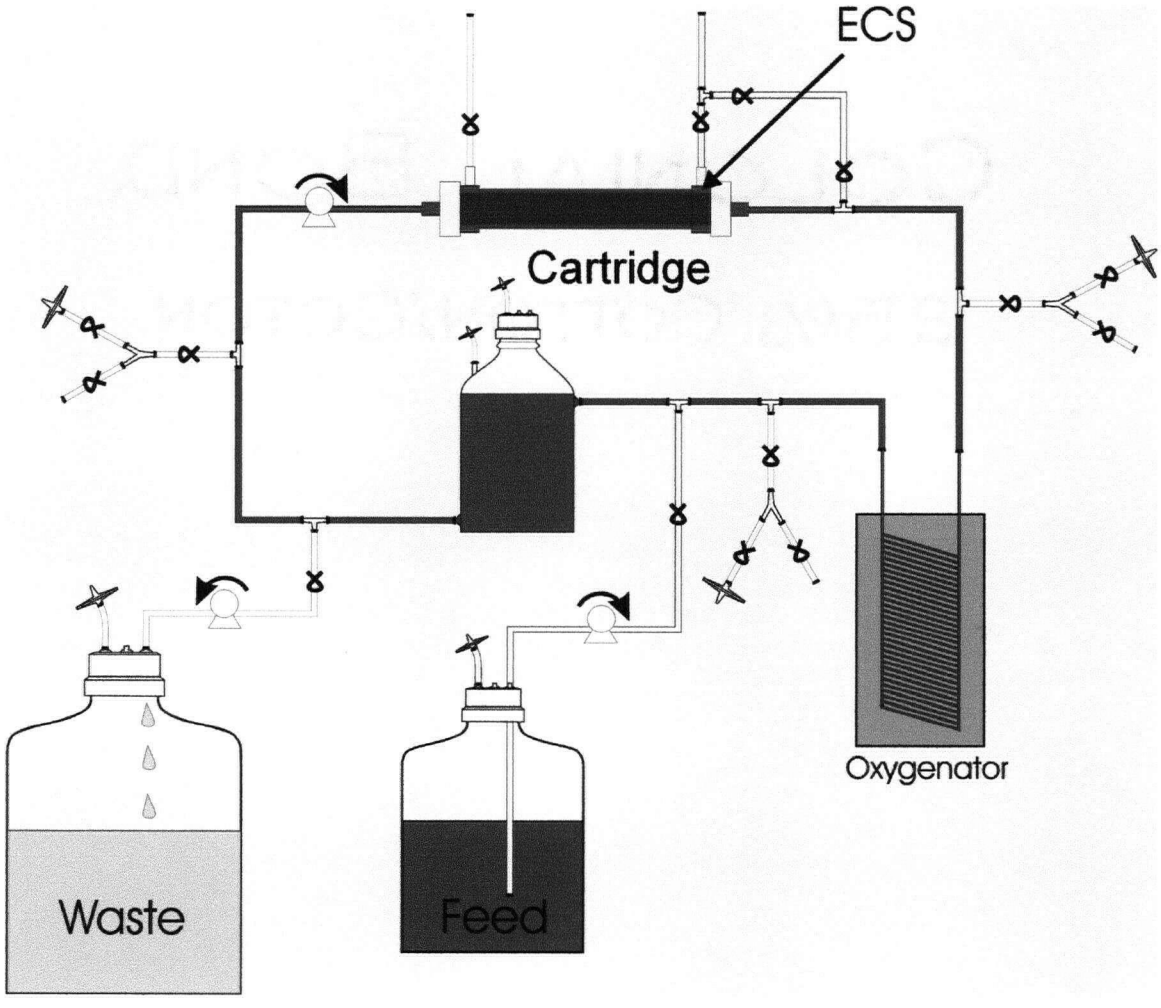

Figure 2.1 Conventional HFBR configuration (components not to scale).

factor proteins in the upstream portion of the ECS can be decreased, possibly creating regions in the HFBR where cell growth is limited. Typically, the HFBR cartridge is inclined at approximately 45° to the horizon, with the ICS flow directed upward. This flow configuration is expected to reduce the undesirable effects of downstream protein polarization and cell sedimentation (Piret and Cooney 1990a; Labecki *et al.* 1995; Labecki *et al.* 1996)

2.2.2. Inoculation

Inoculation of HFBRs is typically accomplished by suspending cells in growth medium and injecting the suspension into the ECS by means of a pump or a syringe after propagating the cells in batch culture (e.g., in t-flasks, shake flasks, roller bottles, and/or spinners). HFBR inoculation procedures can be grouped into three general categories: the standard countercurrent arrangement, the dead-end configuration, and cross-flow inoculation. In standard countercurrent inoculation, the inoculum is introduced through the downstream ECS port while the ICS medium is recirculated and the upstream ECS port is open. In this procedure, some of the inoculum cells may by-pass directly to the outlet ECS port. Dead-end inoculation introduces the inoculum via the upstream ECS port while the downstream ECS and upstream ICS ports are closed, with the downstream ICS outlet open (or vice versa). Dead-end inoculation has the advantage of retaining all of the inoculum in the ECS. In the cross-flow inoculation procedure, the cells are added through the upstream ECS port while the ICS medium is recirculated, and the downstream ECS port is closed. Cross-flow inoculation is similar to the dead-end mode,

but has the advantage of uninterrupted oxygen delivery to the ECS by the lumen-side perfusion flow.

A sufficient number of cells must be present in the ECS at the end of inoculation to ensure a successful start-up. For batch cultures, a minimum cell concentration of 10^4 to 10^5 cells mL^{-1} is usually sufficient for a successful start-up (Freshney 1994). In HFBRs, cell concentrations greater than 10^6 cells mL^{-1} ECS are usually required before start-up can be ensured. Similarly, higher inoculum cell concentrations can reduce the time required to achieve the maximum level of antibody production from HFBRs (Evans and Miller 1990). Therefore, the size of the inoculum can be an important factor in determining the length of the lag-phase, the period of time following inoculation where there is little evidence of an increase in cell number or metabolic activity (Freshney 1994).

One of the major challenges for the inoculation of conventional hollow fibre bioreactors is to uniformly distribute cells within the fibre bundle. In the standard inoculation procedure, the inoculum is pumped at a slow rate (e.g. ~5 mL min^{-1}) into one ECS port while the displaced ECS medium is collected from the other. Gravity can cause a portion of the inoculum to settle to the bottom of the bioreactor, including into the fibre-free manifold regions where the cells are exposed to deprivation of nutrients such as oxygen. Sardonini and Dibiasio (1993) have reported that many cells can become trapped in the more densely packed region of the fibre bundle near the vicinity of the inoculated ECS port. This could lead to a localization of cell growth near the ECS port and a significant reduction in the rate of filling of the remaining ECS volume. It has been suggested that these problems can be alleviated by adjusting the orientation of the HFBR cartridge, for

example by rotating the cartridge periodically or by changing the cartridge inclination angle (Piret and Cooney 1990a).

2.2.3. Closed-Shell Operation

A lag phase of several days is typically observed after inoculation. In a number of published results, 4-9 day lags in the glucose uptake of hybridoma HFBRs have been reported after inoculation (Evans and Miller 1990; Lowrey *et al.* 1994; Omasa *et al.* 1995; Czirbik *et al.* 1996; Gramer and Poeschl 1998). Similar data were published for HFBRs culturing lymphocytes and baby hamster kidney (BHK) cells where there was no observable glucose uptake for the first 5 (Lamers *et al.* 1999) to 8 (Ryll *et al.* 1990) days after inoculation. Within 2-4 weeks after inoculation, the HFBR culture typically undergoes a period of growth that slows as the ECS fills with cells. Ultimately, the HFBR culture enters the stationary phase, where the cell growth and death rates are approximately equal (Butler 1987; Freshney 1994; Pinton *et al.* 1994).

The ECS cell density during the stationary phase can reach as high as 10^9 cells mL^{-1}. The hydraulic permeability of a cell-packed ECS can decrease by much as 7-8 orders of magnitude compared with cell-free conditions (Swabb *et al.* 1974; Labecki *et al.* 1996). Also, at packed-cell densities in tissues, the effective diffusivities for small solutes such as oxygen and glucose can be reduced by a factor of 2-3 and for large solutes such as bovine serum albumin, by a factor of 25 or more (Swabb *et al.* 1974). At high cell densities, it has been reported that HFBR systems can be even more sensitive to variations in the culture parameters such as pH and nutrient/metabolite concentrations

requiring a more rigorous control of the culture conditions (Andersen and Gruenberg 1987).

The HFBR culture can be maintained in the stationary phase for months before an irreversible decline in overall cell viability occurs. This net cell death phase is likely due to the blockage of growth by accumulated nonviable cells and cell debris. There may also be ECS accumulation of high molecular weight inhibitory factors (Kidwell *et al.* 1989), which are difficult to remove from the ECS in an effective manner.

2.3. Oxygen and Carbon Dioxide Transport in HFBR

2.3.1. Krogh Cylinder Models

Most models of hollow fibre systems have been based on the assumption that the fluid and solute behaviours in the vicinity of each fibre are the same, such that a multi-fibre bioreactor can be represented by a single fibre surrounded by an annular fluid envelope (Krogh 1919). This assumption is termed the "Krogh Cylinder" approximation. In the classical theory, Krogh cylinders are assumed to contain parallel, uniformly spaced fibres with no fluid or solute exchange between them. Since the bioreactor volume is entirely and equally divided between all fibres, partial overlapping of the neighbouring Krogh cylinders is necessary to properly account for the void volumes between them. There have been studies where the void spaces have been neglected (Schonberg and Belfort 1987; Kelsey *et al.* 1990; Pillarella and Zydney 1990; Marshall *et al.* 1991), which has resulted in mass imbalances where approximately 10% of the total bioreactor volume is

not accounted for. In addition, the manifold regions of the HFBR are neglected in the Krogh cylinder model.

2.3.2. Membrane Aeration

Membrane aeration/ventilation is the commonly used method of supplying oxygen to, and removing carbon dioxide from, HFBRs. The gas diffuses through a permeable membrane, usually made of a material with high gas solubility, such as silicone. The oxygenation/ventilation units of commercial HFBR systems typically utilize such membranes arranged in the form of a coil (i.e. Cellex Acusyst® systems) or as banks of tubes (i.e. Cell-Pharm® system) with the gas on the outside and the recirculating ICS medium on the inside of the tubes.

The materials used for membrane aeration/ventilation are microporous polypropylene (PP), solid polytetrafluoroethylene (PTFE) and solid polydimethylsiloxane (silicone). In the microporous membranes, a gas-liquid interface is held stationary inside or just outside the pores of the hydrophobic membrane. For solid diffusion membranes, the gas dissolves in the hydrophobic membrane, which has no pores (Aunins and Henzler 1993).

Non-reinforced and pressure-resistant reinforced silicone tubes and silicone-coated tubular membranes are often used as aeration/ventilation membranes, as described by Miltenburger and David (1980), Fleischaker and Sinskey (1981), and Aunins *et al.* (1986). Differences in solubilities and diffusivities between oxygen, carbon dioxide, nitrogen, water, and ammonia give rise to selective permeation through the membrane. Therefore, the transfer of each gas should be considered independently. It has been suggested that

bioreactors which employ silicone tubing experience differential oxygenation and carbon dioxide ventilation. Hence, bioreactor operation requires special attention to maintain both oxygen and carbon dioxide at their optimal levels (Aunins and Henzler 1993). For example, the permeabilities of one type of silicone membrane for oxygen and carbon dioxide were determined to be 6.4×10^{-15} and 4.8×10^{-14} kg·m s^{-1} m^{-2} Pa^{-1}, respectively, at 25 °C (Robb 1968), i.e., a difference of almost an order of magnitude.

Both the membrane resistance to diffusive gas transport and the convective resistance in the proximal medium contribute to the overall mass transfer resistance (Aunins and Henzler 1993). Therefore, the overall mass transfer coefficient must take into account the liquid film mass transfer coefficient, k_L, and the membrane mass transfer coefficient, k_m, in order to predict the oxygen and carbon dioxide transport rates in aerators/ventilators. For internal flow in a tube with a fully developed laminar velocity profile, one can calculate k_L using the mass transfer relationship given by Leveque (1928):

$$\frac{k_L d_1}{D} = 1.615 \left(Re\, Sc \left(d_1 / L \right) \right)^{1/3}$$

where d_1 is the tube inside diameter, D is the diffusion coefficient in the liquid phase, Re is the flow Reynolds number, Sc is the Schmidt number, and L is the length of the tube. k_m can be determined using the following equation from the exact solution for steady-state diffusion through a cylindrical wall (Aunins and Henzler 1993):

$$k_m = \frac{2 D_m H \theta_m f}{H_m d_2 \ln\left(d_2 / d_1 \right)}$$

where D_m is the diffusion coefficient in the membrane, H and H_m are the Henry's law constants for the liquid and the membrane, respectively, θ_m is the tubing void fraction available for gas transport, d_2 is the outer tubing diameter and f is the correction factor that accounts for the tubing dimensional changes due to elastic deformation of the silicone rubber when it is pressurized. Several theoretical (Heath and Belfort 1987; Heifetz *et al.* 1989) as well as experimental (Piret and Cooney 1991) studies identified oxygen as the most important limiting nutrient in hollow fibre bioreactor cultures.

2.3.3. Oxygen Transport in HFBRs

The heterogeneous nature of the ECS, i.e. the presence of nutrient and metabolite gradients, poses a design challenge for optimal oxygen transport in HFBRs. Radial oxygen limitation has been correlated with internal necrotic regions in tumours (Thomlinson and Gray 1955; Tannock 1968) and spheroids of packed cells (Mueller-Klieser and Sutherland 1982). Since cells grow to packed-cell densities, the depletion of oxygen is expected and necrotic regions are likely to exist in the ECS. As a result of the oxygen gradients, the radial and axial dimensions of HFBRs are restricted to certain scales. The length of HFBRs and the spacing of the fibres are the two parameters that are considered in HFBR design to minimize the effects of oxygen gradients. Mathematical modeling and experimental analyses on the impact of nutrient mass transport limitations on the scale-up of HFBRs have been accomplished by a variety of investigators (Wei and Russ 1977; Webster and Shuler 1979; Webster and Shuler 1981; Davis and Watson 1985; Adema and Sinsky 1987; Chresand *et al.* 1988b; Piret and Cooney 1990a; Piret and Cooney 1991; Sardonini and DiBiasio 1992). Generally, these mathematical models

have been based upon mass balance relationships developed around a single fibre, and have been extrapolated to describe events occurring within the entire fibre bundle assuming uniform spacing. Chresand *et al.* (1988b) optimized fibre spacing in a diffusion limited HFBR. Sardonini and DiBiasio (1992) experimentally verified these diffusion-based limitations using a single fibre surrounded by animal cells.

In the Piret and Cooney (1991) model, the oxygen gradients at steady-state were derived from the equations of continuity for oxygen assuming constant density and diffusivity in the ICS, membrane, and ECS. In the ICS, the full equations of continuity in cylindrical coordinates are:

$$v_r \frac{\partial C_{O_2}}{\partial r} + v_z \frac{\partial C_{O_2}}{\partial z} = D_{O_2}\left(\frac{1}{r}\frac{\partial}{\partial r}\left(r\frac{\partial C_{O_2}}{\partial r}\right) + \frac{\partial^2 C_{O_2}}{\partial z^2}\right)$$

In this equation, C_{O_2} is the oxygen concentration, r the radial distance, z the axial distance, v_r the radial fluid velocity, v_z the axial velocity, and D_{O_2} the oxygen diffusivity. The axial diffusive term was neglected based on the ratio of convective and diffusive oxygen fluxes represented by the axial and radial Peclet numbers, Pe^z_L and Pe^r_L, respectively:

$$Pe^z_L = \frac{uL}{D_{O_2}}$$

$$Pe^r_L = \frac{v_r^L R_L}{D_{O_2}}$$

where u is the average ICS axial fluid velocity, L the length of the hollow fibre, v_r^L the average radial ICS velocity, and R_L the outer radius of the fibre lumen. After comparing the axial and radial Peclet numbers, the lumen radial convective flux was found to be two orders of magnitude lower than the radial diffusive transport, while the axial convective

term greatly exceeded its diffusive counterpart. Thus, the lumen continuity equation was reduced to

$$v_z \frac{\partial C_{O_2}}{\partial z} = D_{O_2}\left(\frac{1}{r}\frac{\partial}{\partial r}\left(r\frac{\partial C_{O_2}}{\partial r}\right)\right)$$

In the membrane, the radial Peclet number was calculated and the radial convective oxygen flux was found to be two orders of magnitude less than the diffusive fluxes. If the hollow fibre membrane is assumed to be isotropic, the axial flux term can be neglected. Therefore, the membrane continuity equations becomes

$$0 = D_{O_2}\left(\frac{1}{r}\frac{\partial}{\partial r}\left(r\frac{\partial C_{O_2}}{\partial r}\right)\right)$$

In the ECS, a term Q, for the volumetric oxygen uptake by the cells, was added to the general equation of continuity, yielding the following result:

$$v_r \frac{\partial C_{O_2}}{\partial r} + v_z \frac{\partial C_{O_2}}{\partial z} = D_{e,O_2}\left(\frac{1}{r}\frac{\partial}{\partial r}\left(r\frac{\partial C_{O_2}}{\partial r}\right) + \frac{\partial^2 C_{O_2}}{\partial z^2}\right) - Q$$

where D_{e,O_2} represents the effective diffusivity of oxygen through packed cells. It was again found, through Peclet number considerations, that the convective terms are negligibly small and the radial diffusive transport was orders of magnitude greater than the axial diffusive transport of oxygen because the radial concentration gradients greatly exceeded those in the axial direction. Therefore, the radial and axial convective fluxes as well as the axial diffusive flux can be neglected for a packed-cell ECS and the ECS continuity equation reduces to

$$0 = D_{e,O_2}\left(\frac{1}{r}\frac{\partial}{\partial r}\left(r\frac{\partial C_{O_2}}{\partial r}\right)\right) - Q$$

Piret and Cooney (1991) solved this oxygen transport problem analytically and established the upper limit of fibre spacing for the design of HFBRs based on oxygen delivery considerations.

2.3.4. Carbon Dioxide Transport

The accumulation of dissolved carbon dioxide in high-density perfusion cultures is an issue that has been discussed by several authors (Aunins and Henzler 1993; Ozturk *et al.* 1995; Gray *et al.* 1996; deZengotita *et al.* 1998; Zupke and Green 1998). Carbon dioxide is the principal end product of oxidative metabolism. Animal cells release carbon dioxide as a waste product and, under normal conditions, carbon dioxide freely diffuses from cells and evolves as a gas. In the case of high cell density cultures, the amount of carbon dioxide produced by the cells can accumulate as it exceeds the capacity of the bioreactor to remove carbon dioxide from the cell culture medium. In addition, any sodium bicarbonate added to the cell culture medium for the purpose of pH control will further increase the concentration of the dissolved carbon dioxide (Zanghi *et al.* 1999).

Dissolved carbon dioxide reacts with water to form carbonic acid, which readily dissociates to H^+ and HCO_3^-. At equilibrium, the following generalized reaction relates dissolved carbon dioxide, HCO_3^-, and H^+:

$$CO_2(aq) + H_2O \underset{k_{-1}}{\overset{k_1}{\rightleftharpoons}} H^+(aq) + HCO_3^-(aq)$$

where the *pK* is 6.32 in cell culture medium at 37 °C and atmospheric pressure (Arrua *et al.* 1990). From this relation, the pH of the cell culture medium can be estimated using the following relationship, by taking into account the equilibration of dissolved and atmospheric carbon dioxide and neglecting the dissociation of HCO_3^- to CO_3^{-2} (Sperandio and Paul 1997):

$$pH = log\left[HCO_3^-\right] - log\left[pCO_2\right] + 7.54$$

where pCO_2 is the partial pressure of gaseous CO_2 in bars. It has been reported that elevated pCO_2 can have an adverse effect on the growth and productivity of recombinant CHO (Gray *et al.* 1996; Zanghi *et al.* 1999) and hybridoma (deZengotita *et al.* 1998) cells.

A more recent study provides a more detailed description of the equilibrium reactions when gaseous CO_2 is dissolved in an aqueous solution (Soli and Byrne 2002):

$$CO_2(aq) + H_2O \underset{k_D}{\overset{k_H}{\rightleftharpoons}} H_2CO_3 \overset{K_{a1}}{\rightleftharpoons} H^+(aq) + HCO_3^-(aq) \overset{K_{a2}}{\rightleftharpoons} H^+(aq) + CO_3^{-2}(aq)$$

The first step in the sequence of reactions, i.e., the hydration/dehydration reaction, was assumed to be the rate limiting step. Subsequent reactions were assumed to achieve equilibrium instantaneously because the forward and backward kinetic rate constants for the two acid dissociation reactions are orders of magnitude larger than those for hydration/dehydration reaction (Edsall 1969; Soli and Byrne 2002). Also, because of the pK value of the second acid dissociation reaction is so high, i.e., 10.3 (Harned and Davis 1943), the amount of carbonate ion formed at the normal bioreactor pH range of 7.0-7.4 is expected to be minimal.

Carbon dioxide transport in hollow fibre modules has been previously described in a cell-free system (Kang *et al.* 1988) and for HFBRs containing microbes and algae (Markov *et al.* 1995; Ferreira *et al.* 1998; Carvalho and Malcata 2001). Markov *et al.* (1995) constructed a hollow fibre photobioreactor and experimentally measured the uptake of CO_2 by immobilized cyanobacteria. Ferreira *et al.* (1998) described the mass transfer of CO_2 in photosynthetic algal cultures in a microporous HFBR by measuring the mass transfer coefficients. In their experimental setup, gas flowed through the ICS while liquid medium was pumped through the ECS with its immobilized algae culture. The bulk concentrations of the six species (i.e., CO_2, H_2CO_3, HCO_3^-, CO_3^{-2}, H^+ and OH^-) involved in the equilibrium kinetics were estimated. Carvalho and Malcata (2001) also modelled bulk CO_2 mass transfer in a microporous HFBR containing a microalgae culture, where CO_2 enriched air was bubbled into the culture medium. However, there is currently no model describing the transport of carbon dioxide in ultrafiltration HFBRs culturing animal cells.

Chapter 3

FACTORS AFFECTING HYBRIDOMA CELL GROWTH AND VIABILITY DURING START-UP OF HFBRS

3.1. Motivation and Objectives

Efforts to enhance the performance of HFBRs have focused primarily on optimizing the growth conditions and the productivity of the bioreactor, once the culture has been well-established. One of the known but less widely discussed problems encountered in the production of recombinant proteins and antibodies in HFBRs is their slow start-up and, in some instances, complete failure to establish a viable culture. The slow start-up and occasional HFBR run failure would inevitably delay the development time and increase the production cost of recombinant proteins and antibodies. In a number of published results, visible delays of 4-9 days in the glucose uptake of hybridoma HFBRs were observed after inoculation (Evans and Miller 1990; Lowrey *et al.* 1994; Omasa *et al.* 1995; Czirbik *et al.* 1996; Gramer and Poeschl 1998). Similar data were published for HFBRs culturing lymphocytes and baby hamster kidney (BHK) cells where there was no observable glucose uptake for the first 5 (Lamers *et al.* 1999) to 8 (Ryll *et al.* 1990) days after inoculation. The primary aim of the research reported here was to identify factors causing the increased HFBR start-up delay and develop methods that reduce the influence of these limiting factors.

3.2. Experimental Procedure

3.2.1. Cell Line and Medium

The TFL-P9 hybridoma cell line, which secretes a rat anti-mouse IgG_1 monoclonal antibody (Stem Cell Technologies, Vancouver, BC), was grown in Dulbecco's Modified Eagle Medium (DMEM, Gibco BRL, Burlington, ON) supplemented with 2% Fetal Bovine Serum (FBS, Sigma, St. Louis, MO). After thawing, the cells were cultured in 75 cm^2 and 150 cm^2 t-flasks and maintained at 37 °C in a 5% CO_2 atmosphere inside a humidified incubator (Forma, Marietta, OH).

The total and viable cell concentrations were counted via a haemocytometer. The viable cell population was distinguished from nonviable cells by the trypan blue dye exclusion method (Freshney 1994). Cells were kept in the exponential growth phase by splitting the cultures before they reached the stationary phase, i.e., at ~$2x10^6$ cells mL^{-1} for the TFL-P9 hybridoma cell line.

3.2.2. Hollow Fibre Bioreactor Setup

Two types of hollow fibre bioreactors were used. One was the Cell-Pharm System 100 hollow fibre bioreactor (Unisyn Technologies, Hopkinton, MA). This hollow fibre cartridge had a nominal molecular weight cut-off of 30 kDa, with the membrane material composed of cellulose acetate. In each HFBR, approximately $1x10^8$ cells with 90% viability were suspended in 10 mL of medium and inoculated, via the upstream ECS port with the downstream ECS port open and the two ICS ports closed. The ICS recirculation pump was started 20 min after the cells were added (Labecki *et al.* 2004).

The other HFBR system was self-assembled using a Gambro ALWALL Plus 16 ultrafiltration cartridge (Hechingen, Germany). Approximately $2x10^8$ cells with 90% viability suspended in 50 mL of medium were inoculated, via the upstream ECS port, 20 min before starting the ICS recirculation pump. The ICS and ECS medium were supplemented with 2 mM of L-glutamine and 2-10% of FBS. The hollow fibre cartridge was inclined at a 45 degree angle, with the ICS inlet situated below the ICS outlet. The hollow fibre bioreactor system consisted of the Gambro cartridge, a self-assembled oxygenator/ventilator, a 2 L ICS reservoir, Masterflex Pharmed tubing and a peristaltic pump (Cole-Parmer, Vernon Mills, IL). Sampling ports were connected to the ICS circuit between (1) the cartridge and the ICS reservoir, (2) the ICS reservoir and the ventilator, and (3) the ventilator and the HFBR cartridge (see Figure 2.1). The ventilator consisted of a 7.6 m long segment of thin-wall silicone tubing (Cole-Parmer, IL) coiled around a 20x10x10 cm support. The silicone tubing and the support were enclosed in a 30x18x18 cm sealed plastic vessel, in which the atmosphere was controlled by manually adjusting the flow rates of oxygen, nitrogen and carbon dioxide.

3.2.3. Nutrient and Metabolite Measurements

Glucose, lactate and urea nitrogen medium concentrations were measured using a Stat Profile Plus 10 blood-gas analyzer (Nova Biomedical, Waltham, MA). The urea nitrogen concentrations measured by this instrument were converted to ammonium concentrations by means of a calibration curve obtained using 0-6 mM standard solutions of ammonium chloride (Sigma, MO). Glutamine concentrations were determined by a colorimetric glutaminase-based assay (Lund 1985) in flat bottom microtiter plates (Corning, NY).

3.2.4. Serum Concentration Experiment

Hybridoma cells were inoculated at a concentration of $4.8x10^4$ cells mL^{-1} in 75 cm^2 t-flasks containing 20 mL of 0, 1, 2, 5, 8, or 10% (v/v) FBS, representing the range of values typically used in cell culture (Freshney 1994). A second experiment was performed with 0, 0.5, 1, 2, 3, or 4% (v/v) FBS.

3.2.5. Hollow Fibre Cartridge Rinse Experiment

A hollow fibre bioreactor system was assembled using a Gambro ALWALL Plus 16 cartridge. In a typical rinsing procedure, the ICS was first flushed with 2 L DMEM over 24 h in a 37°C warm room at an ICS flow rate of approximately 100 mL min^{-1}. This medium was then replaced by another litre of DMEM, which was added to the ICS reservoir and allowed to recirculate at 300 mL min^{-1} for an additional 24 h prior to inoculation. The rinse media were collected and stored at 4°C. In the modified rinsing procedure, a second cartridge was flushed by pumping 2 L DMEM from the ICS through the membrane to the ECS (in approximately 3 h at a flow rate of 10 mL min^{-1}) prior to the ICS recirculation of another litre of DMEM for 24 h at 300 mL min^{-1}. These rinse media were also collected and stored at 4°C. Batch cell culture experiments using the collected media from both rinsing procedures (each supplemented with 2% FBS) were performed in 75 cm^2 t-flasks inoculated at ~$1x10^5$ cells mL^{-1}. DMEM plus 2% FBS that had only been incubated for 48 h at 37°C, without HFBR contact, was inoculated as the control.

3.2.6. Cell Pellet Experiment

Hybridoma cells in the mid-exponential growth phase were settled by gravity (for 24 h) or centrifuged in 50 mL tubes (Corning, NY) at 1,000 g for 10 min. The supernatants were discarded and DMEM supplemented with 2% FBS and 2 mM L-glutamine was slowly added to each tube so as not to disturb the pellet. The cell pellets were then incubated at 37°C for up to 50 h. At the end of the incubation period, the medium was either decanted carefully without disturbing the pellets, or the cells were resuspended with vortex mixing. The medium was centrifuged and decanted once more to remove any residual cells. Once all clarified media from various durations of exposure to cell pellets had been collected, each was seeded with a fresh inoculum at ~$2x10^5$ cells mL^{-1} and batch cultures were performed in 75 cm^2 t-flasks.

The settled cell density was estimated by mass difference measurements. Pre-weighed 50 mL centrifuge tubes were filled with a known volume containing a known concentration of cells. The cells were allowed to settle by gravity for 17 h in a 37°C environment. The supernatant was carefully removed without disturbing the pellet. The centrifuge tubes and pellets were re-weighed. Assuming that the mass density of the cells is approximately 1.13 g mL^{-1} (Wang and Hwang 1992), the cell pellet density, which has units of cells mL^{-1}, was estimated by dividing the total number of counted cells by the mass difference and by multiplying by the mass density of the cells.

3.2.7. Ammonium or Lactate Dose Response

Cells from an exponentially growing culture were centrifuged, used to inoculate 75 cm^2 t-flasks at $2x10^5$ cells mL^{-1} and cultured for 48 h in DMEM supplemented with 2% FBS and 0-10 mM ammonium chloride or 0-40 mM L-lactic acid (Sigma, St. Louis, MO).

The supplemented media pH values were adjusted to 7.4 prior to inoculation. Cell numbers and viability were determined using the trypan blue dye exclusion method and a hemocytometer.

3.2.8. Statistical Analysis

The significance of differences between values was determined by the Student's *t* test. The error bars shown on the graphs represent standard deviations of the data.

3.3. Results and Discussion

3.3.1. Typical Start-Up Problems

Identifying the factors associated with a prolonged start-up in HFBRs may yield insight about how the overall productivity of HFBR and other immobilized cell cultures can be improved. Due to the structure of these bioreactors with the cells trapped in the ECS, cell concentration and viability usually cannot be measured directly. Viable cell numbers are instead inferred from nutrient uptake and metabolite production. In this study, the progress of HFBR cultures was assessed using glucose uptake rates. In addition, a parallel spinner culture was used as a basis of comparison, seeded from the same inoculum culture and with the same cell concentration as the HFBR, where the latter is based on the total volume of the ICS and ECS.

An example of a typical HFBR start-up can be seen in Figure 3.1, which compares the time-dependent glucose concentrations measured in a spinner with those found in the ICS of a Gambro HFBR culturing the same cells. The change in glucose concentration

provides an indication of the rate of cell growth in each case. In the parallel-operating HFBR, the glucose concentration decreased more slowly compared to the spinner batch culture. After 3 days, the batch rate slowed as the cells entered the stationary phase. At this time, fresh medium was added to the HFBR, leading to an increase in the glucose concentration. Another example of HFBR start-up delay can be seen when comparing the cumulative glucose consumed on a volumetric basis between three Cell-Pharm CP100 HFBRs and their parallel-operating spinner batch cultures (Figure 3.2). It took about 3 days for cells in the batch spinner cultures to consume 15 mM of glucose, whereas it took

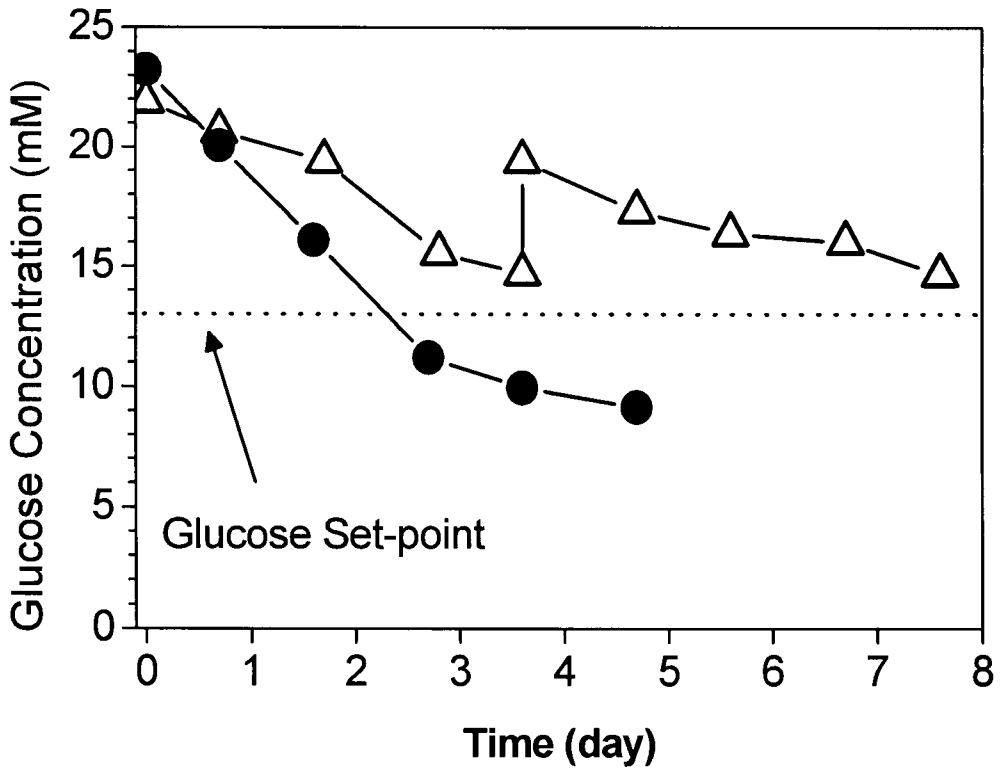

Figure 3.1 Glucose concentrations of a batch spinner culture (-●-) and a hollow fibre bioreactor (-Δ-) using the Gambro ALWALL Plus 16 cartridge, started in parallel. Inoculum concentration for both devices was 2.0×10^5 cells mL^{-1} on a total volume basis. Medium was DMEM + 2%FBS + 2mM L-glutamine. Fresh medium was added to the HFBR on day 4, resulting in an increase in the glucose concentration.

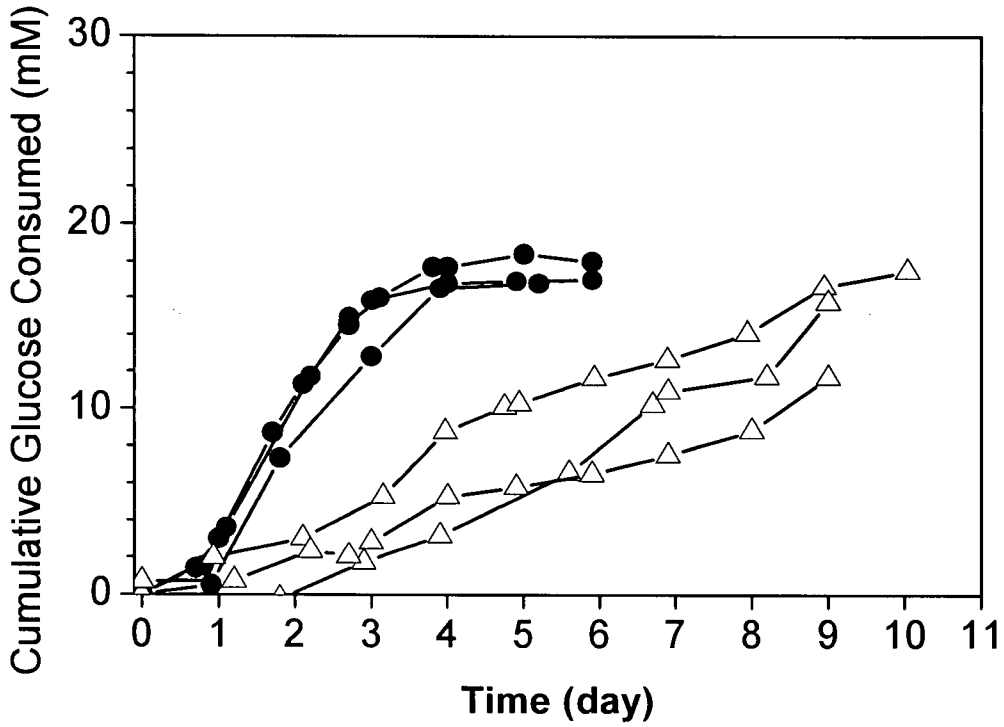

Figure 3.2 Cumulative glucose consumed on a volumetric basis for three parallel batch cultures (-●-) and three corresponding hollow fibre bioreactors (-Δ-) using the Cell-Pharm CP100 bioreactor system. Inoculum for all devices was approximately $1.5x10^5$ cells mL^{-1} on a total volume basis. Medium was DMEM + 2%FBS + 2mM L-glutamine.

approximately 8 days for the HFBRs to consume the same amount of this nutrient.

3.3.2. Effect of Fetal Bovine Serum

Mammalian cells have traditionally been cultured in media containing fetal bovine serum (FBS) that provides necessary growth factors and nutrients. It has been reported that serum can also increase the apparent specific growth rate by acting as a shear-protecting agent that decreases the rate of cell death (Ozturk and Palsson 1991). The effect of serum concentration from 0.5% to 10% (v/v) on the TFL-P9 hybridoma cell growth in batch cultures is shown in Figure 3.3. Average growth rates were calculated assuming exponential growth for the duration of the batch culture. The growth rate decreased

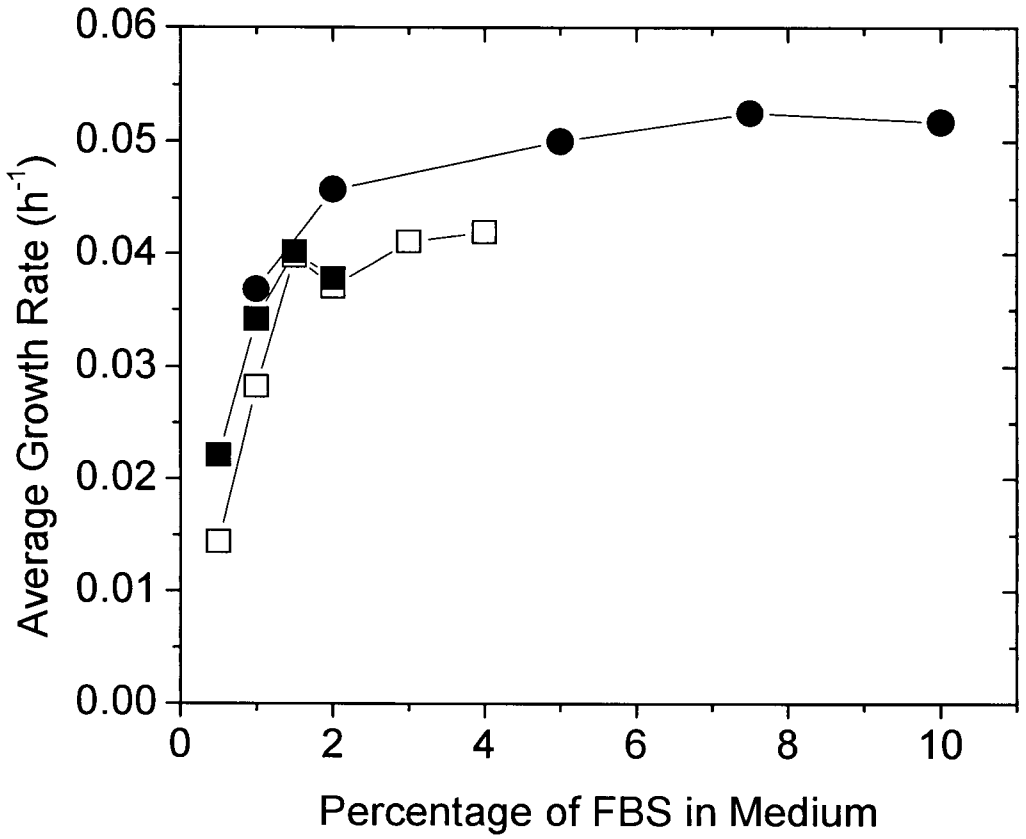

Figure 3.3 Effect of FBS concentration (v/v) on the growth rate of TFL-P9 hybridoma cells using DMEM as the basal medium. Data are taken from three separate sets of batch cultures, where starting cell concentrations are $3.9x10^4$ (-●-), $7.4x10^4$ (-■-) and $7.6x10^4$ (-□-) cells mL^{-1}. The duration of each culture is approximately 72 h.

sharply when the serum concentration dropped below 2% (v/v). When the serum concentration was increased from 2% to 10% FBS (v/v), the growth rate increased by approximately 20%.

Since the HFBR operates similarly to a batch culture during the start-up period, where there is no addition or removal of medium to or from the system, it is possible that increasing the serum concentration in the ECS can lead to faster cell growth. However,

the HFBRs using 10% FBS (v/v) in the ECS did not exhibit a greater cumulative glucose uptake than those with 2% FBS (Figure 3.4). The linear relationship between the cumulative glucose uptake and time (Figure 3.4) suggests that the cells in the HFBRs were not undergoing exponential cell growth. The presence of other factors that contribute to the prolonged HFBR start-up could have overshadowed any beneficial effect of a higher serum concentration on cell growth.

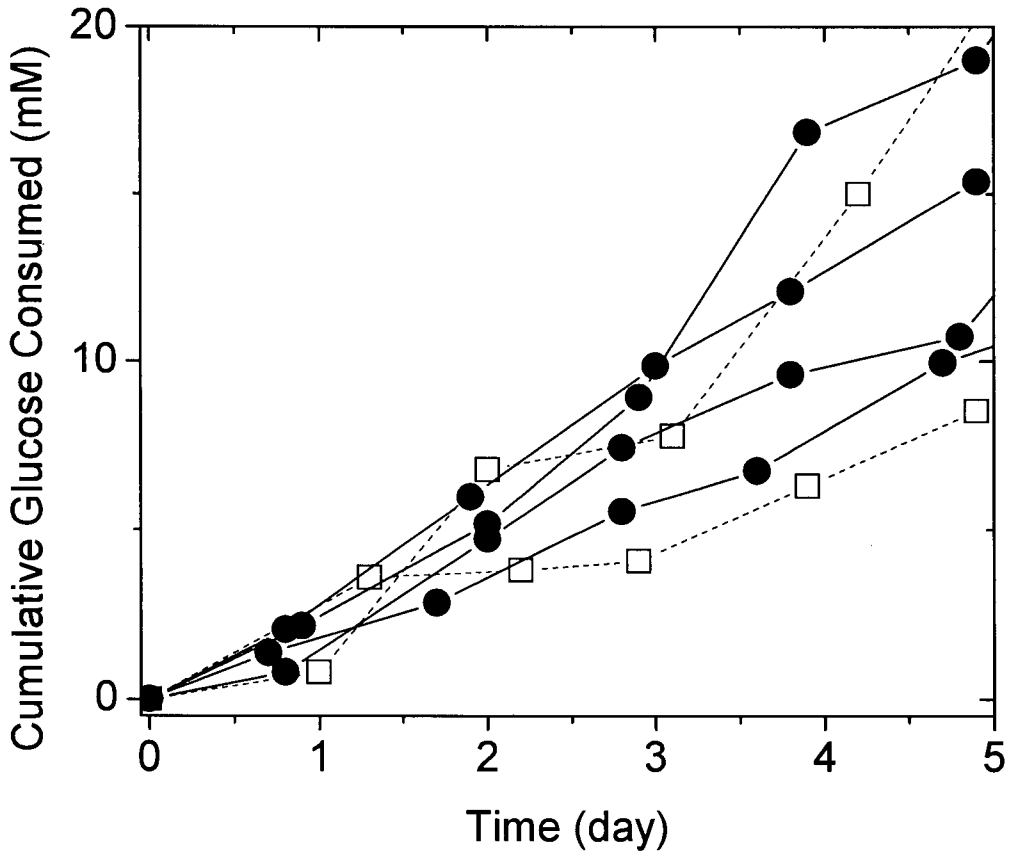

Figure 3.4 Cumulative glucose consumed on a volumetric basis for two separate HFBR runs using 10% FBS (-□-) and four runs using 2% FBS (-●-) in a Gambro ALWALL Plus 16 cartridge self-assembled bioreactor systems. Inoculum for all devices was approximately 1.5×10^5 cells/mL on a total volume basis. Basal medium was DMEM supplemented with 2mM L-glutamine.

The lack of a beneficial effect of a higher serum concentration could be explained by the downstream polarization of growth factors due to a secondary Starling flow in the ECS driven by the primary recirculation flow in the ECS (Piret and Cooney 1990a). This polarization of growth factors from the bulk of the ECS to the downstream region could also contribute to the start-up delay in HFBRs, irrespective of the initial serum concentration. For this reason, the HFBRs were operated at a 45-degree incline to reduce the overall effect of downstream polarization as suggested by Piret and Cooney (1990a). However, the transient redistribution of proteins in the ECS would take hours, which was shown by a recent three-dimensional protein transport model (Labecki *et al.* 2004). This could deprive the bulk of the ECS of growth factors for a significant period. Therefore, the redistribution of growth factors during the initial stage of culture could also exacerbate the delay in HFBR start-up.

3.3.3. Inoculum Size

For a batch culture, a minimum cell concentration (e.g. 10^4 cells mL^{-1}) is usually required for a successful start-up (Freshney 1994). Similarly, higher hybridoma inoculum cell concentrations can reduce the time required to achieve the maximum level of antibody production from HFBRs (Evans and Miller 1990). HFBRs inoculated with $3.5x10^5$ cells/mL on a total volume basis appeared to have slightly faster start-ups compared to those inoculated with $1.5x10^5$ cells mL^{-1} (Figure 3.5). Therefore, a larger inoculum can help to reduce the start-up delay. However, there are problems associated with cultivating a larger inoculum. To obtain a larger inoculum, the operator may feel compelled to grow the inoculum culture to a later growth phase or even the stationary phase. Martial *et al.* (1991) found that the cells from later growth phases also yielded

longer delays. For the TFL-P9 hybridoma cells tested here, the start-up delay increased up to as much as 50 h if the inoculum was taken from the stationary rather than from the early exponential phase (Henry 2000). Therefore, when increasing the size of the inoculum, this effect of inoculum phase on prolonging the start-up delay should be taken into consideration.

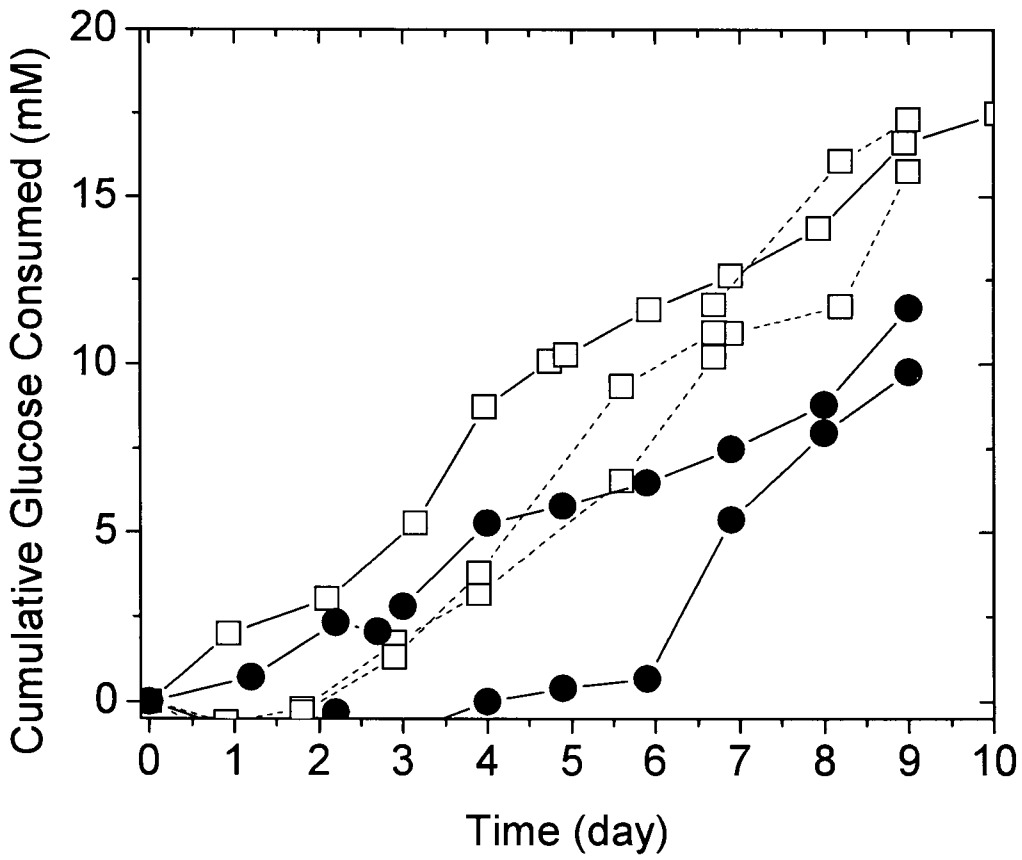

Figure 3.5 Cumulative glucose consumed on a volumetric basis for hollow fibre bioreactors runs with inoculum sizes of $1.5x10^5$ cells/mL (-●-) and $3.5x10^5$ cells/mL (-□-) on a total volume basis using the Cell-Pharm CP100 bioreactor system. Medium was DMEM + 2%FBS + 2mM L-glutamine.

3.3.4. HFBR Rinsing

An important factor that could lead to start-up delay is insufficient rinsing of the HFBR cartridge prior to inoculation. As a by-product of the manufacturing process, HFBR fibres can contain residual chemicals, including plasticizers, additives and solvents, that could adversely affect the growth and viability of cultured cells (Reif *et al.* 1996). Before inoculating a mammalian cell culture in an HFBR, extensive washing is normally required. In the normal rinsing procedure, two litres of medium was recirculated in the ICS for 24 h and drained prior to inoculation. A 28% decrease in growth rate relative to control was observed for cells cultured in the medium taken from the initial two-litre, 24 h ICS rinse (Figure 3.6). In normal HFBR operations, cells are inoculated after the two-litre medium rinse has been completed. A 10% decrease in cell growth was observed when cells were cultured in another litre of rinsing DMEM that had been recirculated in the ICS for an additional 24 h. It has been shown that the rinse solution from a hemodialyser composed of hemophan, the same membrane material used in the Gambro HFBR cartridge, led to a decrease in the mitochondrial ATP synthesis of a human colon adenocarcinoma cell line (Tabouy *et al.* 1997). A deleterious effect on the metabolic activity for a promyelocytic cell line has also been reported when the cells were incubated in the presence of a hemophan membrane (Kubala *et al.* 2002). Both reports support the hypothesis that insufficient rinsing of the membrane material in the cartridge can lead to an increase in the start-up delay of a HFBR culture.

Dead-end rinsing, i.e., where the rinse fluid was forced through the membrane from the ICS to the ECS, was performed to more effectively rinse the HFBR cartridge. The decrease in growth rate from the two-litre dead-end rinse was statistically

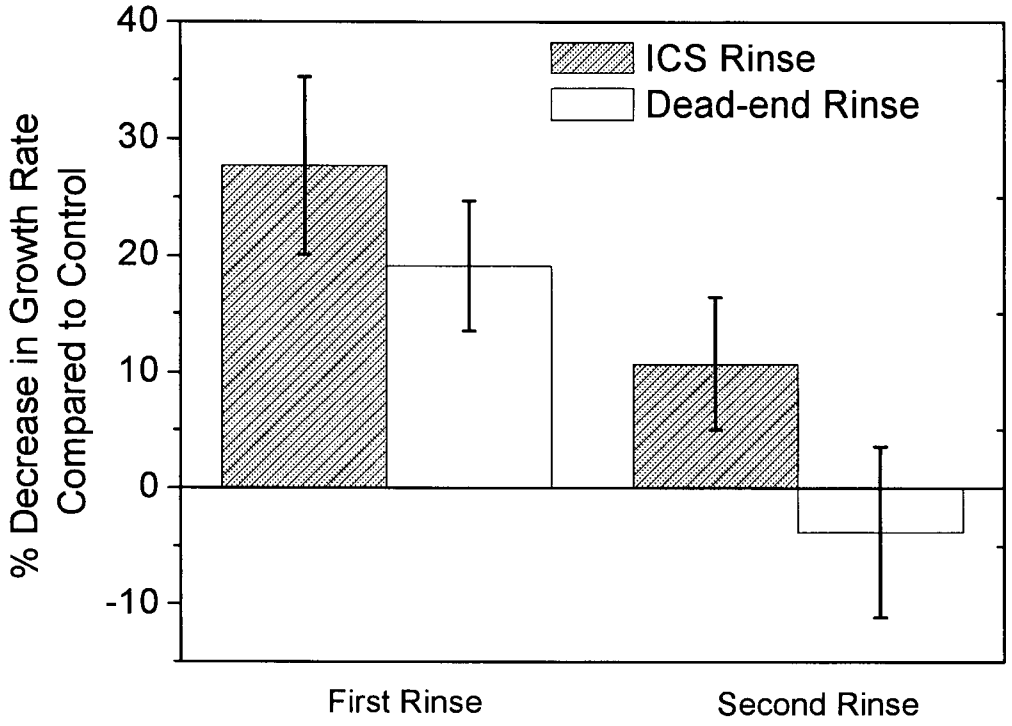

Figure 3.6 Effect of cartridge rinsing procedure on cell growth. For a typical rinsing procedure (shaded bars), the intracapillary space (ICS) was flushed with two litres of DMEM followed by another litre of DMEM. In the dead-end rinsing procedure (unshaded bars), two litres of DMEM was flushed from the ICS through the membrane to the extracapillary space (ECS) followed by ICS rinsing with another litre of DMEM. Batch cultures with a starting inoculum of $1x10^5$ cells mL^{-1} were performed using media collected from each rinsing procedure. Error bars represent the standard deviations of triplicate data.

indistinguishable from the 2-litre ICS rinse solution (Figure 3.6). No decrease in growth rate compared to control was found for the one-litre ICS rinse that followed the two-litre dead-end rinse (Figure 3.6). When such a dead-end washing procedure is used, the transmembrane pressure drop is significantly greater, forcing the rinse solution to pass through a much larger fraction of the membrane pores. Such improved rinsing procedures may more generally reduce start-up delay kinetics, especially for sensitive primary cultures in biomedical applications.

3.3.5. Settling of Cells in HFBRs

In a typical inoculation procedure, the inoculum is pumped at a slow rate (e.g., 5 mL min^{-1}) into one ECS port while the displaced ECS medium is collected from the other. Gravity can cause a portion of the inoculum to settle to the bottom of the bioreactor, including into the fibre-free manifold regions where deprivation of nutrients such as oxygen may occur (Piret and Cooney 1991). Within minutes after inoculation, it was observed that a visible mass of cells settled in the manifold regions of the ECS. This settled mass of cells became even more apparent in the downstream ECS manifold 16 h after inoculation. Such additional accumulation was only visible in the upstream manifold after approximately 62 h (Figure 3.7). The centrifuged or settled pellet cell density was calculated to be $2x10^8$ cells mL^{-1} based on the mass of a gravity-settled pellet containing a known number of cells. The total number of cells settled in the manifold regions was then estimated by measuring the external dimensions of the visible cell mass. It was found that an amount equivalent to approximately $9x10^6$ cells, or 5% of the initial inoculum, settled into the manifold regions within 16 h after inoculation, and approximately $7x10^7$ cells, or 44% of the initial inoculum, settled after 62 h. This accumulation of cells in the manifold regions suggests that a significant fraction of the growing cell mass is progressively removed from the fibre bundle into this nutrient-deprived location where they will become nonviable, thereby contributing to the prolonged start-up delay compared to a parallel batch spinner culture.

The oxygen penetration depth in a HFBR was estimated to be approximately 300 μm by Piret *et al.* (1991), whereas the settled mass in the manifolds is located a few millimetres away from the nearest hollow fibres. It is likely that the bulk of the settled cells was

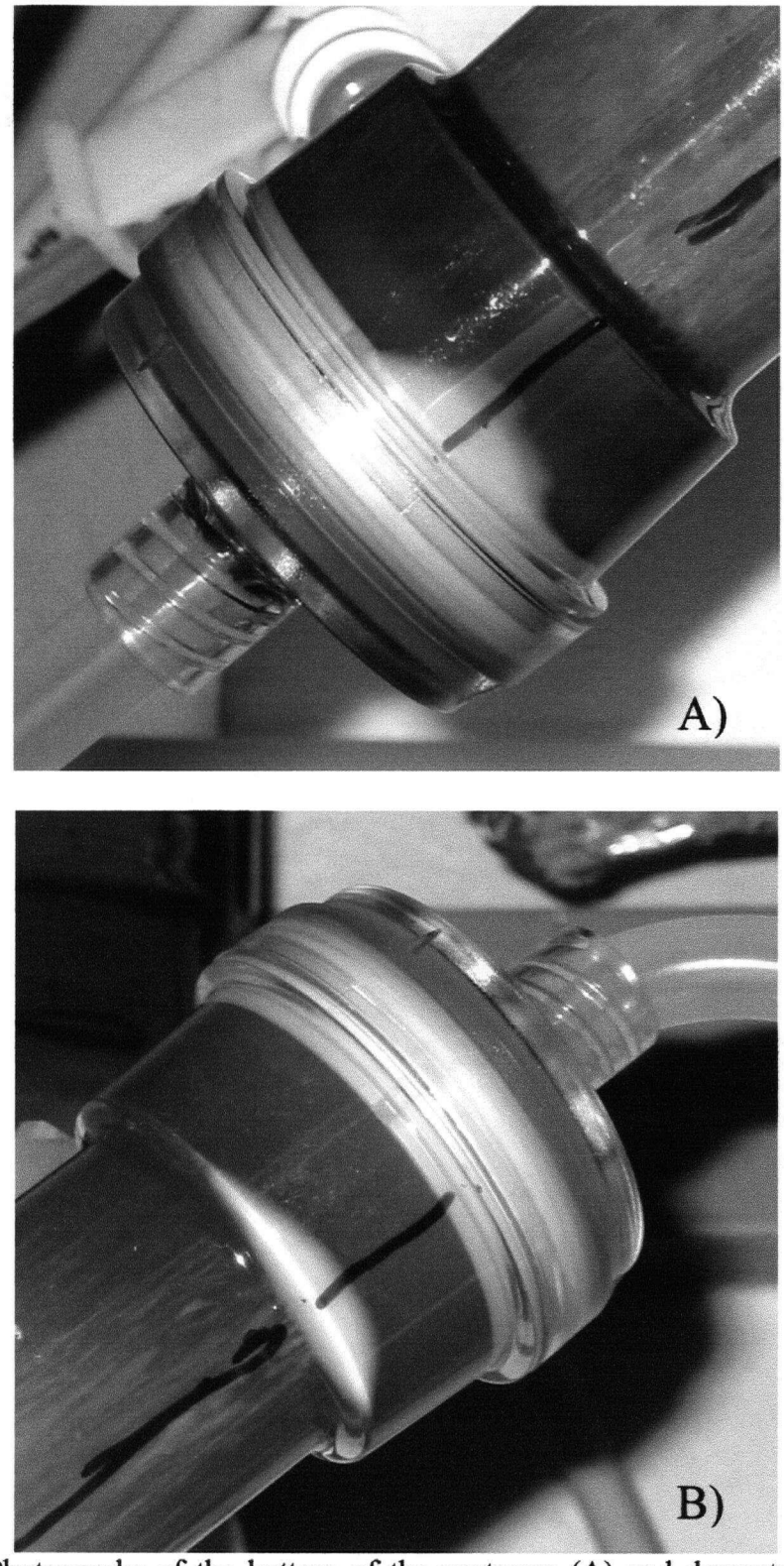

Figure 3.7 Photographs of the bottom of the upstream (A) and downstream (B) ECS manifolds 62 h after inoculation. Settled cells appear as white masses within the manifold regions and the marker line indicates the centre of the bottom side of the cartridge.

exposed to an environment where oxygen is limiting. Experiments were performed to mimic the oxygen limiting conditions in the manifolds. The viability of the cells in a spun-down but subsequently undisturbed pellet decreased to 30% after 10 h at 37°C (Figure 3.8). The cell viability further decreased to 6% after 50 h of incubation. These results suggest that a large fraction of the cells accumulated in the ECS manifold region are likely to be nonviable after 50 h.

The dying cells in the manifold may also have released factors that inhibit the growth of the cells remaining in the HFBR bundle region. The release of soluble factors causing

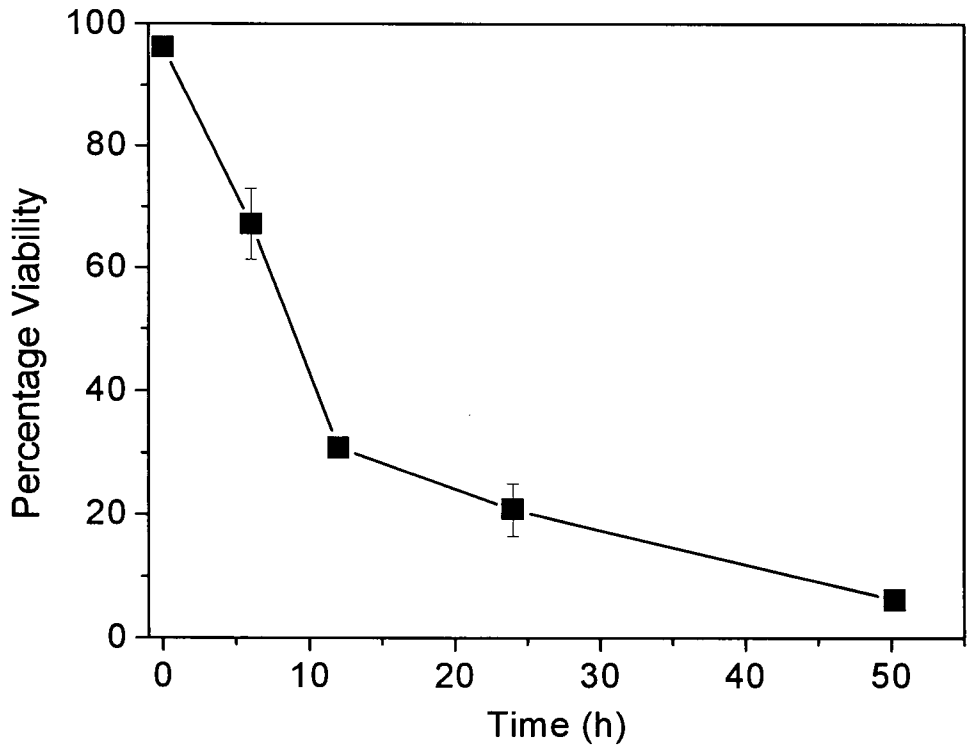

Figure 3.8 Cell viability in a cell pellet versus time. Cell pellets were created from 50 mL samples of a culture at $6x10^5$ cells mL^{-1} with 94% viability, centrifuged at 1,000 g for 10 min. Cell-free supernatant was replaced with fresh DMEM+5%FBS. The cell pellets were incubated at 37°C in a 5% CO_2 atmosphere. The viabilities were measured after gently resuspending the pellet. Error bars represent standard deviations of triplicate data.

cell death in a primary cell culture was described by Lynch *et al.* (1986). Siegel and Liu (1997) reported that apoptosis can be induced by medium exposed to dying cells. Furthermore, tumour cells experiencing hypoxia were shown to release cell death factors that could induce cell necrosis (Sowter *et al.* 2001). To test this hypothesis for hybridomas, TFL-P9 cells were exposed to the supernatants of a spun-down cell pellet, either with or without cell resuspension and recentrifugation. Due to presence of an ICS axial pressure gradient, ECS Starling flow can cause convective transport of cell lysis products to viable cell regions. The decanted samples approximately simulated conditions where only lysis products that diffuse from the pellet influence inoculum growth while resuspended samples better represent conditions where the ECS is well mixed, as would occur when cell death is more evenly distributed. A larger decrease was found for the resuspended cell samples, as would be expected. In either case, cell growth decreased with increased time of exposure of the medium to the cell pellet (Figure 3.9). After 24 h of media exposure to the pellet, subsequent cell growth decreased 13% for the decanted sample and 27% for the resuspended sample and, after 50 h, it decreased by 23% and 37%, respectively. These results suggest that the death of settled cells in the manifold regions may release factors that inhibit cell growth and, hence, may prolong the HFBR start-up delay.

In section 3.3.3, it was shown that increasing inoculum size can reduce the HFBR start-up delay. However, an increase in inoculum size could also lead to an increase in the number of cells settling into the manifolds. As shown above, the beneficial effect of having more inoculum could be counteracted to some extent by the increased release of growth inhibiting factors from cells dying in the manifolds.

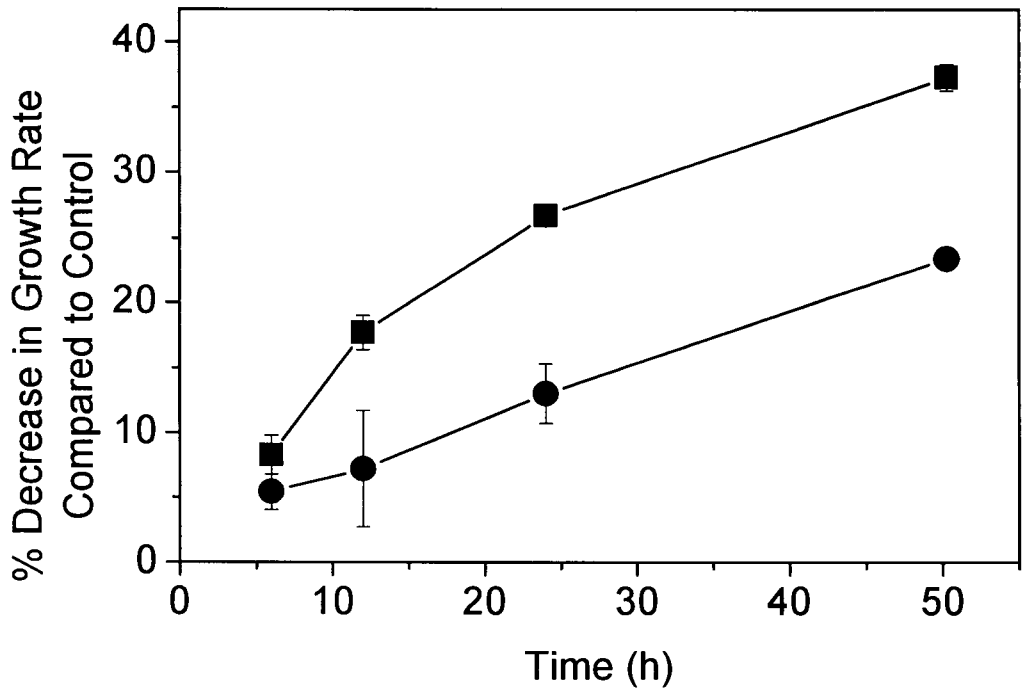

Figure 3.9 Effect of exposure to cell pellet on growth rate of fresh cells for the decanted incubated medium (-●-) and the resuspended incubated medium (-■-). Error bars represent standard deviations of triplicate data.

3.3.6. Nutrients and Metabolites

Another factor that may contribute to HFBR start-up delay is the accumulation of inhibitory metabolites as healthy cells multiply in the HFBR. An important metabolite is the ammonium ion, produced by cells mainly via the de-amination of L-glutamine. L-glutamine is the primary source of nitrogen as well as an important carbon and energy source for cells (Zeilke *et al.* 1984). Varying concentrations of ammonium chloride were added to the medium to observe the effect on hybridoma cells cultured in t-flasks. The growth of the hybridoma cells decreased as the initial ammonium concentration increased

above 3 mM, with a 50% growth inhibition at 7 mM (Figure 3.10). These results correspond with published data where ammonium, in the range of 2-10 mM, has been observed to inhibit cell growth by 50% (Glacken *et al.* 1986; Ozturk *et al.* 1992).

Thermal degradation of L-glutamine also contributes to the build-up of ammonium in the ECS (Zeilke *et al.* 1984; Ozturk and Palsson 1990). L-glutamine thermally degrades to ammonium such that, even without cellular metabolism, the concentration of glutamine decreased exponentially with time under reactor conditions, with a half life of approximately 6 days (Figure 3.11), consistent with the rate reported by Ozturk and Palsson (1990). The total amount of medium L-Glutamine was 4 mM, and, the

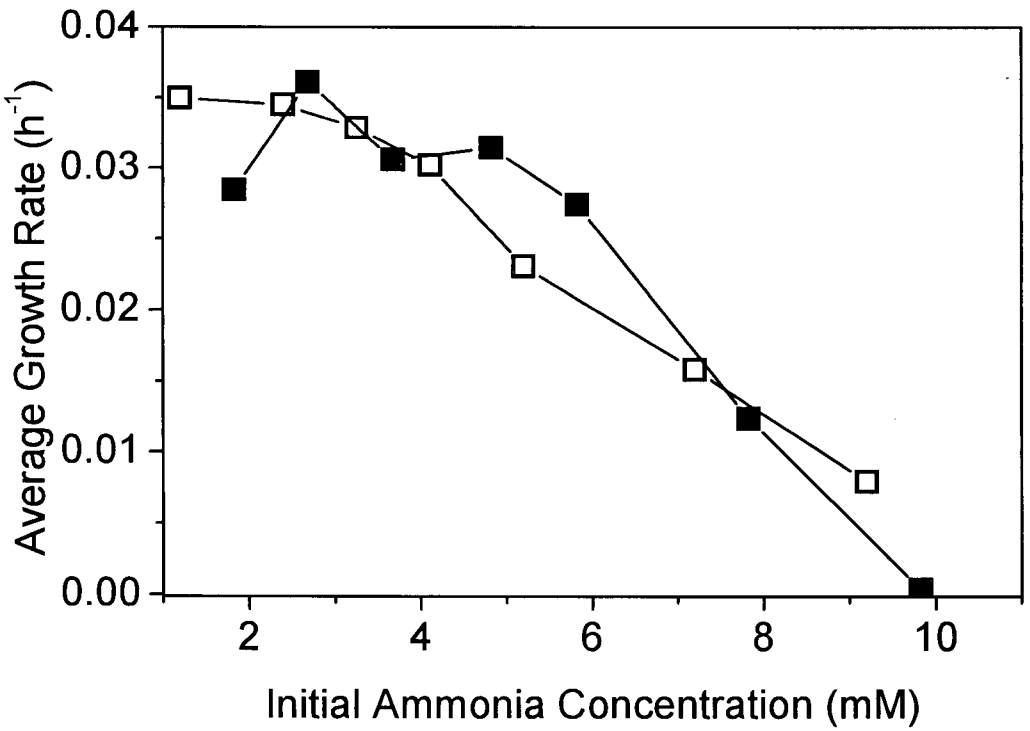

Figure 3.10 Growth rate of hybridoma cells in response to initial ammonia concentration. Results are from two separate duplicate experiments.

maximum ammonium concentration due to thermal degradation and metabolism of L-glutamine, therefore, would also be approximately 4 mM. In situations where an HFBR experiences a prolonged start-up, this level would not be expected to reduce growth rate significantly (Figure 3.10). However, the build-up of ammonium ions, in combination with other factors, may exacerbate the decrease in cell growth.

One other metabolite that accumulates as healthy cells multiply in an HFBR is lactate. Lactic acid is the primary metabolic product of glucose (Zeilke *et al.* 1984). It readily dissociates to form hydrogen ions and lactate ions. Varying concentrations of L-lactic acid were added to the medium to observe their effect on TFL-P9 cells cultured in t-flasks. The growth of the hybridoma cells was not significantly reduced in the range of

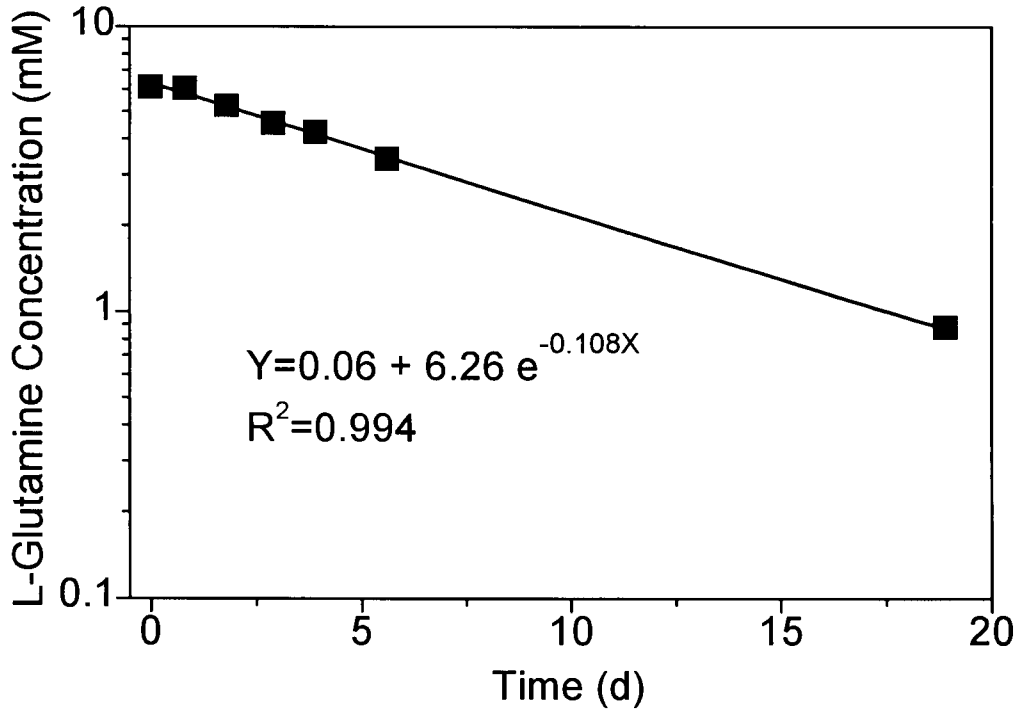

Figure 3.11 L-glutamine concentration versus time after being placed in a 37°C humidified incubator with a 5% CO_2 atmosphere.

0-30 mM lactate (Figure 3.12), the typical concentrations in HFBR culture. Therefore, lactate is not likely to be an important factor in contributing to start-up delays in HFBRs.

HFBRs are commonly monitored and controlled based on glucose concentration changes in the ICS medium. In situations, as discussed above, where there may be a loss of inoculum via settling in the manifold and other factors affecting cell growth, the bioreactor glucose consumption rate will decline. If these negative influences are compounded such as by the effect of the inoculum phase, where the start-up delay can increase up to 50 h, the time prior to fresh medium addition to the HFBR can be

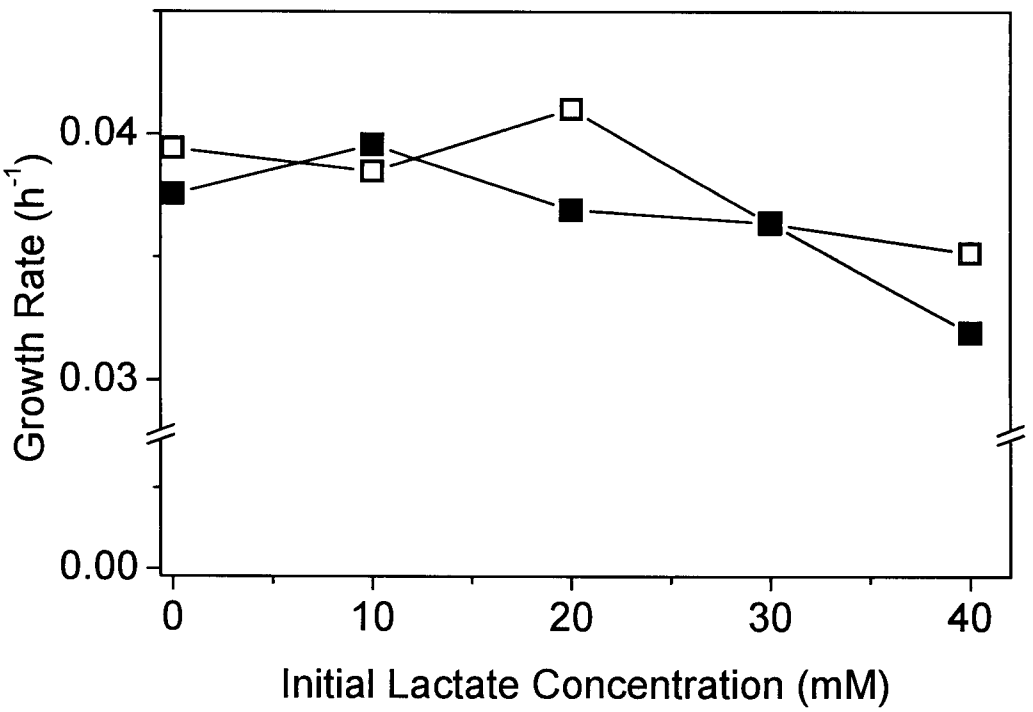

Figure 3.12 Growth rate of hybridoma cells in response to initial lactate concentration. Results are from two separate experiments.

significantly lengthened. As a result, more of the L-glutamine in the medium will have a chance to degrade to ammonium ions. Ultimately, the L-glutamine concentration could fall below the minimum level needed to sustain cell growth. For instance, in one HFBR run with a long start-up delay, the L-glutamine level dropped to 0.2 mM within 7 days (Figure 3.13), while the glucose level remained above the set-point concentration of 15 mM such that the fresh medium feed was not initiated. Therefore, in situations where an HFBR experiences a prolonged start-up, the decrease in L-glutamine concentration due to combined metabolic activity and thermal degradation can also further decrease cell growth.

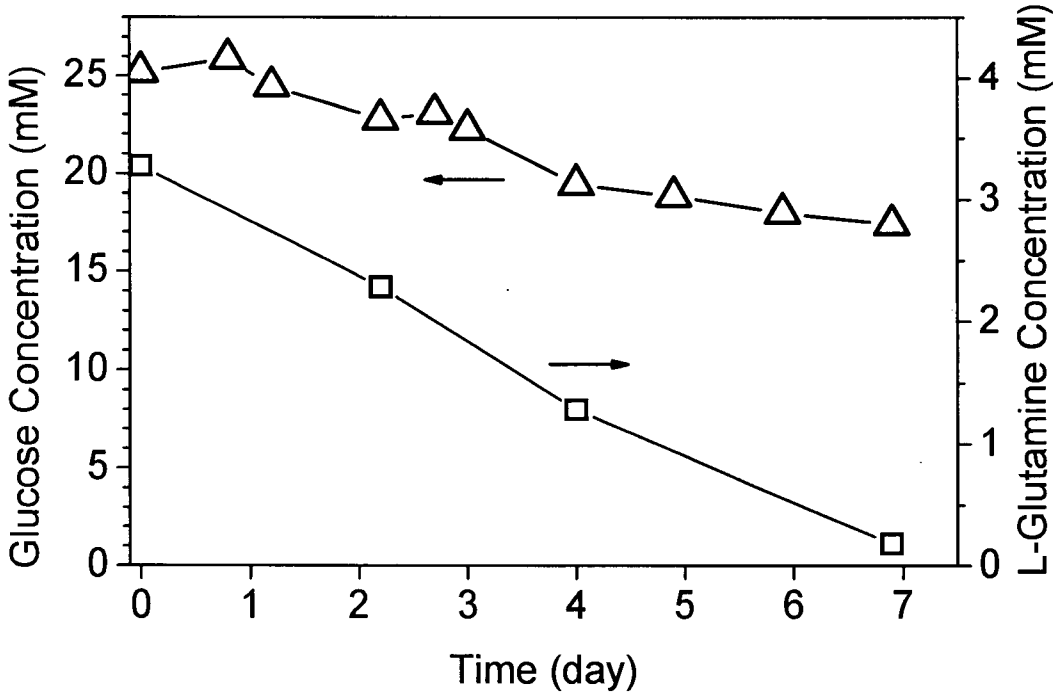

Figure 3.13 L-glutamine and glucose concentrations in the ICS of a hollow fibre bioreactor that experienced a slow start-up. Inoculum concentration was 1.5×10^5 cells mL^{-1} on a total volume basis. Medium was DMEM + 2%FBS + 2mM L-glutamine

3.3.7. Minimizing Factors Causing Start-up Delay

A HFBR run with TFL-P9 hybridoma cells was carried out using procedural changes intended to alleviate some of the factors that are suspected of causing start-up delays based on the results in this chapter. The HFBR cartridge underwent a dead-end rinse prior to inoculation instead of the typical ICS rinse. A larger inoculum concentration, in this case ~$4x10^5$ cells mL^{-1}, compared to $2x10^5$ cells mL^{-1} (Figure 3.1), was seeded in the HFBR. During the first 24 h, the cartridge was rotated frequently to reduce the settling of cells in the ECS manifolds. The medium FBS concentration was increased from 2% to 5% based on the small effect of greater than 2%FBS on TFL-P9 growth rates (Figure 3.3). As was done for all runs, the cartridge was inclined at a 45 degree angle in order to minimize the downstream polarization of growth factors.

The glucose concentrations of the HFBR and a parallel batch spinner can been seen in Figure 3.14. In the HFBR, the glucose concentrations decreased at only a slightly slower rate than in the spinner batch culture. Over the first few days of operation, the cumulative glucose consumed on a volumetric basis for the HFBR was also slightly lower than in the comparable spinner batch culture (Figure 3.14). These results suggest that careful control of conditions during the initial stages of a HFBR run can significantly reduce start-up delay.

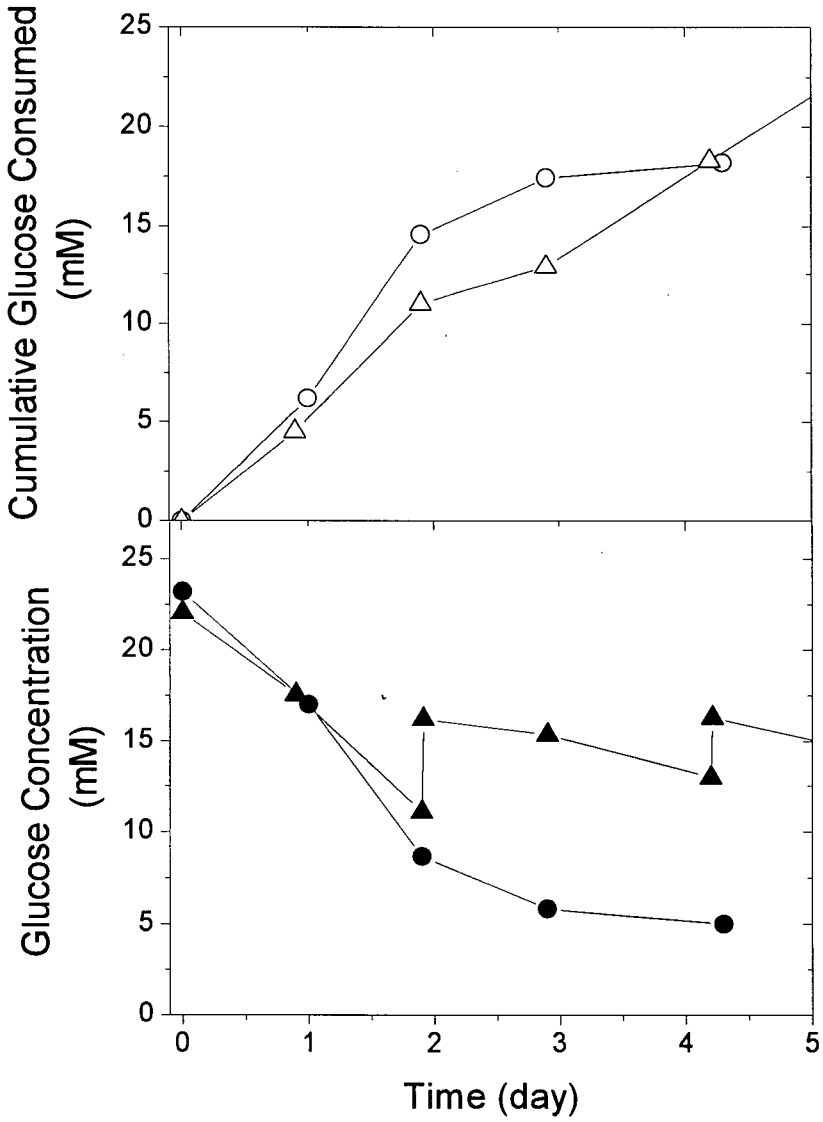

Figure 3.14 The top panel shows the cumulative glucose consumed on a volumetric basis for a hollow fibre bioreactor run (-Δ-) using the Gambro ALWALL Plus 16 cartridge and a batch culture (-○-) started in parallel. The bottom panel displays the glucose concentrations of the HFBR (-▲-) and the batch spinner (-●-). Prior to inoculation, the cartridge underwent a 2 L dead-end rinse. The initial inoculum concentration for both devices was ~4.0×10^5 cells mL^{-1} on a total volume basis. After inoculation, the cartridge was rotated periodically. Medium was DMEM + 5%FBS + 2mM L-glutamine. Fresh medium was added to the HFBR on days 2 and 4, resulting in an increase of the glucose concentration.

3.4. Conclusions

A number of factors that could cause the delay in HFBR start-up were investigated and can be classified as either direct or indirect effects. The rinsing of the HFBR cartridge prior to inoculation, the size of the inoculum, the loss of inoculum to the manifolds and ECS protein polarization can have a direct impact on prolonging the HFBR start-up. In other words, all of these factors reduce the inoculum activity, which could result in an apparently slower growth and an extended start-up period compared to a parallel batch culture. Secondarily, the release of growth inhibiting factors from the settled cells, the possibly significant build-up of ammonium and the decrease in L-glutamine concentration, either individually or in combination, could further indirectly contribute to the start-up delay in HFBRs.

It should be noted that the factors contributing to the delayed start-up were studied individually. When a HFBR is in the midst of a start-up delay, the factors described above can work together and their deleterious effects on cells can be compounded. For example, dying cells in the manifold can release factors causing further cell death and reduce cell growth in other regions in the HFBR. The thermal depletion of L-glutamine during this delay could further reduce the growth of these cells and, in some cases, the combined effects of these factors can lead to start-up failure.

To overcome HFBR start-up difficulties, a number of recommendations can be made. The rinsing of the cartridge can be significantly improved by forcing the rinse medium to pass through the membrane. A larger inoculum size can improve the HFBR start-up,

however, care should be taken to avoid using an inoculum from the late phases of the seed culture. The HFBR cartridge inclination angle can be adjusted and the cartridge rotated periodically during the start-up period to reduce cell accumulation in the ECS manifolds and to minimize the polarization of growth factors in the ECS. Also, the ECS medium could be recirculated to reduce protein polarization. These procedural changes should help to alleviate the problem of settled cells releasing growth inhibiting factors into the bundle region where the viable cells reside, as well as more evenly distribute growth factors in the ECS. Increasing ammonium and decreasing L-glutamine concentrations in the ECS are two other factors that could possibly further prolong the start-up of HFBRs, especially if cells in the ECS are otherwise experiencing a suboptimal growth environment. If a convenient L-glutamine analysis is not available, a practical solution may be to monitor the changes in the ammonium concentration as well as the glucose concentration during start-up. Once the ammonium concentration reaches a level corresponding to significant L-glutamine depletion, fresh L-glutamine could be added to the HFBR. Additional HFBR experiments would be needed to verify that significantly improved start-up are obtained from these recommended methods.

When some these recommendation were performed in conjunction (i.e., improved rinsing, a larger inoculum, rotating the cartridge after inoculation), the start-up delay was reduced significantly. Alleviating the problems that contribute to start-up delay or culture failure in HFBRs should lead to more efficient and rapid production of monoclonal antibodies. With the increasing use of immobilized cell bioreactors for artificial organs and tissue engineering research, these HFBR results should also provide guidance for more optimal start-up of biomedical engineering cultures.

Chapter 4

REDUCED RECOMBINANT PROTEIN PRODUCTION FROM ULTRAFILTRATION HFBR DUE TO HINDERED PROTEIN HARVESTING

4.1. Motivation and Objectives

Ultrafiltration membrane hollow fibre bioreactors (HFBRs) are widely used to culture hybridoma cells to produce gram quantities of highly concentrated monoclonal antibodies. However, there are few reports of using Chinese hamster ovary (CHO) cells in HFBRs despite the frequent use of this cell line as a producer of recombinant proteins. Ryll *et al.* (1990) reported that protein harvest yields from HFBR cultures of baby hamster kidney (BHK) cells decreased with time. They hypothesized that the cell packing became so extreme that the reduced space between cells compromised the ability to harvest the protein product. However, Koska *et al.* (1997) have shown by means of a mathematical model that, at tissue-like densities in HFBRs, cells alone will only moderately reduce fluid flow.

Many cell lines derived from tissues, such as CHO and BHK cells, form an extracellular matrix (ECM) in the space between the cells. When such adherent cell lines grow to packed-cell densities, this extracellular matrix can fill the remaining void space in the ECS volume. Koska *et al.* (1997) have shown via their modelling studies that, for cells surrounded by ECM, the hydraulic conductivity is greatly decreased. This can restrict fluid movement in the ECS so much that the harvest flow would be drawn primarily from the ICS medium, short-circuiting from fibres near the ECS outflow port. Hence, in cases

where significant ECM is present, Koska *et al.* (1997) predicted that the bulk of the product cannot be removed from the reactor and that the harvest concentration will fall well below the average value in the ECS.

In this work, two CHO cell lines producing tissue plasminogen activator (t-PA) were cultured in HFBRs to study the impact of packed-cell density on harvest effectiveness for such cell types and to thereby test the predictions of the Koska *et al.* (1997) model. The experimental plan was to operate the HFBRs until a decline in the protein harvest concentration was observed, and then to sacrifice each reactor so that its ECS content could be analyzed.

4.2. Experimental Procedures

4.2.1. Cell Line and Medium

The CHO cell lines SI12-5.23.23 (Fann *et al.* 2000) and 540/24 (Gorenflo *et al.* 2003) were cultured in serum-free media (SFM1 and SFM2, respectively, Cangene, MB). Thawed cells were first cultured in 75 cm^2 t-flasks, then in 250 mL spinners, and finally in 1 L spinners. Once there were enough cells to inoculate the bioreactor, they were centrifuged at 1,000 g for 10 min and resuspended in a 15 mL volume of the original supernatant. No antibiotic was used in the inoculum cultures in order to allow more rapid detection of any contaminants. The SI12-5.23.23 cells were used in the first two HFBR runs and the 540/24 cells in the third HFBR run.

4.2.2. Hollow Fibre Bioreactor Setup and Culture

Approximately 10^8 cells with ~90% viability were suspended in the 15 mL volume and inoculated into Cell-Pharm® System 100 HFBRs (Unisyn Technologies, Hopkinton, MA). These hollow fibre cartridges had a nominal molecular weight cutoff of 30 kDa. The fibres were composed of regenerated cellulose, and the module had an ECS volume of 12 mL and a fibre surface area of 1.1 m^2. The cells were inoculated at the upstream ECS port according to the procedures recommended by Unisyn Technologies. The pH in the medium reservoir was adjusted to between 7 and 7.4 by controlling the volumetric flow rates of air and CO_2 in the aerator/ventilator.

The HFBRs were operated in batch mode for the first several days. The initial ICS reservoir volume was 1 L. The ICS glucose concentration, initially 25 mM, was measured daily. Each time the glucose concentration decreased to 15 mM or less, 500 mL of the ICS medium was removed and sufficient fresh medium was added to maintain the ICS reservoir volume at the desired level (1 L at the start, increasing to 2 L as the culture requirements increased). HFBR harvesting started 5-7 days after inoculation, and henceforth, the ECS was harvested every 2-3 days. Approximately 8-10 mL were harvested at a flow rate of 5-10 mL min^{-1} from the downstream ECS port while an equal volume of fresh medium was pumped into the upstream ECS port.

4.2.3. Hollow Fibre Cartridge Sectioning

After each run, the hollow fibre cartridges were frozen and sectioned using a modification of the method described by Piret and Cooney (1990b). First, the ICS

medium was pumped from the HFBR and replaced by air. The cartridge was then detached from the system and rapidly placed in a liquid nitrogen bath to freeze the reactor (within 10 min). After storage at –20 °C, the cartridge was sliced into four axial sections in a 4°C cold room. Each section was weighed and then thawed in 8-10 mL of phosphate buffer saline solution. The fibres were dispersed and the samples gently mixed. To determine the cell recovery, aliquots of fibre-free samples were diluted 50-fold in a solution of 0.4% trypan blue and 0.9% NaCl (Sigma, St. Louis MO), and then counted in a hemocytometer.

4.2.4. Cell Lysis Buffer and ε–aminocaproic Acid Wash

In order to recover t-PA inside the ECS at the end of the runs, thawed ECS section samples were treated with cell lysis buffer (5 mM Tris, 15 mM NaCl and 10% w/v NP40, pH 8.0) and 1 mL of each sample was centrifuged at 10,000 g and 4 °C for 20 min. The supernatant was discarded and 1 mL of cell lysis buffer was added to the cell pellet. The cell pellet was dispersed and placed on ice for 30 min. The cell lysate was then centrifuged at 10,000 g and 4 °C for 10 min and the supernatant analyzed by an enzyme-linked immunosorbent assay (ELISA).

The remainder of each cell pellet from the cell lysis buffer wash was treated with an aminocaproic acid solution (0.2 M ε–aminocaproic acid in 0.1 M sodium phosphate buffer, pH 7.4) to release the bound t-PA from the cell debris (Deutsch and Mertz 1970). The samples were dispersed, left on ice for 30 min, and then centrifuged at 10,000 g and 4 °C for 10 min. The supernatant was then analyzed by ELISA.

4.2.5. t-PA ELISA and Activity Assay

The concentration of t-PA was measured using a modification of the assay described by Harlow and Lane (1988). HI72C monoclonal antibody (Life Technologies, Burlington, ON) was used for plate-coating and rabbit anti-t-PA antiserum (Cangene, Winnipeg, MB) was used as the secondary antibody. The immuno-complex formed by the binding of the antibodies and t-PA molecules was detected by alkaline phosphatase conjugated goat anti-rabbit antibodies and alkaline phosphatase substrate (Sigma). Plasma t-PA (Calbiochem, La Jolla, CA) was used as the standard for the ELISA. The samples and the standards were diluted in the same buffer (0.1 M TrisCl, 0.1% v/v Tween 80, 0.1% w/v IMDM/10% v/v FBS medium, pH 8.0). The optical densities of 96-well plates were read at 405 nm using a microtiter plate reader (Molecular Devices, Sunnyvale, CA).

The enzymatic activity of t-PA was analyzed via a modified colorimetric assay (Randy and Wallen 1981; Verheihen *et al.* 1982), described in detail by Dowd *et al.* (2000). Briefly, solutions of plasma t-PA standard and the samples were diluted in buffer (0.1 M TrisCl, 0.1% v/v Tween 80, 0.1% w/v IMDM/10% v/v FBS medium, pH 8.0). The substrate used for the assay was *D*-Val-Leu-Lys-*p*-Nitroanilide dihydrochloride (0.5 mM, Sigma). The cleaved substrate was detected at 405 nm using the microtiter plate reader. For ease of comparison between the ELISA and the activity assay results, the World Health Organization (WHO) conversion factor of 580 U μg^{-1}, based on the t-PA standard provided, was used.

4.3. Results and Discussion

The t-PA harvest concentrations measured by ELISA for HFBR run #1 (Figure 4.1), increased gradually from 50 μg mL^{-1} on day 6 up to 95 μg mL^{-1} on day 21 and then dropped precipitously to approximately 10 μg mL^{-1}, where it remained until the end of

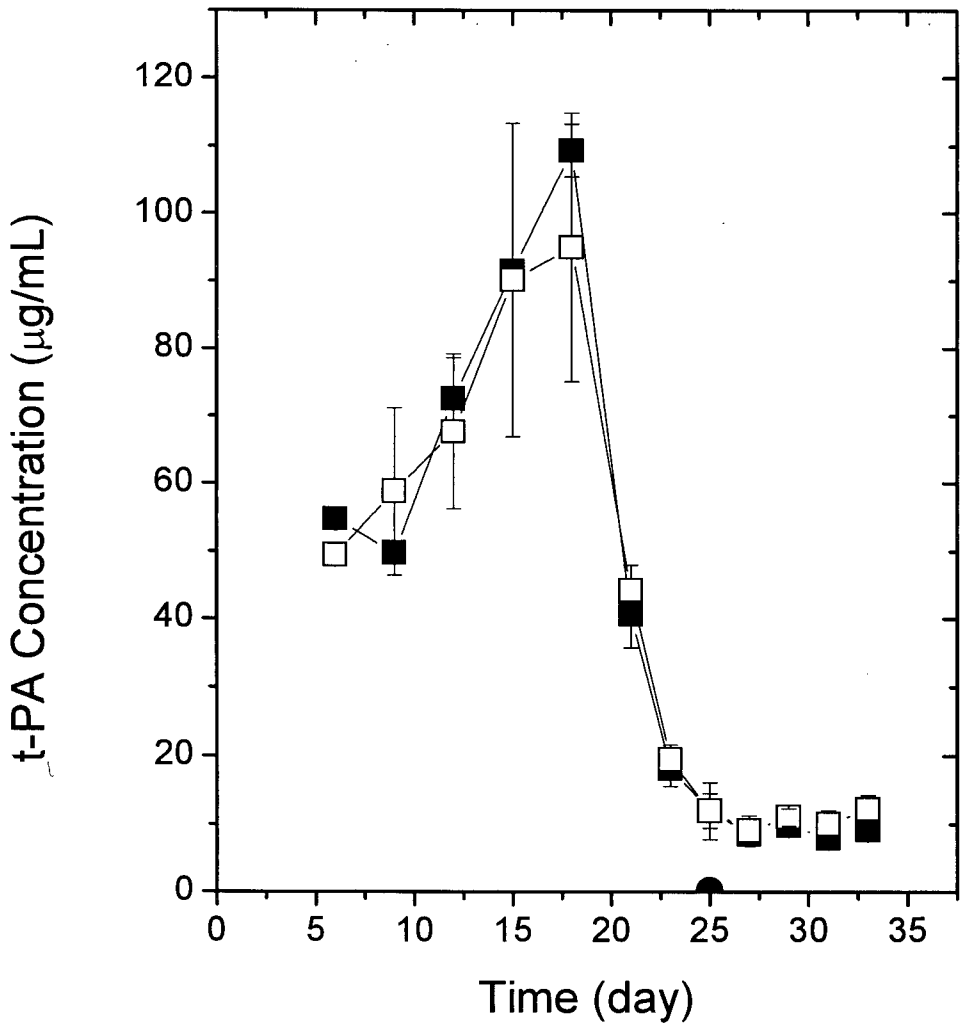

Figure 4.1 The ECS t-PA concentration profile (-□-) (ELISA) for run #1 for the CHO cell line SI12-5.23.23. The data from the t-PA activity assay (-■-) were converted to concentration based on the conversion factor 580 U μg^{-1}. The ICS sample (●) was measured by ELISA. Each harvest volume was approximately 10 mL. The error bars are the standard deviations of duplicate assay results.

the run. The low ELISA result for the ICS sample (Figure 4.1) indicates that essentially none of the t-PA produced in the ECS leaked to the ICS. The t-PA content of the ECS harvest was also measured by the t-PA activity assay. Based on the WHO conversion factor, the t-PA activity assay gave very similar results, confirming those obtained from the ELISA assay and indicating little to no inactivation of the t-PA molecules. The total amount of t-PA harvested during run #1 was 6,590 μg. Since the activity assay and the t-PA ELISA results were comparable, only the activity assay was performed to determine the ECS concentrations in subsequent runs, though for clarity, the results are expressed in units of $\mu g\ mL^{-1}$.

The harvested product versus time profile from a replicated HFBR run was similar to that of the first run (Figure 4.2). However, the glucose uptake rates of run #2 were about 40% higher than those of run #1. The starting concentration of the harvest from HFBR run #2 was 58 $\mu g\ mL^{-1}$ and reached a maximum t-PA concentration of 69 $\mu g\ mL^{-1}$, somewhat lower than in run #1. After day 20, the t-PA concentration suddenly dropped to 5 $\mu g\ mL^{-1}$ and then levelled off at approximately 16 $\mu g\ mL^{-1}$ (Figure 4.2), similar to the sharp decline observed in run #1. These results were consistent with the Koska *et al.* (1997) prediction that packed CHO cells with extracellular matrix may prevent effective harvesting. The total amount of t-PA harvested during run #2 was 3,760 μg, approximately half of the total amount of t-PA harvested from run #1. The differences in the glucose uptake rate and the total amount of t-PA harvested were greater than typical run-to-run variations in mammalian cell culture. Nonetheless, the significant declines in harvested t-PA concentration around day 20 strongly suggest that, for both runs, the mass

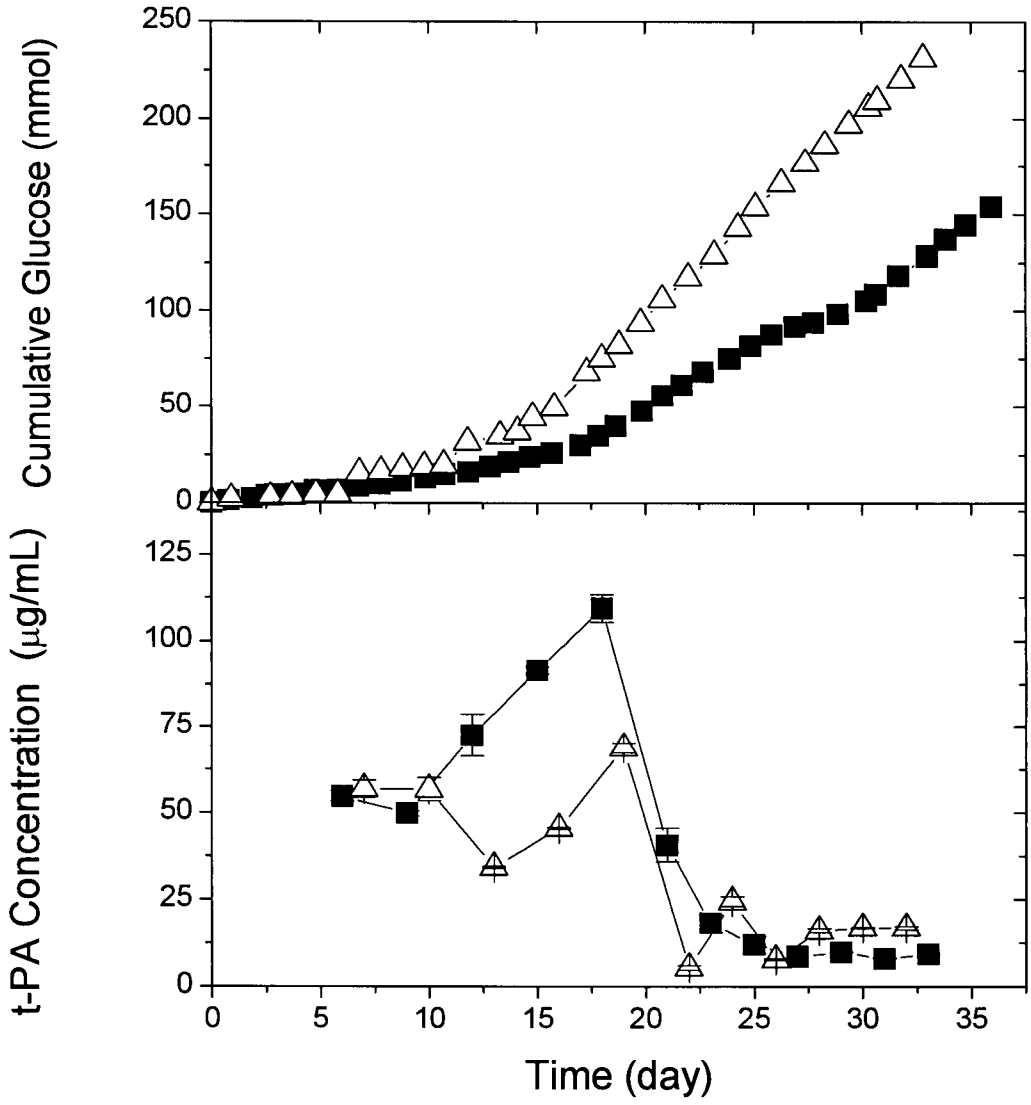

Figure 4.2 The top panel shows the cumulative glucose consumption profiles for run #1 (-■-) and run #2 (-Δ-) for the CHO cell line SI12-5.23.23. The bottom panel displays the t-PA concentrations from run #1 (-■-) and run #2 (-Δ-) based on the activity assay. Each harvest volume was approximately 10 mL. The error bars are the standard deviations of duplicate assay results.

transport limitation to protein harvesting predicted by Koska *et al.* (1997) does take place.

After 35 days, the cartridge from HFBR run #1 was frozen, sectioned and analyzed. The average t-PA concentration inside the cartridge was approximately 130 μg mL^{-1} with concentrations higher in the middle sections of the cartridge than in the two end sections (Figure 4.3). The t-PA was not polarized towards the downstream end of the HFBR as was the case for Piret and Cooney (1990a), at least in part because an ECS harvest was carried out only 30 min before the cartridge was frozen. Also, at high CHO cell concentrations, ECS polarization would be diminished (Koska *et al.* 1997). The average recovered cell concentration from the cartridge ECS was approximately $1.3x10^8$ cells mL^{-1}, corresponding to the visual observation of a tissue-like density in most of the cartridge. Cell recoveries from the ECS were considerably less than 100%, given the freeze/thaw cell damage combined with shear during recovery (Piret and Cooney 1990a).

The cartridge from HFBR run #2 was analyzed after 33 days. The average ECS t-PA concentration was approximately 80 μg mL^{-1}, lower than the value from run #1. The axial t-PA distribution for run #2 was relatively uniform (Figure 4.3), for unknown reasons since it was also harvested about 30 min prior to freezing. The total amount of t-PA recovered from the ECS supernatants at the end of the run were 1,300 μg and 990 μg for runs #1 and #2, respectively, consistent with the relatively greater harvest from run #1. The average cell concentration in the cartridge was $\sim 10^8$ cells mL^{-1} (approximately two orders of magnitude greater than that in a batch culture), again, confirming the observation of cell-packed conditions in most of the ECS. As had been qualitatively

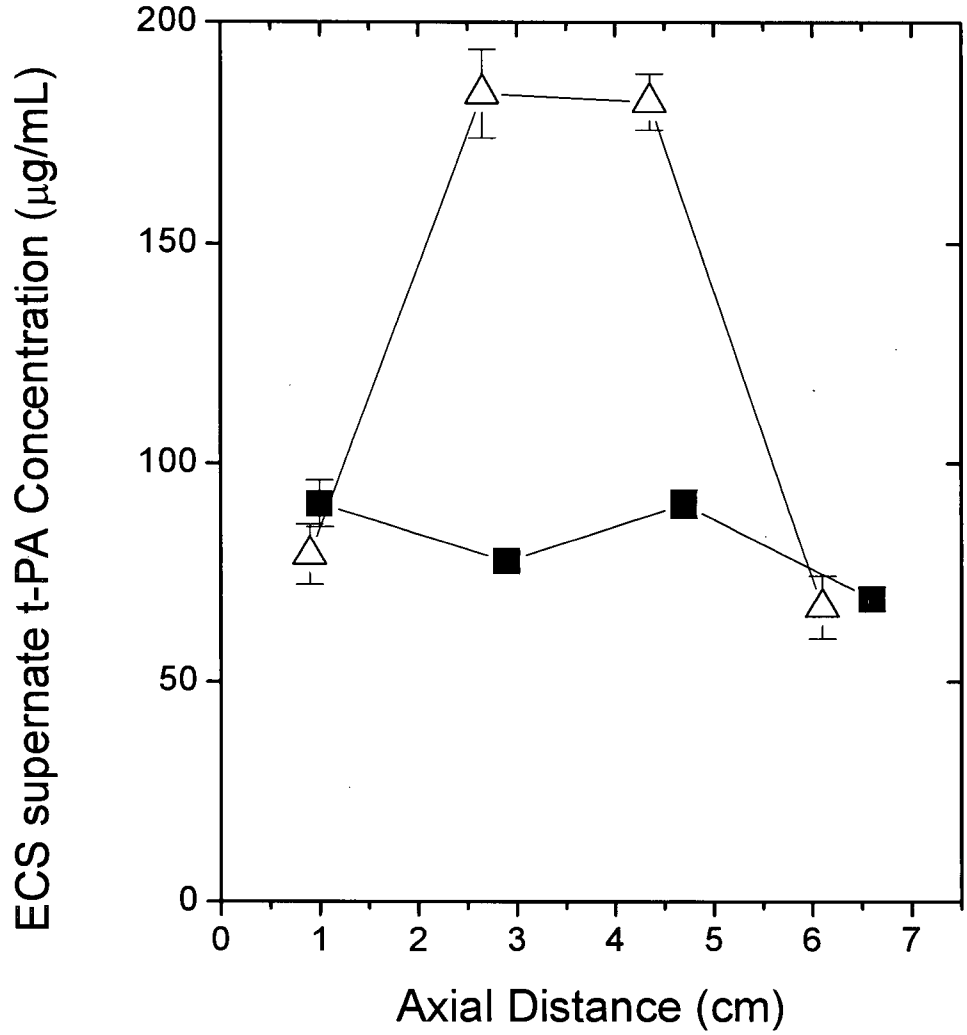

Figure 4.3 Axial ECS supernatant t-PA concentrations recovered from HFBR cartridges at the end of run #1 (-Δ-) and run #2 (-■-). The axial distance of zero represents the upstream end of the cartridge bundle. The points are plotted at the mid-position of each axial section. The error bars are the standard deviations of duplicate assay results.

predicted by Koska *et al.* (1997), in both runs, the harvest concentration from day 20-21 onwards (9-16 μg mL^{-1}) was about an order of magnitude lower than the ECS t-PA supernatant concentration measured at the end of the runs (70-180 μg mL^{-1}). The higher concentration retained in the ECS could be another indicator that harvesting was not

effective. However, it is also possible that these higher ECS concentrations were caused by t-PA released by the cells during the freeze/thaw procedure. In addition, the analysis of ECS t-PA is complicated by t-PA binding to cell debris (see below).

The analysis of these results was further complicated when Dowd *et al.* (2000) discovered that, in the presence of extracellular t-PA concentrations greater than 0.5 $\mu g\ mL^{-1}$, the specific t-PA productivity of these SI12-5.23.23 CHO cells significantly decreased (although their growth rate was not affected). Since HFBRs concentrate recombinant proteins in the ECS, this unusual inhibition of t-PA production by extracellular t-PA was likely magnified and, consequently, could also have contributed to the drop in the t-PA harvest concentration observed in runs #1 and #2.

A 540/24 CHO cell line, which does not exhibit such inhibition of t-PA production, was investigated in HFBR run #3 to ensure that t-PA inhibition alone could not explain the above results. As can be seen from Figure 4.4, the starting concentration of the harvest from run #3, at 313 $\mu g\ mL^{-1}$, was significantly higher than the corresponding values in runs #1 and #2 (typical t-PA concentration at the end of a batch culture of 540/24 CHO cells is ~50 $\mu g\ mL^{-1}$). The glucose uptake rate profile, an indicator of the metabolic activity in the HFBR, was similar, in run #3, to those of the two previous HFBR runs. The high concentration of the first harvest at day 8 was likely due to the increased production in the absence of feedback inhibition for this cell line. However, the harvest concentration steadily decreased to 20 $\mu g\ mL^{-1}$ by day 20 and then dropped below

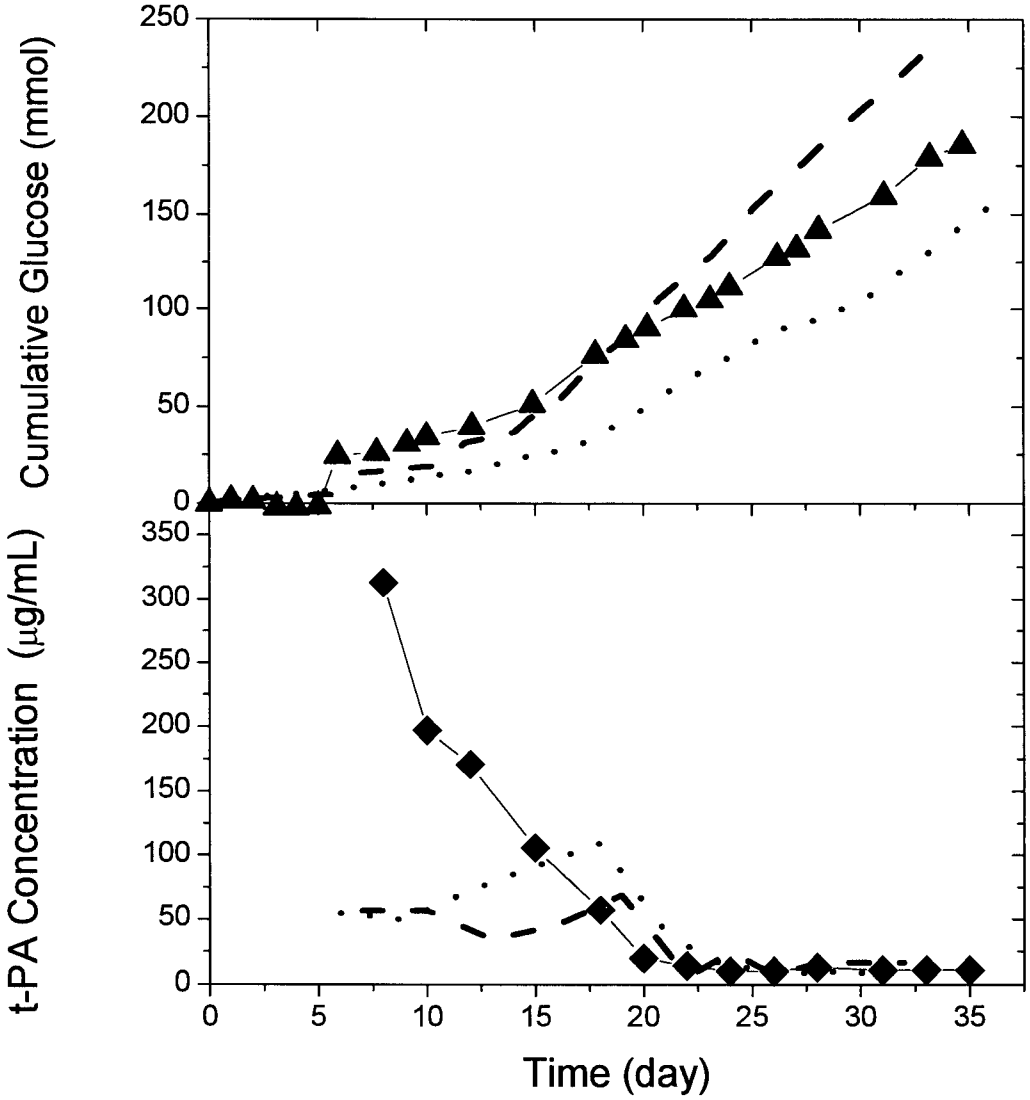

Figure 4.4 The top panel shows the cumulative glucose consumption profile for HFBR run #3 using the CHO 540/24 cell line (-▲-). The bottom panel displays the t-PA concentrations of the harvest samples from run #3 using the new cell line (-♦-). The dotted and dashed lines are the corresponding results from runs #1 and #2 (Figure 4.2), respectively, shown for comparison. Each harvest volume was approximately 10 mL.

13 μg mL^{-1} where it remained until the end of the run (Figure 4.4). This drop in harvest concentration is likely caused by the accumulation of ECM in the ECS that is predicted to prevent the effective harvesting of t-PA. The total amount of t-PA harvested during run

#3 was 8,170 μg, somewhat higher but still comparable to the values obtained in the first two runs.

At the end of run #3, the cartridge was frozen, sectioned and analyzed. The axial t-PA distribution was relatively uniform (Figure 4.5), averaging approximately 60 μg mL^{-1}. The total t-PA in the cartridge supernatant was 720 μg. The average cell concentration in the cartridge was $1.8x10^8$ cells mL^{-1}, and also visibly tissue-like. The average ECS t-PA supernatant concentration in run #3 was higher than the t-PA harvest concentration at the end of the run, once again suggesting that the cartridge was being ineffectively harvested. Koska *et al.* (1997) predicted that lower harvest concentrations would result from the fact that a significant portion of the harvest medium passes through the ECS from the ICS, as the ECM and the packed ECS permeabilities become lower than the membrane permeability. In addition, free "channels" (i.e., passageways having relatively low cell concentrations) were observed in the ECS as each run progressed. Some of the fresh medium, differentiated by its bright red color, was observed to by-pass the bulk of the ECS cell mass through these free "channels" during the harvesting of cartridges that were otherwise packed with cells. This additional by-passing of the ECS cell mass also likely contributed to the lower concentration of the t-PA harvest.

The sectioned cartridge samples from runs #2 and #3 were treated with cell lysis buffer to release any t-PA remaining trapped inside the cells. After treating the samples twice with the buffer and analyzing by ELISA, more t-PA was measured compared to the total amount harvested during the runs or in the cartridge supernatant (Table 4.1). The t-PA recovered from this cell lysis step (Table 4.1) may also be released from the ECM or

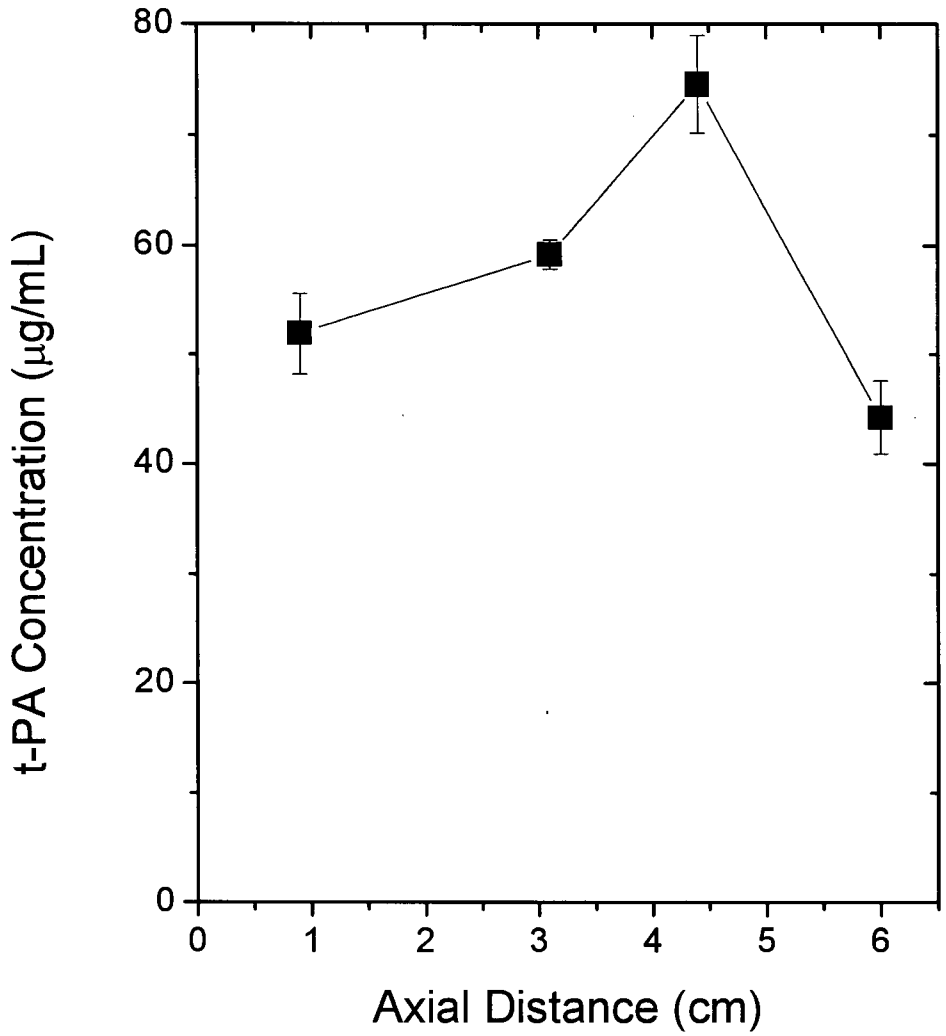

Figure 4.5 Axial supernatant t-PA concentrations recovered from the reactor cartridge at the end of run #3 (-■-). The axial distance of zero represents the upstream end of the cartridge bundle. The points are plotted as the mid-position of each axial section. The error bars are standard deviations of duplicate assay results.

other surfaces by the cell lysis buffer. The larger amount of t-PA measured from cell lysis treatment for run #2 compared to run #3 can be explained by the Dowd *et al.* (2000) finding of greater intracellular t-PA in the SI12-5.23.23 cells compared to the 540/24 cells. To immoblize t-PA at the site of a clot, the molecule contains a lysine binding

domain (Verheihen *et al.* 1982). Since the t-PA molecule could also bind to free lysine residues in the cell debris, a lysine analog, ε–aminocaproic acid, was used to recover more of the bound t-PA. An additional 6,000 and 19,500 μg of t-PA were recovered in this fashion from cartridges #2 and #3, respectively (Table 4.1). The lower amount recovered from run #2 is consistent with the fact that the secretion of t-PA for the SI12-5.23.23 cells is inhibited by the extracellular t-PA. This binding property of t-PA may make HFBRs particularly unsuitable for the production of t-PA, especially later in the culture when the ECS contains a significant fraction of nonviable cells (Piret and Cooney 1990a). However, it should be noted that the freeze/thaw method used to recover the ECS content lyses many of the viable cells (Piret and Cooney 1990a) and thereby may exaggerate this phenomenon.

One possible method to improve product recovery from HFBRs culturing cells with ECM is to subject the ECS to additional convection, i.e. by circulating medium in the ECS. Gramer *et al.* (1999) has reported increased monoclonal antibody recovery with an extracapillary (EC) space convection system (using circulation and cycling) for

Table 4.1 Summary of results from two hollow fibre bioreactor runs (12 mL ECS volume).

	Run #2 (SI12-5.23.23 cell line) (μg)	Run #3 (540/24 cell line) (μg)
t-PA harvested	3,760	8,170
t-PA in the cartridge supernatant [1]	990	720
t-PA released by cell lysis [2]	28,700	14,600
t-PA released by a lysine analog [3]	6,000	19,500

[1] t-PA activity measurement at the end of each run.
[2] t-PA ELISA measurement after washing cells with cell lysis buffer.
[3] t-PA ELISA measurement after washing cells with 200 mM aminocaproic acid solution

hybridoma cells. There are currently no reports of using EC circulation or cycling for cells producing ECM. It is likely that the use of EC circulation could partially improve the product recovery from CHO-type cells, but it remains to be seen whether EC circulation could substantially overcome the reduced permeability caused by the ECM.

4.4. Conclusions

The observed drop in the t-PA harvest concentration for two different CHO cell lines supports the model predictions of Koska *et al.* (1997) and indicates that product recovery is significantly hindered for cells that produce extracellular matrix. If product inhibition occurs or the product binds to the cells, the special ability of HFBRs to concentrate products in the ECS can also become a disadvantage as the ECS eventually becomes filled with both viable and nonviable cells. The results of this study help to explain why HFBRs, as opposed to stirred tank bioreactors, are so rarely used for recombinant protein production from CHO-type cell lines, while they remain widely used for small scale hybridoma monoclonal antibody production. Less ambivalent data in support of the Koska *et al.* (1997) model prediction might be obtained if another protein, without the binding properties of t-PA to lysine residues, was used.

Chapter 5

TWO-DIMENSIONAL ANALYSIS OF PH DISTRIBUTION IN HOLLOW FIBRE BIOREACTORS

5.1. Introduction

Mathematical modeling is an important tool for engineers and scientists. In process optimization, the use of mathematical models can provide prediction of results for many possible sets of input variables without the need for performing time consuming experiments. In addition, mathematical models can provide valuable information and insight for systems where experiments cannot be easily performed. From models, detailed knowledge of the process behaviour can be obtained and the optimization of the process can be carried out more efficiently.

The accumulation of carbon dioxide in high cell density bioreactors is an important issue that has been previously discussed (Aunins and Henzler 1993; Ozturk *et al.* 1995; Gray *et al.* 1996; deZengotita *et al.* 1998; Zupke and Green 1998). Since carbon dioxide is a principle end product of cellular metabolism, the buildup of carbon dioxide in packed cell HFBRs can become an important concern. Dissolved carbon dioxide interacts with bicarbonate in the medium, affecting the pH of the system. It is well-known that the viability of animal cells can be very sensitive to even small changes in pH (Freshney 1994).

Lactate is one of the main metabolites produced by cultured cells (Thomas 1990). Lactic acid is primarily generated from the conversion of glucose by the glycolytic pathway

(Zeilke *et al.* 1984; Batt and Kompala 1989). Lesser amounts of lactic acid can also be produced from L-glutamine metabolism (Zeilke *et al.* 1984). In the pH range of 6-8, most of the lactic acid (with a pKa of 3.9) is readily dissociated in water (Oetzel 2003). Hence, in the model, lactic acid produced by cells in the ECS is another source of H^+ ions.

A mathematical model that describes not only the transport of carbon dioxide and its equilibrium kinetics, but also the generation of lactic acid in HFBRs can provide information about the detailed pH distribution in the cell-packed region of the bioreactor. The model inputs include the recirculation flow rate, the ICS inlet concentrations of all species, the cell specific generation rates of CO_2 and lactic acid, and the number of cells in the HFBR. The mathematical model is described in the following sections.

5.2. Mathematical Model

5.2.1. Model Description

The "Krogh Cylinder" approximation is typically used in modelling HFBR hydrodynamics and mass transfer (Labecki *et al.* 1995; Patkar *et al.* 1995; Labecki *et al.* 1996). Here one assumes that the fluid and solute behaviours in the vicinity of each fibre are the same, such that a multi-fibre bioreactor can be represented by a single fibre surrounded by an annular fluid envelope (Krogh 1919). The control volume was therefore defined to be a Krogh cylinder with a packed annular layer of cells in the ECS. Its geometry consists of three concentric cylinders (Figure 5.1). The innermost cylinder, with radius R_L, represents the intracapillary space (ICS) where the medium is recirculated. The outermost cylinder represents the packed cells growing in the extracapillary space

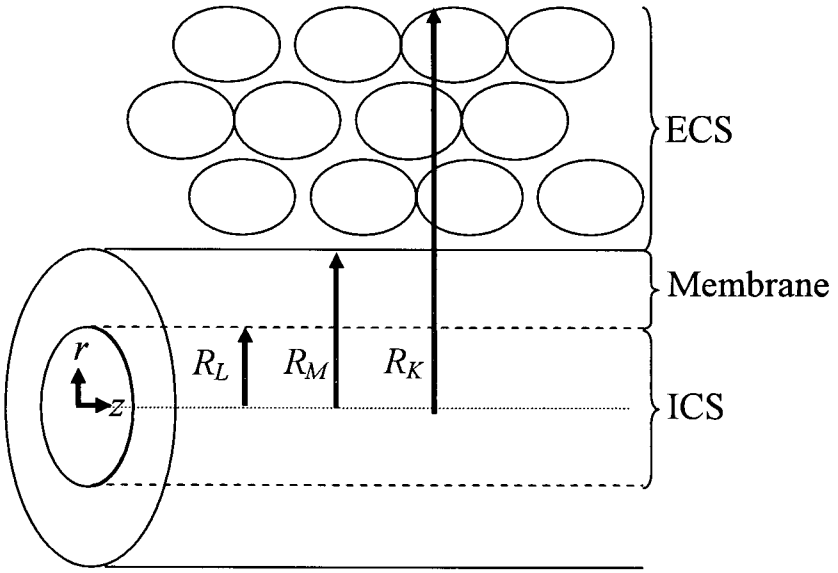

Figure 5.1: Krogh cylinder approximation used for the HFBR mass transfer model.

(ECS). R_K is the Krogh cylinder radius. Between the ICS and the ECS is the cylindrical membrane wall. R_M represents the outer membrane radius.

It has been shown that, under typical HFBR operating conditions, diffusion is the primary transport mechanism in the radial direction for low-molecular weight nutrients and metabolites (Webster and Shuler 1978; Piret and Cooney 1991). Therefore, a two-dimensional Krogh cylinder approximation will be used to estimate the local concentrations of carbon dioxide (CO_2), carbonic acid (H_2CO_3), bicarbonate ion (HCO_3^-), carbonate ion (CO_3^{-2}), hydroxyl ion (OH^-), hydrogen ion (H^+), and lactate ion ($CH_3CHOHCO_2^-$) in the ICS, membrane, and ECS.

The mathematical model was based on the resolution of the conservation of mass equation for each of these seven species in cylindrical coordinates for the Krogh cylinder geometry shown in Figure 5.1.

5.2.2. Conservation of Mass Equation for Each Species

Several assumptions were made to allow the development of a simple but representative model. To mimic typical operating conditions in a HFBR, the temperature is taken to be at 37°C throughout the Krogh cylinder. If it is therefore assumed that the diffusion coefficient is constant in each of the three regions, then the general form of the steady-state mass continuity equation in cylindrical coordinates is:

$$v_r \frac{\partial C_{i,j}}{\partial r} + v_z \frac{\partial C_{i,j}}{\partial z} = D_{i,j}\left(\frac{1}{r}\frac{\partial}{\partial r}\left(r\frac{\partial C_{i,j}}{\partial r}\right) + \frac{\partial^2 C_{i,j}}{\partial z^2}\right) + r_{i,j} \qquad (5.1)$$

where $C_{i,j}$ is the local concentration (mol m^{-3}) of species i in region j, v_r and v_z are the fluid velocity components (m s^{-1}) in the r and z directions, respectively, and $D_{i,j}$ is the diffusion coefficient (m^2 s^{-1}) of the chemical species i in region j. The kinetic term, $r_{i,j}$, represents the net production of species i per unit volume of region j due the reversible reactions between the species. In the ECS, this term also represents the evolution of CO_2 by cells and the addition of H^+ and lactate ions from the production of lactic acid.

Based on the calculations of Piret and Cooney (1991) for oxygen transfer in HFBRs, axial convection dominates the mass transport in the ICS, and hence the radial convective term in this region can be neglected. Using an order of magnitude analysis based on the entrance length to diameter ratio of the Krogh cylinder ($L/2R_K$~1000), the axial diffusive fluxes in the ICS, membrane and ECS were also found to be negligible compared to the radial diffusive fluxes. Furthermore, because of the low permeability of both the hollow fibre membrane and the cell-packed ECS, it is assumed that there is insignificant convective fluid exchange between the ICS and the ECS, i.e., that v_r=v_z=0 in the

membrane and ICS. Thus, after simplification, the continuity equations for the ICS, membrane, and ECS are reduced to:

$$
\begin{aligned}
&ICS: && v_z \frac{\partial C_{i,ICS}}{\partial z} = D_{i,ICS}\left(\frac{1}{r}\frac{\partial}{\partial r}\left(r\frac{\partial C_{i,ICS}}{\partial r}\right)\right) + r_{i,ICS} \\
&Membrane: && 0 = D_{i,MEM}\left(\frac{1}{r}\frac{\partial}{\partial r}\left(r\frac{\partial C_{i,MEM}}{\partial r}\right)\right) + r_{i,MEM} \\
&ECS: && 0 = D_{i,ECS}\left(\frac{1}{r}\frac{\partial}{\partial r}\left(r\frac{\partial C_{i,ECS}}{\partial r}\right)\right) + r_{i,ECS}
\end{aligned}
\qquad \textbf{(5.2)}
$$

where the subscripts *ICS*, *MEM* and *ECS* have the obvious meanings.

With appropriate boundary conditions, such as the known initial concentrations entering the ICS, axisymmetry in the ICS, continuity of the radial fluxes at the ICS/membrane and membrane/ECS interfaces, and the absence of radial gradients at the Krogh cylinder radius (i.e., no transfer of species between cylinders), one can use finite difference methods to calculate the radial concentration profile of all species at any axial position in the HFBR. The boundary conditions are:

$$
\begin{aligned}
&z = 0 && C_{i,ICS} = C_{i,ICS,0} \\
&r = 0 && \frac{\partial C_{i,ICS}}{\partial r} = 0 \\
&r = R_L && D_{i,ICS}\left(\frac{\partial C_{i,ICS}}{\partial r}\right) = D_{i,MEM}\left(\frac{\partial C_{i,MEM}}{\partial r}\right) \\
&r = R_M && D_{i,MEM}\left(\frac{\partial C_{i,MEM}}{\partial r}\right) = D_{i,ECS}\left(\frac{\partial C_{i,ECS}}{\partial r}\right) \\
&r = R_K && \left(\frac{\partial C_{i,ECS}}{\partial r}\right) = 0
\end{aligned}
\qquad \textbf{(5.3)}
$$

5.2.3. CO_2 Evolution and Lactate Production Rates

The ECS of the HFBR is assumed to be uniformly packed with cells at a tissue density of X (cell m^{-3}) having a uniform specific carbon dioxide evolution rate of *sCER* (mol $cell^{-1}$ s^{-1}) and a specific lactic acid production rate of *sLPR* (mol $cell^{-1}$ s^{-1}). It is also assumed that any lactic acid produced immediately dissociates into hydrogen and lactate ions via the reaction:

$$CH_3CHOHCOOH \rightarrow CH_3CHOHCOO^- + H^+ \tag{5.4}$$

Thus, in the ECS, the evolution of CO_2 contributes to the carbon dioxide kinetic term according to:

$$r_{CO_2,ECS} = sCER \cdot X \tag{5.5}$$

Similarly, the production of lactic acid contributes directly to the hydrogen ion and lactate ion kinetic terms as

$$\begin{aligned} r_{H^+,ECS} &= sLPR \cdot X \\ r_{CH_3CHOHCOO^-,ECS} &= sLPR \cdot X \end{aligned} \tag{5.6}$$

The density of cells in tissues has been reported to be about $3x10^{14}$ cell m^{-3} (Freshney 1994). A specific carbon dioxide evolution rate of $8.33x10^{-18}$ mol $cell^{-1}$ s^{-1} was reported by Gray *et al.* (1996) for Chinese hamster ovary (CHO) cells in high density perfusion cultures. Other reported specific carbon dioxide evolution rates were. $4.42x10^{-17}$ mol $cell^{-1}$ s^{-1} for SF-9 cells in a stirred tank bioreactor (Kamen *et al.* 1991), $8.21x10^{-17}$ mol $cell^{-1}$ s^{-1} for CHO cells in microcarriers cultures (Lovrecz *et al.* 1992), and $1.07x10^{-17}$ mol $cell^{-1}$ s^{-1} for NS0 myeloma cells in a fed-batch culture (Aunins and Henzler 1993). The specific lactic acid production rate of $1.35x10^{-17}$ mol $cell^{-1}$ s^{-1} was estimated from batch culture data for TFL-P9 hybridoma cells obtained in previous experiments (see Chapter

3). Other reported specific lactate production rates were in the range from 3.61×10^{-17} to 1.25×10^{-16} mol cell^{-1} s^{-1} for murine hybridoma cells in a stirred tank culture (Ozturk *et al.* 1992; Ong *et al.* 1994).

5.2.4. Equilibrium Reactions

The following detailed equilibrium reaction for the dissolution of gaseous CO_2 in aqueous solution was provided by Soli and Byrne (2002):

$$CO_2(aq) + H_2O \underset{k_D}{\overset{k_H}{\rightleftharpoons}} H_2CO_3 \overset{K_{a1}}{\rightleftharpoons} H^+ + HCO_3^- \overset{K_{a2}}{\rightleftharpoons} H^+ + CO_3^{-2} \qquad (5.7)$$

The hydration/dehydration reaction, or the first step in the sequence of reactions, was assumed to be the rate limiting step. The subsequent reactions in the sequence were assumed to achieve equilibrium instantaneously. Rate constants for the first acid dissociation of carbonic acid ($H_2CO_3 \leftrightarrow H^+ + HCO_3^-$) were reported to be 8×10^6 s^{-1} for the forward reaction, and 4.7×10^{13} mol m^{-3} s^{-1} for the reverse reaction (Edsall 1969). These values clearly exceed those of the hydration/dehydration reaction, where the dehydration, k_D, and the hydration, k_H, constants were reported to be 50.2 s^{-1} and 0.057 s^{-1}, respectively, at 32.5°C (Soli and Byrne 2002). Since the pK value of the second dissociation reaction ($HCO_3^- \leftrightarrow H^+ + CO_3^{-2}$) was reported to be 10.3 (Harned and Davis 1943) at the normal operating pH of the bioreactor, the overall reaction yields only very small amounts carbonate ion (CO_3^{-2}).

To determine the equilibrium concentrations of the five species, H_2CO_3, HCO_3^-, CO_3^{-2}, H^+ and OH^-, involved in the equilibrium reactions, the following five non-linear equations were written and then solved as a set:

$$[HCO_3^-]+2[CO_3^{-2}]+[OH^-]-[H^+]+[CH_3CHOHCOO^-]-[Na^+]_0+[Cl^-]_0=0 \quad \textbf{(5.8)}$$

$$K_{a1}[H_2CO_3]-[HCO_3^-]\cdot[H^+]=0 \quad \textbf{(5.9)}$$

$$K_{a2}[HCO_3^-]-[CO_3^{-2}]\cdot[H^+]=0 \quad \textbf{(5.10)}$$

$$K_W-[OH^-]\cdot[H^+]=0 \quad \textbf{(5.11)}$$

$$C_T-[HCO_3^-]-[CO_3^{-2}]-[H_2CO_3]-[CO_2]=0 \quad \textbf{(5.12)}$$

Equation 5.8 represents the electroneutrality balance for the system. Note that this equation requires the lactate ion concentration which is determined locally by solving the differential mass balance (Equation 5.2) for this species. Equation 5.8 also needs the concentration of Na^+ ions, which are present in the system due to the complete dissociation of sodium bicarbonate ($NaHCO_3$), used as a buffer, and the complete dissociation of NaCl. The latter is also a source of Cl^- ions, whose concentration is also required in Equation 5.8. Because Na^+ and Cl^- are not generated by cells, nor involved in equilibrium reactions, their concentrations are assumed to be constant at the values of $[Na^+]_0$ and $[Cl^-]_0$ (mol m^{-3}), respectively, throughout the HFBR. Consequently, mass balance equations for these two species are not required.

The first and second acid dissociation equilibria of HCO_3 are represented by Equations 5.9 and 5.10, respectively, where K_{a1} is 1.023 mol m^{-3} (Sperandio and Paul 1997) and K_{a2} is 5.62×10^{-8} mol m^{-3} (Pankow 1991) at 32.5°C. These rate constants were obtained for sea water, which is similar to culture medium. The water dissociation reaction, which is needed to determine the local concentration of OH^- ions, is represented by Equation 5.11, where K_W is 2.24×10^{-8} mol^2 m^{-6} for water at 37°C (Lide 2004).

The local total carbon species balance for the system is shown in Equation 5.12, where C_T is the total carbon present at that location including the CO_2 evolved by the cells. The carbon dioxide concentration, $[CO_2]$, required by this equation is obtained by applying Equation 5.2 to this species.

Before the mass balance equations, given generally by Equation 5.2, can be solved to determine the distributions of CO_2, H_2CO_3, HCO_3^-, CO_3^{-2}, H^+, OH^-, and $CHO_3CHOHCOO^-$, the kinetic term, $r_{i,j}$, must be specified for all seven species. These kinetic terms are based on both reaction kinetics and species generation from cells. For CO_2 and H_2CO_3 in the ICS and membrane, the kinetic terms involve only the forward and reverse reactions of the hydration/dehydration steps, i.e.,

$$\begin{aligned} r_{CO_2,j} &= -k_H \cdot C_{CO_2,j} + k_D \cdot C_{H_2CO_3,j} \\ r_{H_2CO_3,j} &= k_H \cdot C_{CO_2,j} - k_D \cdot C_{H_2CO_3,j} \end{aligned} \qquad \textbf{(5.13)}$$

where j = *ICS, MEM.* For the remaining species, i = H^+, OH^-, HCO_3^-, CO_3^{2-}, and $CH_3CHOHCOO^-$, there are no kinetic terms, i.e., $r_{i,j} = 0$, $j = ICS, MEM$.

For the ECS, the complete kinetic terms required for CO_2, H_2CO_3, H^+ and lactate are as follows:

$$\begin{aligned} r_{CO_2,ECS} &= -k_H C_{CO_2,ECS} + k_D C_{H_2CO_3,ECS} + X \cdot sCER \\ r_{H_2CO_3,ECS} &= k_H C_{CO_2,ECS} - k_D C_{H_2CO_3,ECS} \\ r_{H^+,ECS} &= X \cdot sLPR \\ r_{CH_3CHOHCOO^-,ECS} &= X \cdot sLPR \end{aligned} \qquad \textbf{(5.14)}$$

As discussed previously, the $X{\cdot}sCER$ term is the source term for the CO_2 produced in the ECS. Similarly, $X{\cdot}sLPR$ is the source term for both H^+ and $CH_3CHOHCOO^-$ assuming

that lactic acid dissociates immediately after being produced by the cells in the ECS. For the remaining species, $i = OH^-$, HCO_3^-, and CO_3^{2-}, in the ECS, $r_{i,ECS} = 0$.

5.2.5. ICS Velocity Distribution

In the HFBR, the ICS flow rate was generally varied between 210 and 860 L day^{-1} (or 150 to 600 mL min^{-1}). When taking into account the fact that the HFBR has approximately 10,500 fibres, the flow rate through each fibre is between 0.021 to 0.082 L day^{-1}. The *Reynolds numbers* for these flow rates (2.1 to 8.3) corresponds to the laminar regime (Re < 2,100). Furthermore, because the length to internal diameter ratio of each fibre is typically about 10^3, it is expected that the z velocity component should have a fully-developed laminar profile over almost the full length of the ICS. Hence, for the ICS,

$$v_z = \frac{3}{2} v_{z,avg} \left(1 - \frac{r^2}{R_L^{\,2}} \right) \qquad \textbf{(5.15)}$$

where $v_{z,avg}$ is the average fluid velocity in each fibre lumen. Equation 5.15 also assumes that the medium flowing through the ICS can be treated as a Newtonian fluid, since cell culture medium is composed mostly of water.

5.3. Hollow Fibre Bioreactor Specification and System Parameters

5.3.1. HFBR Geometric Parameters

For all mathematical simulations, the geometric parameters for a Gambro ALWALL Plus 16 ultrafiltration cartridge (Hechingen, Germany) were used. The fibre and reactor

dimensions as well as the membrane permeability of a similar Gambro cartridge were reported in various publications (Labecki *et al.* 1995; Patkar *et al.* 1995; Labecki *et al.* 1996; Labecki *et al.* 1998; Labecki *et al.* 2001). The values of the fibre geometric characteristics used in the present simulations are given in Table 5.1.

Table 5.1 Gambro ALWALL Plus 16 cartridge specifications

Parameter	Variable	Value
Inner fibre radius (m)	R_L	0.000105
Outer fibre radius (m)	R_M	0.000113
Krogh cylinder radius (m)	R_K	0.000161
Fibre length (m)	L	0.21
Number of fibres	N	10,500

5.3.2. Species Diffusion Coefficients

To properly simulate mass transfer in a HFBR, reasonable estimates of the diffusion coefficients in the cell culture medium, membrane, and packed-cell ECS, for all seven species involved in mass transfer and chemical equilibria are required. A wide range of diffusion coefficients have been reported in the literature for these seven species, as shown in Table 5.2. The diffusion coefficients for CO_2 varied from 0.34×10^{-9} m^2 s^{-1} at 37°C in a hemolysate solution (Uchida *et al.* 1983) to 1.104×10^{-9} m^2 s^{-1} in tissue (Swabb *et al.* 1974). For H_2CO_3, only the diffusion coefficient in tissue has been experimentally determined (Swabb *et al.* 1974). The diffusion coefficients for H^+ ions varied greatly from 0.14×10^{-9} m^2 s^{-1} at 25°C (Al-Baldawi and Abercrombie 1992) in a cytoplasm mixture to 1.18×10^{-9} m^2 s^{-1} in stroma cell layers (Fatt *et al.* 1998). For OH^- ions, the diffusion coefficient was estimated to be 1.1×10^{-9} m^2 s^{-1} for water (Ruff and Friedrich 1972) and 1.56×10^{-9} m^2 s^{-1} in 2 mM salt solution (Easteal and Lawrence 1986). The reported diffusion coefficient for HCO_3^- ions varied significantly from 0.022×10^{-9} m^2 s^{-1}

in an epithelium cell layer (Fatt *et al.* 1998) to $16x10^{-9}$ m^2 s^{-1} in a 2 mM myoglobin solution (Uchida and Doi 1992). For CO_3^{-2} ions, the diffusion coefficient did not vary significantly between water (Kigoshi and Hashitani 1963) and tissue (Swabb *et al.* 1974), where it was estimated to be 0.974 and $0.824x10^{-9}$ m^2 s^{-1}, respectively. Finally, for lactate ions, the experimentally determined diffusion coefficients increased from $0.56x10^{-9}$ m^2 s^{-1} in water (Hazel and Sidell 1987) to $1.6x10^{-9}$ m^2 s^{-1} in a 2% collagen solution (Chresand *et al.* 1988a).

In situations where experimental data have not been reported in the literature, empirical correlations can be used to estimate diffusion coefficients in solvents and in tissues. The diffusivity of small solutes in a solvent may be estimated from the empirical Wilke-Chang equation:

$$D_i = 7.4x10^{-8}\frac{T(\chi MW_i)^{0.5}}{V_m^{0.6}\mu} \qquad \textbf{(5.16)}$$

where D_i is the infinite dilution diffusion coefficient of solute i (cm^2 s^{-1}), T is the temperature (K), χ is the interaction parameter (for water, it is 2.26), MW_i is the molecular weight of solute i, V_m is the molecular volume of the solute at its boiling point (cm^3 g^{-1} mol^{-1}), and μ is the solvent viscosity (cP).

Table 5.2 Summary of experimentally determined diffusion coefficient for CO_2, H_2CO_3, H^+, OH^-, HCO_3^-, CO_3^{-2}, and lactate ion.

Species	Diffus. Coeff. (10^{-9} m^2 s^{-1})	Material Solute Diffusing Through	Reference
CO_2	2.18	Water (30°C)	(Kigoshi and Hashitani 1963)
	2.4	Water (37°C)	(Gros and Moll 1974)
	1.104	Any Tissue	(Swabb *et al.* 1974)
H_2CO_3	0.803	Any Tissue	(Swabb *et al.* 1974)
H^+	9.33	Water (25°C)	(Vanysek 1999)
	1.14	Agar (25°C)	(Al-Baldawi and Abercrombie 1992)
	1.18	Stroma	(Fatt *et al.* 1998)
	0.19	Epithelium	" "
OH^-	1.1	Water (25°C)	(Ruff and Friedrich 1972)
	1.56	Salt solution (25°C)	(Easteal and Lawrence 1986)
HCO_3^-	1.28	Water (30°C)	(Kigoshi and Hashitani 1963)
	2.02	Saline (37°C)	(Livingston *et al.* 1995)
	0.15	Stroma	(Fatt *et al.* 1998)
	0.022	Epithelium	" "
CO_3^{-2}	0.974	Water (30°C)	(Kigoshi and Hashitani 1963)
	0.824	Any Tissue	(Swabb *et al.* 1974)
$CH_3CHOHCO_2^-$	0.56	Water (25°C)	(Hazel and Sidell 1987)
	1.4	1% Agar (37°C)	(Chresand *et al.* 1988a)

An empirical molecular weight correlation for the diffusion of species *i* through tissue slices is

$$D_i = D_{i,w}\left(\frac{32}{MW_i}\right)^{0.75} \qquad (5.17)$$

where $D_{i,w}$ is the diffusion coefficient of *i* in water, and 32 is the molecular weight of water. Casciari (1989) used this correlation to compute the diffusivities of hydrogen and

bicarbonate ions, as well as carbon dioxide and oxygen through multicellular tumour spheroids.

For the diffusion coefficient of lactate ion in tissue, Casciari (1989) used the following correlation (where 180 is the molecular weight of glucose):

$$D_i = D_{i,w}\left(\frac{180}{MW_i}\right)^{0.75} \qquad \textbf{(5.18)}$$

Swabb *et al.* (1974) has reported a general correlation for tissue diffusion coefficients ($cm^2\ s^{-1}$) as a function of molecular weight:

$$D_i = 1.778\times10^{-4}(MW_i)^{-0.75} \qquad 32 < MW_i < 69{,}000 \qquad \textbf{(5.19)}$$

Once the diffusion coefficients have been determined, they can then be corrected to 37°C using a relationship based on the Stokes-Einstein equation (Cussler 1984):

$$D_{i,37^\circ C} = \frac{310}{T}\left(\frac{\mu_T\ D_{i,T}}{\mu_{310}}\right) \qquad \textbf{(5.20)}$$

where μ_T is the viscosity of the solvent and $D_{i,T}$ is the diffusion coefficient of species i at temperature T (K).

There are often significant differences between the diffusion coefficients measured in various solvents, such as in the case of HCO_3^- ions in water and saline (Table 5.2). In order to reduce discrepancies and simplify the model, only diffusion coefficients in water at 37°C, as listed in Table 5.3, are used as the ICS coefficients for the simulation model. Note that the experimental diffusion coefficients determined at lower temperatures have been adjusted to 37°C by applying the Stokes-Einstein equation.

The diffusivities of the various species in the HFBR membrane were estimated using the following equation from Labecki *et al.* (1998)

$$D_{i,MEM} = D_{i,ICS} \cdot \varepsilon \qquad \textbf{(5.21)}$$

where ε is the membrane porosity, assumed to be 0.8 for the regenerated cellulose hollow fibres of the Gambro cartridge.

Table 5.3 Diffusion coefficients used in the ICS for the species mass transfer model

Species	Diffusion Coeff. (10^{-9} m^2s^{-1})	References	Diffusion Coeff. At 37 °C (10^{-9} m^2 s^{-1})
CO_2	2.4 (37 °C)	(Gros and Moll 1974)	2.4
H_2CO_3	4.23 (37 °C)	From Wilke-Chang Equation	4.23
H^+	9.311 (25 °C)	(Vanysek 1999)	12.5
OH^-	1.1 (25 °C)	(Ruff and Friedrich 1972)	1.48
HCO_3^-	1.28 (30 °C)	(Kigoshi and Hashitani 1963)	1.52
CO_3^{-2}	0.974 (30 °C)	(Kigoshi and Hashitani 1963)	1.15
Lactate ion	0.56 (25 °C)	(Hazel and Sidell 1987)	0.75

As can be seen from Table 5.2, the diffusion coefficients for both charged and non-charged species would be expected to be different in the presence of cells. For example, the diffusion coefficient of CO_2 in tissue is approximately half that in water, whereas the diffusion coefficient of H^+ ions in tissue is approximately one-tenth of its value in water. However, for HCO_3^- and CO_3^{-2} ions, the diffusion coefficients in tissue are approximately half and 80%, respectively, of their values in water. An arbitrary factor of 0.5 was therefore applied to all of the ICS diffusion coefficients to derive the corresponding ECS values.

5.4. Numerical Methods

5.4.1 Method of Solving PDEs

At steady state, the differential material balance for each species yields a set of parabolic partial differential equations (Equation 5.2) in two dimensions, in this case, the radial and axial directions. The partial differential equations that govern the concentration distributions of the seven species involved, i.e., CO_2, H_2CO_3, H^+, OH^-, HCO_3^-, CO_3^{-2}, and $CH_3CHOHCO_2^-$, were solved simultaneously using the implicit finite difference method (Forsythe and Wasow 1960). This method was selected over the Crank-Nicolson method, the most commonly-used method for solving parabolic PDEs, because the latter technique yielded unstable results, especially in the membrane and ECS where v_z=0. Using a control volume approach, the Krogh cylinder was transformed into a r x z grid, where the radial steps (i.e., the finite increments in the radial direction) are staggered (Press *et al.* 1986), starting at $r=\Delta r/2$ and with increasing increments of Δr to $r = R_K - \Delta r/2$. A staggered radial grid allows for more convenient specification of the derivative boundary conditions at r=0 and $r=R_K$, as well as more convenient handling of the discrete changes in diffusion coefficients at $r=R_L$ and $r=R_M$. The axial steps, on the other hand, start at z=0 with increasing increments of Δz to $z=L$. The simultaneous set of algebraic equations required to describe the behaviours of all the diffusing species at any given axial position was solved using a block tridiagonal matrix method (Press *et al.* 1986) for CO_2 and H_2CO_3 and the Thomas algorithm (Press *et al.* 1986) for the other five

species. Once the mass balance equations had been solved for a new axial location, the concentrations of the equilibrated species, H_2CO_3, HCO_3^-, CO_3^{-2}, H^+ and OH^-, were updated by using Newton's method to solve the set of nonlinear algebraic equations, Equations 5.8-5.12. In this manner, the concentrations of each species were determined for the next axial position, and onward until $z=L$.

5.4.2 Discretization of PDEs

The derivation of the discretized finite difference equations is shown in Appendix A using CO_2 as an example. The numerical methods described above were programmed using the MatLab 6.1 (The MathWorks Inc., Natick, MA) computing language and the code is shown in Appendix B.

5.4.3 Program Organization

The general flowsheet describing how the program was organized is shown in Figure 5.2. The initial estimates for the ICS species concentrations (Table 5.4) were used as inputs to solve Equations 5.8-5.12 for the equilibrium concentrations at $z=0$ for $0 \leq r \leq R_L$. To arrive at the true equilibrium, in addition to these five equations, one more relationship, describing the CO_2/H_2CO_3 equilibrium, is required. The extra equation is:

$$K_H \cdot [CO_2] - [H_2CO_3] = 0 \qquad \textbf{(5.22)}$$

where $K_H = k_H/k_D = 0.057/50.2 = 1.14 \times 10^{-3}$ (Soli and Byrne 2002) at 32.5°C. Note that Equation 5.22 above is used only for determining the ICS inlet equilibrium concentrations of CO_2, H_2CO_3, HCO_3^-, CO_3^{-2}, H^+, and OH^-. It is assumed that the

medium entering the HFBR at the ICS inlet has a negligible lactate ion concentration (see Table 5.4).

The concentrations of CO_2 and H_2CO_3 at z=0 for $R_L \leq r \leq R_K$ were then obtained by solving Equation 5.2 for these two species using the block tridiagonal matrix (BTDM) method. Next, the Thomas algorithm was used to individually determine, again by solving Equation 5.2, the concentrations of each of the remaining species (i.e., H^+, OH^-, HCO_3^-, CO_3^{-2}, and $CH_3CHOHCOO^-$) at z=0 for $R_L \leq r \leq R_K$. This becomes possible

Table 5.4 Initially estimated and equilibrium ICS concentrations at z=0

Species	**Estimated Concentration (mol m^{-3})**	**Equilibrium Concentration (mol m^{-3})**
CO_2	1.587	1.648
H_2CO_3	0.0045	0.0019
H^+	7.709×10^{-5}	4.373×10^{-5}
OH^-	1.297×10^{-4}	2.287×10^{-4}
HCO_3^-	44.05	43.94
CO_3^{-2}	0.00238	0.0565
Na^+	160.7	160.7
Cl^-	116.7	116.7
Lactate ion	0	0
pH	7.11	7.36

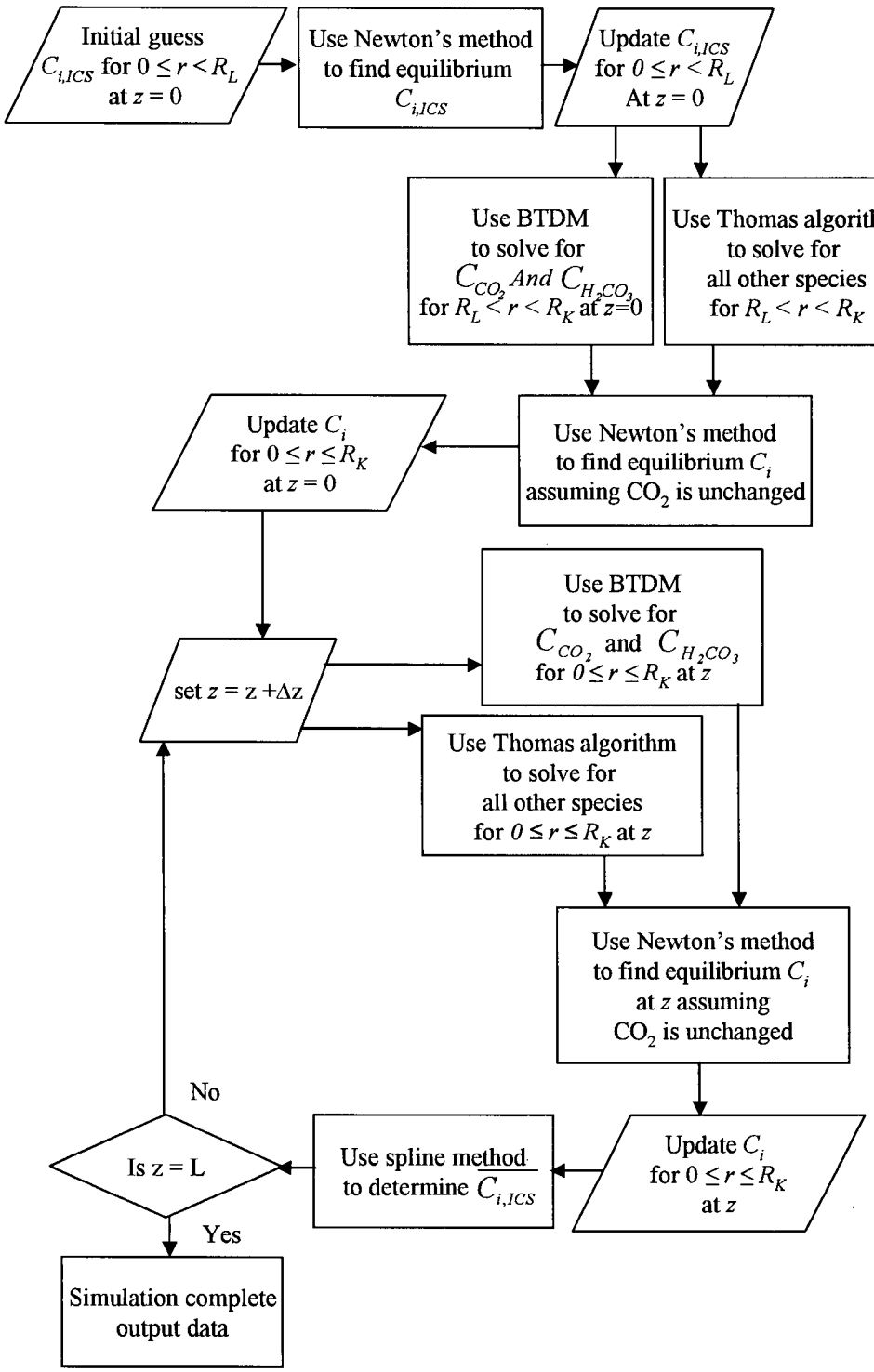

Figure 5.2 Block diagram showing the computational procedure

because the concentrations of these latter species are not linked with any of the others in the mass balance equations. Using these calculated species concentrations based on the diffusive transport, the equilibrium concentrations at each radial position were obtained using Newton's method to solve Equations 5.8-5.12 (i.e., with the CO_2 concentration held unchanged).

Once all species concentrations at z=0 in the ICS, membrane, and the ECS had been determined in this manner, the next step was to obtain the solution at $z = \Delta z$. First, the concentrations of CO_2 and H_2CO_3 at $z = \Delta z$ for $0 \leq r \leq R_K$ were determined using the BTDM method to simultaneously solve Equation 5.2 for these two species. Again, the Thomas algorithm was used to obtain the concentrations of each of the remaining species (i.e., H^+, OH^-, HCO_3^-, CO_3^{-2} and $CH_3CHOHCOO^-$) at $z = \Delta z$ for $0 \leq r \leq R_K$. And finally, by means of Newton's method, the equilibrium concentrations were calculated using Equations 5.8-5.12 with the CO_2 concentration being held unchanged at the values determined from the mass transfer equations.

This procedure was repeated for each axial step Δz until the entire axial distance L was covered. At z=L, the final mixing cup concentration of each species leaving the HFBR at the ICS exit was calculated from

$$\overline{C_{i,ICS}} = \frac{\int_0^{R_L} v_z(r) \cdot C_{i,ICS}(r) \cdot 2\pi r \, dr}{\pi R_L^{\,2} v_{z,avg}} \qquad \textbf{(5.23)}$$

The integral in Equation 5.23 was evaulated using spline quadrature.

5.4.4 Algorithm Testing

Before discretizing the equations for the current model, the simpler case of O_2 transport, where there is no chemical equilibrium involved, was tested to check the finite difference solution procedures. In the O_2 model, the $r_{i,ICS}$ and $r_{i,MEM}$ terms in Equation 5.2 were neglected since there is no generation/consumption of O_2 in the ICS and membrane. For the ECS, $r_{i,ECS}$ is equal to minus the specific oxygen uptake rate times the cell concentration. The mass transport equations were discretized in a manner similar to the method described in Appendix A. The Thomas algorithm was used to solve the set of simultaneous finite difference equations corresponding to each axial position. The O_2 model results using a grid size of 161x2100 matched within 0.001% the results from the analytical solution of Equation 5.2 (Piret and Cooney 1991), indicating that this discretization method is appropriate for the current pH distribution model.

The numerical accuracy of the current model were partially verified by performing an overall carbon mass balance. The ICS inlet and outlet mixing cup concentrations of all species involved in the CO_2 equilibrium kinetics that contained carbon, i.e., CO_2, H_2CO_3, HCO_3^-, and CO_3^{-2}, were calculated. A simple mass balance was performed, including the CO_2 produced by cells in the ECS, and it was found that more than 99.9% of carbon dioxide evolved could be accounted for in the changes in the concentrations of the carbon-containing species between the ICS inlet and outlet. A similar balance on lactate ions yielded an error of less than 0.001%. These mass balance tests suggested that the species concentration errors in this model simulation are relatively small.

5.4.5 Grid Size Optimization

An appropriate size radial-axial grid needs to be selected for the mathematical simulation in order to ensure efficiency and to minimize error. The Krogh cylinder model has a very large length to diameter ratio, with a Krogh radius of 0.000161 m and a length of 0.21 m. When the radial and axial grid sizes were independently varied, the error was calculated as shown in the following equation:

$$error = \frac{\left|pH_{old} - pH_{new}\right|}{pH_{old}} \tag{5.24}$$

where the pH_{old} and pH_{new} are the pH values calculated from the H^+ concentration at the same location for the old and new grid sizes, respectively.

Initially, the number of radial grid interval was selected to be 161 in order to ensure that the discretization control volume boundaries coincided exactly with r=0, r=R_L, r=R_M, and r=R_K. When the radial grid size was doubled from 161 to 322, the error in pH had a maximum value of $4\text{x}10^{-4}$ and an average value of $1.46\text{x}10^{-4}$ at z=L. Therefore, a radial grid size of 161 was chosen to ensure efficient computing. A summary of the maximum and average errors at z=L, calculated when the axial grid size was progressively increased from 21 to 42000 intervals, is shown in Table 5.5. With the axial grid size set at 42000, the maximum pH error was 0.0016 and the average error was $7.3\text{x}10^{-4}$. The time and computing resources needed to complete the simulation at grid sizes larger than 161x42000 become exceedingly demanding. Therefore, a grid size of 161x42000 was chosen to carry out all of the simulations discussed in the next two sections.

Table 5.5 Maximum error calculated when increasing the axial grid size from 21 to 42000, with radial grid size set at 161.

Axial Grid Size	Maximum Error	Average Error
21 → 42	0.0359	0.0306
42 → 210	0.0641	0.0517
210 → 420	0.0220	0.0132
420 → 2100	0.0267	0.0147
2100 → 4200	0.0054	0.0028
4200 → 21000	0.0068	0.0033
21000 → 42000	0.0016	0.00073

5.5. Concentration and pH Profiles

Once the values of the initial concentrations entering the HFBR have been specified, the mathematical model can then be used to determine the concentration distribution inside the HFBR for all transferring species and for any set of operational conditions.

In Figure 5.3, the radial concentration profiles for the species CO_2, H_2CO_3, H^+, OH^-, HCO_3^-, and CO_3^{-2} are shown at three axial positions, $z=1/3L$, $z=2/3L$ and $z=L$. The dotted vertical lines define the three regions in the model: the ICS, the membrane, and the ECS. The ICS appears to be the largest region but, in fact, because of the cylindrical geometry, the ECS volume is about 20% greater than that of the ICS.

The axial CO_2 concentration increased as the ICS fluid moved downstream, which is in agreement with the fact that the carbon dioxide produced by the cells accumulates in the ICS and ECS. The production of H^+ via lactic acid in the ECS would also aid in the equilibrium conversion of H_2CO_3 to CO_2. Conversely, the axial HCO_3^- concentration

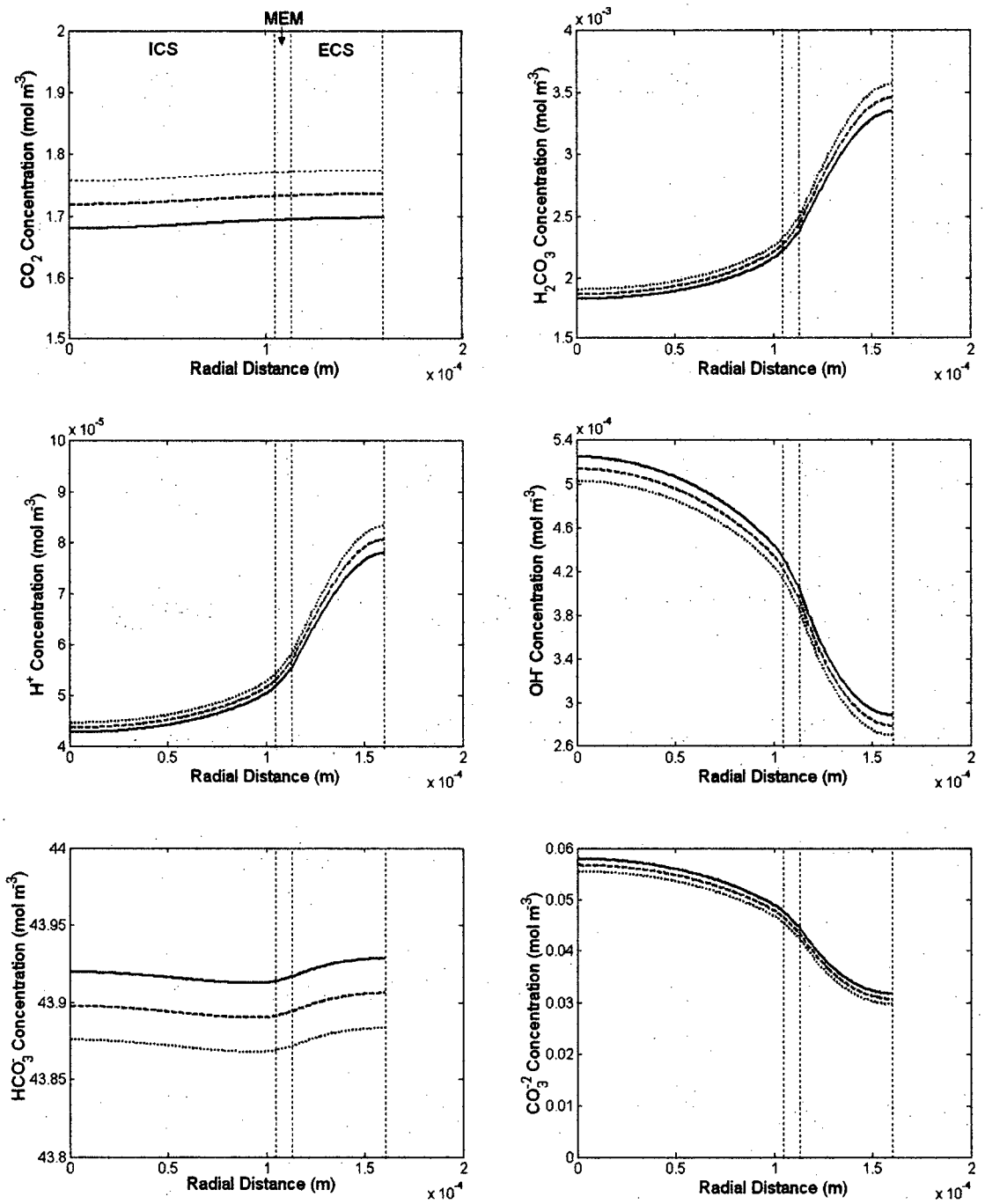

Figure 5.3 Species radial concentration distributions at three different axial positions (z=1/3L solid line, z=2/3L dashed line, and z=L dotted line). ICS flow rate = 300 mL min^{-1}. Diffusion coefficients for all species in ECS were taken to be 0.5 times their ICS values. *sCER* and *sLPR* are 8.33x10^{-18} and 1.35x10^{-17} mol cell^{-1} s^{-1}, respectively. Grid size is 161x42000. The equilibrium ICS inlet concentrations are shown in Table 5.4.

decreased slightly as a result of the chemical equilibrium with H_2CO_3 and H^+ ions. It should be noted that the relatively high concentrations of HCO_3^-, ~44 mol m^{-3}, were due to the sodium bicarbonate that was added to the cell culture medium to act as a pH buffer. The radial H^+ concentration is the highest at the Krogh cylinder radius as a result of lactic acid dissociation and the first acid dissociation of H_2CO_3. Similarly, the radial lactate concentration is also the highest at the Krogh cylinder radius (Figure 5.4) as a result of lactic acid production by the cells and the dissociation of lactic acid to H^+ and lactate. The axial increase in the lactate concentration corresponds to the accumulation of lactate in the HFBR. (Note that the ICS inlet lactate ion concentration was selected to be zero for these simulations.)

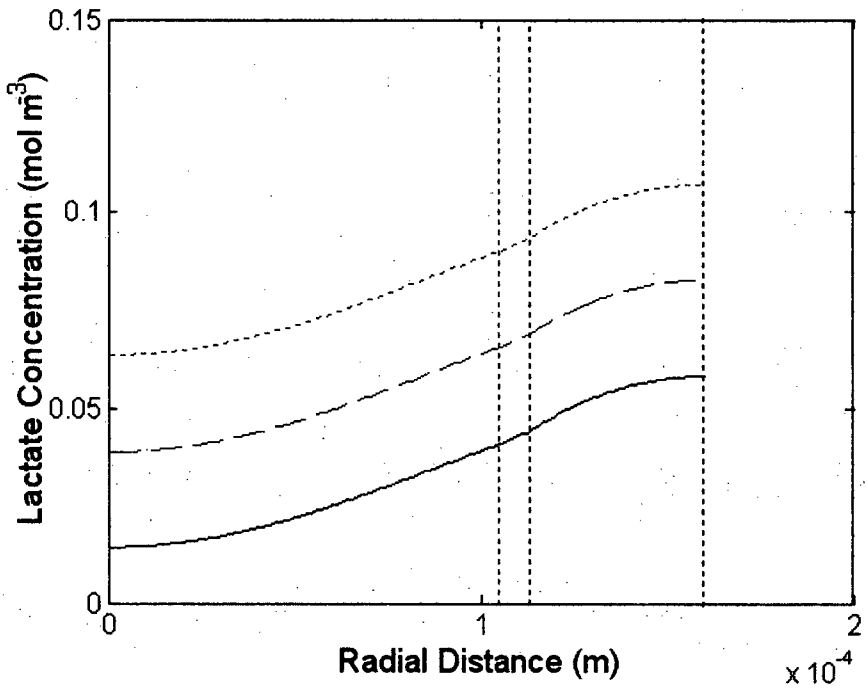

Figure 5.4 Radial lactate concentration distribution at three different axial positions (z=1/3L solid line, z=2/3L dashed line, and z=L dotted line). ICS flow rate = 300 mL min^{-1}. Diffusion coefficients for all species in ECS were taken to be 0.5 times their ICS values. sCER and sLPR are $8.33x10^{-18}$ and $1.35x10^{-17}$ mol $cell^{-1}$ s^{-1}, respectively. Grid size is 161x42000. The equilibrium ICS inlet concentrations and pH are shown in Table 5.4.

Using the calculated H^+ concentration profiles, one can determine the pH distribution in the HFBR cartridge, as shown in Figure 5.5. The mixing-cup ICS pH change from the inlet to the outlet was calculated to be 0.03 pH units. The overall radial pH decrease was about 0.28 between $r=0$ and $r=R_K$ at all axial positions beyond $z=0$. These results are similar to those reported by Piret *et al.* (1991), where the measured ICS inlet-outlet pH difference was 0.05 and ICS-ECS pH difference was 0.5. In the ECS region alone, the decline in the pH was ~0.15 between $r=R_M$ and $r=R_K$. Nonetheless, for the particular circumstances selected here, these results suggested that cells trapped in the ECS will not experience harmful pH conditions (i.e., the pH everywhere remained in the range of 7.0-7.4).

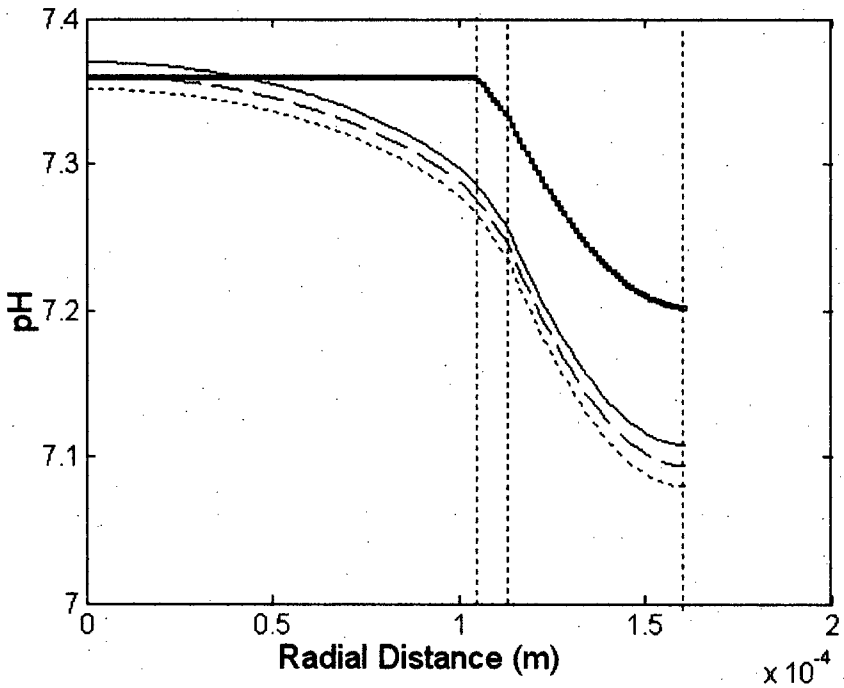

Figure 5.5 Radial pH distribution at four different axial positions ($z=0$ bold solid line $z=1/3L$ solid line, $z=2/3L$ dashed line, and $z=L$ dotted line). ICS flow rate = 300 mL min^{-1}. Diffusion coefficients for all species in ECS were taken to be 0.5 times their ICS values. sCER and sLPR are $8.33x10^{-18}$ and $1.35x10^{-17}$ mol $cell^{-1}$ s^{-1}, respectively. Grid size is 161x42000. The equilibrium ICS inlet concentrations and pH are shown in Table 5.4.

The simulation shown in Figure 5.5 will be used as a basis for comparison with the results obtained as several of the base case parameters are now individually varied.

5.6. Effect of Different System Conditions on pH Distribution

The mathematical model is useful for interpreting the effect on pH of a number of system parameters including the ICS flow rates, the values of *sCER* and *sLPR*, the ECS diffusion coefficients, the size of the Krogh cylinder radius, and the ICS inlet pH.

When the ICS flow rate is increased from 150 to 600 mL min^{-1}, as shown in Figure 5.6, the axial pH gradient is reduced, i.e., there is a reduction in the spacing between the curves. In addition, the effect of flow rate on the pH difference between the ICS (r=0) and ECS (r=R_K) at z=L appears to decrease slightly, from approximately 0.29 at 150 mL min^{-1} to 0.26 at 600 mL min^{-1}. The ICS flow rate also influences the pH in the ECS at r=R_K and z=L, which is 7.03 at 150 mL min^{-1} and 7.11 at 600 mL min^{-1}. The increase in axial convection at higher flow rates is expected to reduce the axial concentration gradients and thereby increase the ECS pH.

The values of *sCER* and *sLPR* found in the literature are subject to a wide degree of variability due to the use of different cell lines, different operational modes (batch vs. continuous), and inhomogeneous environmental factors (oxygen limitation, protein polarization in HFBR, etc.). When *sCER* and *sLPR* were both increased four-fold, from 4.165×10^{-18} and 0.675×10^{-17} (i.e., half the base case values) to 1.667×10^{-17} and 2.7×10^{-17} mol $cell^{-1}$ s^{-1} (i.e., twice the base case values), respectively, the maximum pH difference

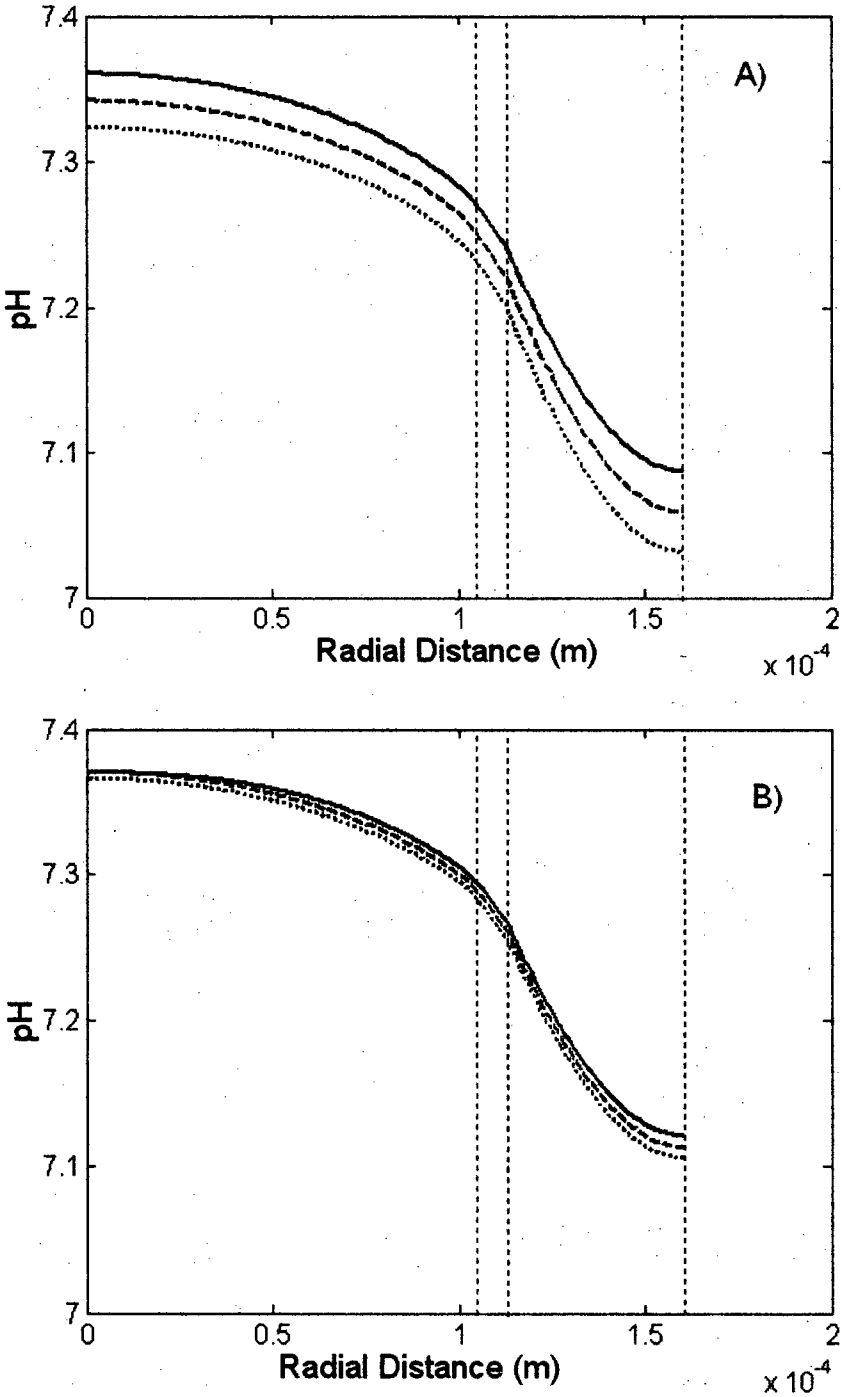

Figure 5.6 Radial pH distribution at three different axial positions (z=1/3L solid line, z=2/3L dashed line, and z=L dotted line). ICS flow rates are A) 150 and B) 600 mL min^{-1}, respectively. Diffusion coefficients for all species in ECS were taken to be 0.5 times their ICS values. *sCER* and *sLPR* are 8.33×10^{-18} and 1.35×10^{-17} mol $cell^{-1}$ s^{-1}, respectively. Grid size is 161x42000. The equilibrium ICS inlet concentrations and pH are shown in Table 5.4.

between the ICS and ECS increased significantly at $z=L$, from approximately 0.1 to 1.8, as shown in Figure 5.7. At pH values below 7, most cells begin to experience significant stress and many would not survive under the pH conditions near $r=R_K$ for the largest combination of specific rates. The results shown in Figure 5.7 suggest that the *sCER* and *sLPR* values play a more dominant role, compared to the ICS flow rate, in affecting the ECS pH. Note that, since the source terms for CO_2 and H^+ are obtained as the product of a specific production rate and the cell concentration, the same effects would have been obtained by halving or doubling the cell concentrations (i.e. $1.5x10^{14}$ or $6x10^{14}$ cells m^{-3}) with *sCER* and *sLPR* held constant (assuming the ECS diffusion coefficients are

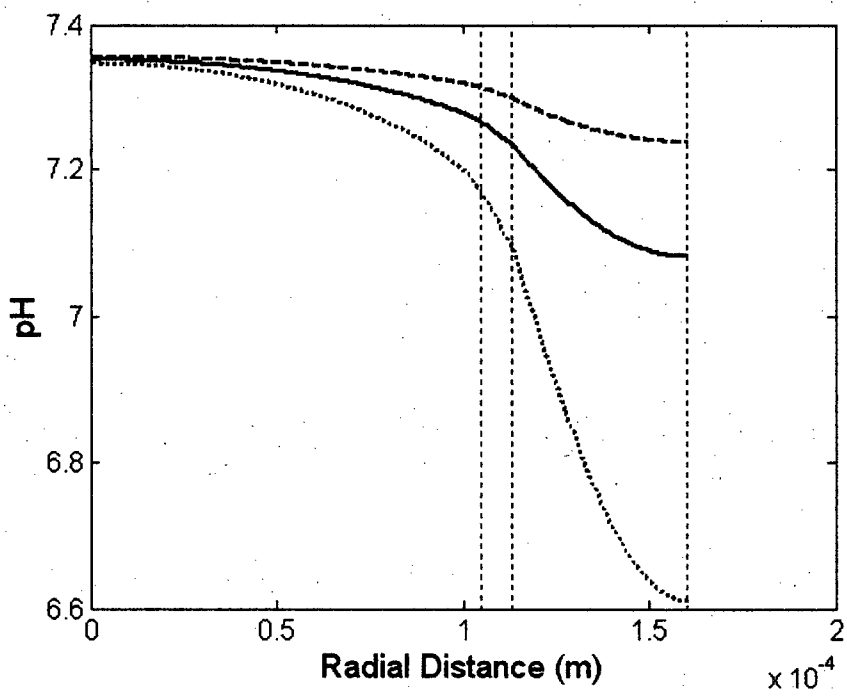

Figure 5.7 Radial pH distribution at axial position, $z=L$. ICS flow rate is 300 mL min^{-1}. Diffusion coefficients for all species in ECS were taken to be 0.5 times their ICS values. *sCER* and *sLPR* are $4.165x10^{-18}$ and $0.675x10^{-17}$ (dashed line), $1.667x10^{-17}$ and $2.7x10^{-17}$ (dotted line), and the based case, $8.33x10^{-18}$ and $1.35x10^{-17}$ mol $cell^{-1}$ s^{-1} (solid line), respectively. Grid size is 161x42000. The equilibrium ICS inlet concentrations and pH are shown in Table 5.4.

unaffected by changes in X).

The results shown in Figure 5.7, and in subsequent figures where pH values drop below approximately 6.8, should be interpreted with care. Hybridoma growth rate and metabolism are strongly influenced by the pH environment (Miller *et al.* 1988). For instance, at pH values below 6.8, it was found that glucose consumption (and, therefore, lactic acid production) decreased. The decrease in the lactic acid production rate as a function of low pH was not incorporated in this model.

The individual effects of *sCER* and *sLPR* are compared in Figure 5.8. Interestingly, when *sLPR* is set to zero and *sCER* is 8.33×10^{-18} mol cell^{-1} s^{-1}, no observable radial pH gradients were predicted. Overall, the *sCER* played a less important role in affecting the pH because, while CO_2 affects the pH only indirectly through the equilibrium reactions, lactic acid contributes H^+ ions directly. Also, CO_2 is produced at approximately half the rate of lactic acid. The axial pH change was also relatively small, in the range of 0.01. When the *sCER* was zero and *sLPR* was 1.35×10^{-17} mol cell^{-1} s^{-1}, the pH profiles were similar to the ones shown in Figure 5.5. Apparently, lactic acid production contributes much more to the radial pH gradient than does the evolution of carbon dioxide at least at the specific generation rates selected here.

From the diffusion coefficients listed in Table 5.2, one can see that the values for the charged species in tissues are, in general, significantly different from those in water, by as much as an order of magnitude in the case of H^+ and HCO_3^-. A simulation was performed where the ECS diffusion coefficients for non-charged species remained at 0.5

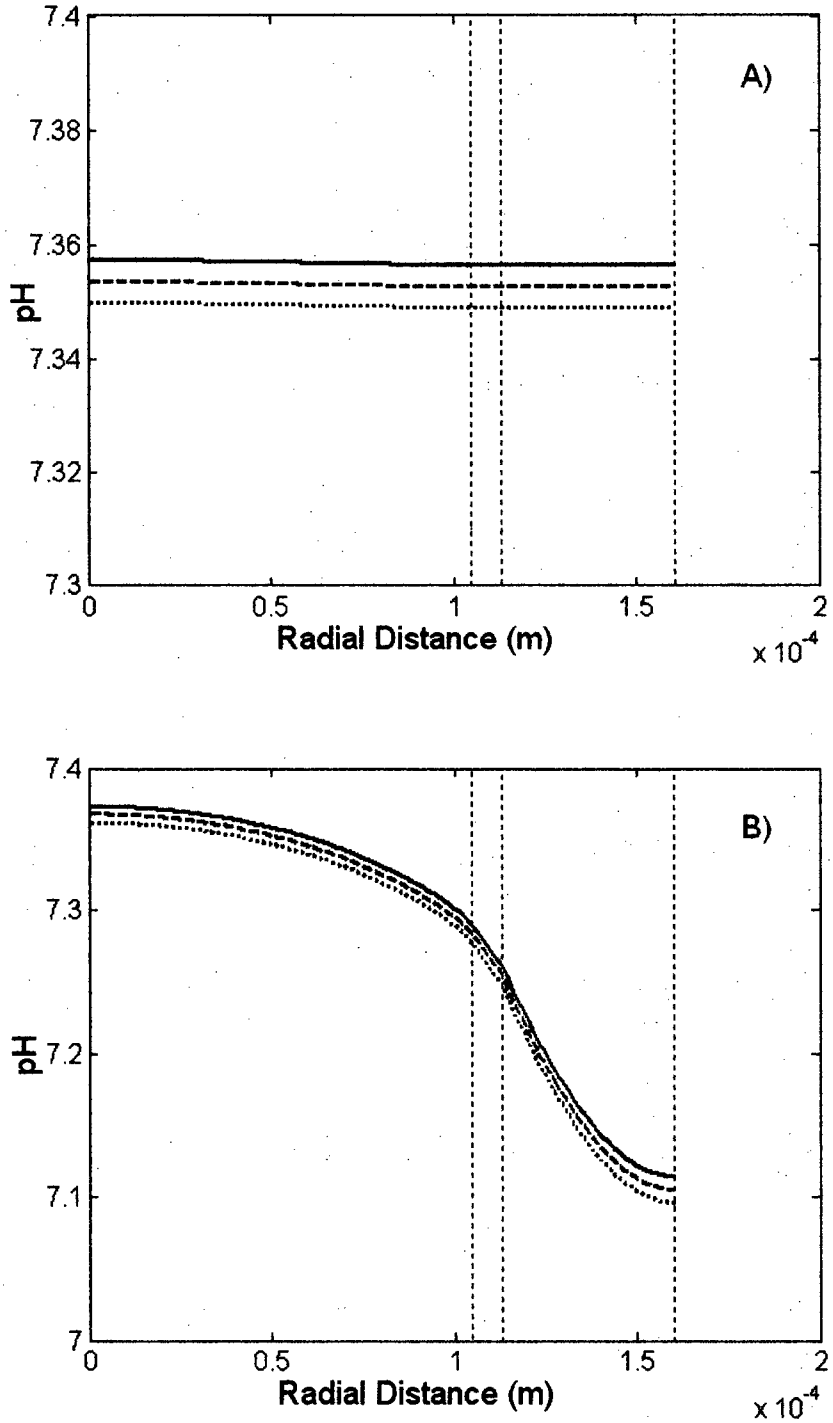

Figure 5.8 Radial pH distribution at three different axial positions (z=1/3L solid line, z=2/3L dashed line, and z=L dotted line). ICS flow rate is 300 mL min^{-1}. Diffusion coefficients for all species in ECS were taken to be 0.5 times their ICS values. *sCER* and *sLPR* are A) 8.33x10^{-18} and 0, and B) 0 and 1.35x10^{-17} mol cell^{-1} s^{-1}, respectively. Grid size is 161x42000. The equilibrium ICS inlet concentrations and pH are shown in Table 5.4.

times, whereas those for the charged species were decreased to 0.1 times, their ICS values. The difference in the radial ECS pH between $r=R_L$ and $r=R_K$ increased by more than 7-fold compared to the base case (Figure 5.9), probably primarily due to the decreased ability of H^+ ions to transfer from the ECS to the ICS. This suggests that the charged species diffusion coefficients in the cell-packed ECS also play a very important role in controlling the ECS radial pH gradients.

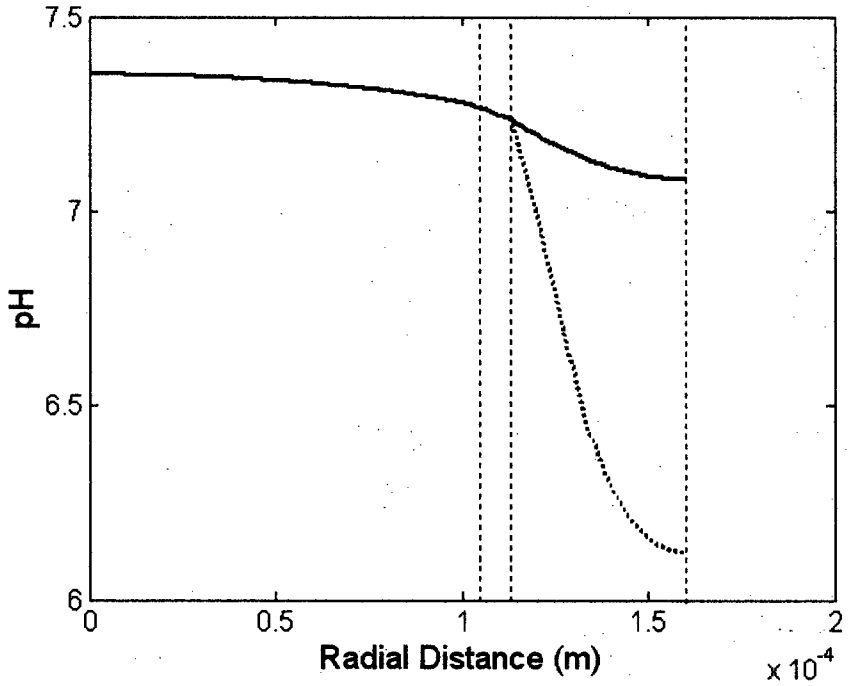

Figure 5.9 Radial pH distribution at axial position, $z=L$. ICS flow rate is 300 mL min^{-1}. Diffusion coefficients for all non-charged species in ECS were taken to be 0.5 times and for charged species 0.1 times their ICS values (dotted line). In the base case, all species ECS diffusion coefficients were 0.5 times their ICS values (solid line). *sCER* and *sLPR* are 8.33×10^{-18} and 1.35×10^{-17} mol $cell^{-1}$ s^{-1}, respectively. Grid size is 161x42000. The equilibrium ICS inlet concentrations and pH are shown in Table 5.4.

One parameter that is very important in the design of HFBRs is the distance between fibres, manifested in this model by the thickness (i.e., the difference between R_K and R_M) of the annular ECS space occupied by the cells. When the packed cell ECS thickness was doubled, at the downstream end and the outer edge of the ECS, i.e., where $r=R_K$ and $z=L$, the pH fell from 7.1 to 6.1 (Figure 5.10). This significant steepening of the radial pH gradients in the ECS is due to a combination of two factors: (1) more than twice as much CO_2 and lactic acid are produced by the larger cell mass and (2) the diffusing species have twice as far to travel. This result suggests that pH considerations (due to the metabolic activity of cells) could play an important role along with oxygen delivery in determining the optimal fibre spacing in a HFBR. In the present case (Figure 5.10)

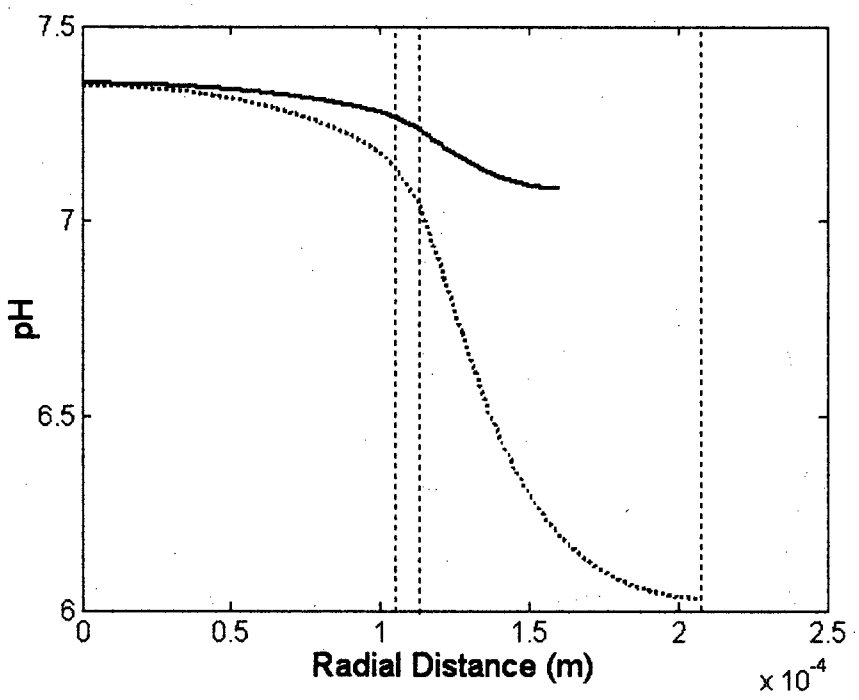

Figure 5.10 Radial pH distribution at axial position $z=L$. ICS flow rate is 300 mL min^{-1}. Diffusion coefficients for all species in ECS were taken to be 0.5 times ICS value. *sCER* and *sLPR* are $8.33x10^{-18}$ and $1.35x10^{-17}$ mol $cell^{-1}$ s^{-1}, respectively. Grid size is 209x42000, as the ECS thickness is doubled (dotted line) and 161x42000 for the base case (solid line). The equilibrium ICS inlet concentrations and pH are shown in Table 5.4.

where the ECS thickness was doubled, pH considerations would probably prevent viable cells from filling the ECS space; rather they would likely grow only in a layer near the membrane surface. It should be noted that the Krogh cylinder approximation assumes evenly-spaced fibres. In an actual HFBR, the local fibre spacing can vary significantly such that even lower pH values could be encountered than predicted by the Krogh cylinder model.

Another parameter that can be adjusted in the operation of HFBRs is the ICS inlet pH. For the base case (Figure 5.5), the pH at the ICS inlet is approximately 7.4. When the ICS inlet pH is decreased to 7.1 and the concentrations of all species at the ICS inlet are

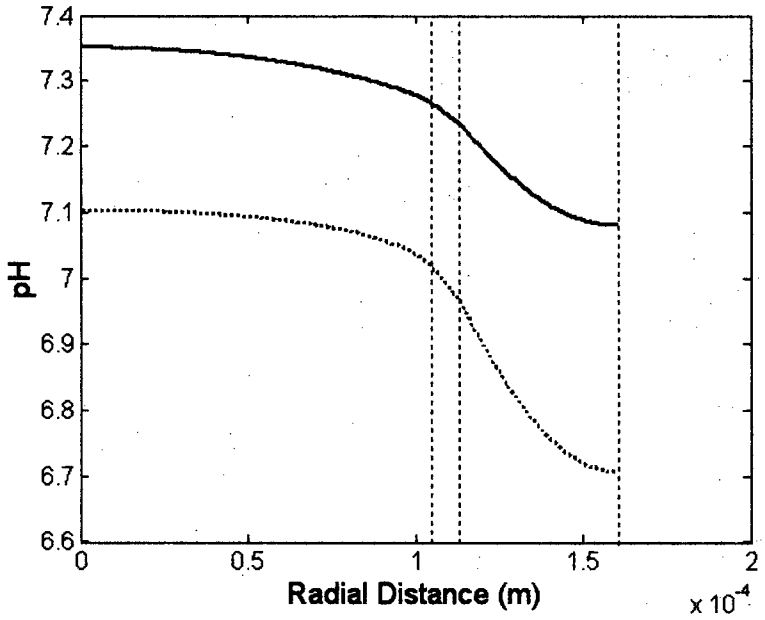

Figure 5.11 Radial pH distribution at axial position $z=L$. ICS flow rate is 300 mL min^{-1}. Diffusion coefficients for all species in ECS were taken to be 0.5 times ICS value. *sCER* and *sLPR* are $8.33x10^{-18}$ and $1.35x10^{-17}$ mol $cell^{-1}$ s^{-1}, respectively. Grid size is 161x42000. ICS inlet pH has been adjusted to 7.13 (dotted line) with all species maintained in equilibrium, compared to the base case value of 7.36 (solid line).

maintained at equilibrium, the ECS pH at $z=L$ and $r=R_K$ approached 6.7 (Figure 5.11). This result suggests that the bulk of cells in the ECS would then experience suboptimal pH conditions.

5.7. Discussion and Conclusions

A model of metabolite mass transport was developed that predicts the concentrations of various species involved in the CO_2-bicarbonate equilibrium within a packed cell HFBR that utilizes a bicarbonate-buffered medium. The current model incorporates CO_2 evolution and lactic acid generation by cells which are packed into the ECS of the HFBR. Both species were assumed to be produced homogeneously and at fixed rates in the ECS. Lactic acid, a major metabolite, was assumed to behave as a source of H^+ ions. Even though ammonia is another metabolite commonly found in cell culture (and one that can also affect system pH), it is typically produced at much lower rates than lactic acid. Therefore, ammonia production was not included in the present model.

One of the major model assumptions is that the ECS is uniformly packed with cells. Regions void of cells, or channels, have been observed in the ECS of an otherwise cell-packed HFBR. The inhomogeneity in the ECS of a packed HFBR has not been accounted for in this model. One could qualitatively account for such inhomogeneities by reducing the ECS cell concentrations to approximate the presence of voids and channels.

Another model assumption is that the ECS diffusion coefficients are related by a general factor to the corresponding ICS values. The values shown in Table 5.2 suggest that diffusion coefficients for cell layers and tissues can be very different from those in water or aqueous solutions. The diffusion coefficients can vary significantly between cell types, e.g., between stroma and epithelium. It is also expected that the diffusion coefficients of charged and non-charged species will be affected differently by the presence of cells bearing surface charges with hydrophobic membranes and having ion channels for facilitated transport. When the general factor for charged species in the ECS was reduced from 0.5 to 0.1 (Figure 5.9), the model predicted a much greater drop in the ECS pH at the Krogh cylinder radius. This result indicates that the pH profile in the HFBR can be greatly affected by the diffusion coefficients through the cell mass. Therefore, to ensure more accurate model predictions, more accurate diffusion coefficients need to be measured and these may depend on the specific cell type used in the bioreactor.

The specific metabolite production rates, *sLPR* and *sCER*, used in this model were assumed to be constant with time and homogenous throughout the cell mass. This could be quite different from reality. Typically, *sLPR* and *sCER* are obtained from batch or continuous stirred tank bioreactors. These rates can be quite different from those in the ECS of a HFBR where the cells grow to much higher concentrations. In addition, there is an observed variability between different cell lines. Furthermore, lactic acid production and carbon dioxide evolution rates are affected by the extracellular pH. The current model did not account for the relationship between the specific rates (sLPR and sCER) and pH, a feature that should be included in a future modification of this model.

The model has demonstrated that increasing both *sLPR* and *sCER* simultaneously can lead to significant radial pH gradients in the ECS (Figure 5.7). The model also predicted that *sLPR* played a much more important role in affecting the radial pH gradients than does *sCER* (Figure 5.8). This result was somewhat unexpected as evolved CO_2 was originally thought to have an effect on pH more similar to that of lactic acid. When *sCER* was increased by a factor of 10 times its original value with *sLPR*=0, the model predicted a greater radial pH gradient than shown in Figure 5.8(A). The pH values at $z=L$ and $r=R_K$ were 7.35 and 7.26 when *sCER* was set to 8.33×10^{-18} and 8.33×10^{-17} mol cell^{-1} s^{-1}, respectively, with *sLPR=0*.

The model has also shown that the spacing between HFBR fibres could play an important role in affecting the radial pH variations. When the cell layer thickness was doubled, the ECS pH at $r=R_K$ changed from ~7.1 to ~6.1 at $z=L$ (Figure 5.10). It is likely that most of the cells in the ECS would not remain viable at the low pH values encountered in most of the ECS when its thickness was doubled. This result suggests that radial pH gradients could play as important a role in the determining the optimum fibre spacing in HFBRs as was previously suggested for oxygen gradients (Piret and Cooney 1991).

Another parameter that could be very important in maintaining and operating a packed cell HFBR is the pH at the ICS inlet. When the inlet ICS pH was reduced from 7.4 to 7.1, the ECS pH at $r=R_K$ and $z=L$ fell from ~7.1 to ~6.7 (Figure 5.11), where the latter value is in a pH range that could be harmful to cells. This result should raise a cautionary warning for operators accustomed to maintaining the HFBR reservoir pH at a stirred tank bioreactor setpoint of 7.0, as this may be too low for the cells in the ECS. This model can

therefore assist operators of HFBRs in determining the optimum inlet ICS condition that would result in a favourable pH environment throughout the ECS.

The mathematical model used a set of previously reported diffusion coefficients along with some generalized assumptions about the specific metabolic production rates, *sLPR* and *sCER*. The change between the ICS inlet and outlet pH, and the difference between the ICS and ECS pH predicted by the model were comparable to corresponding values described in the literature. This suggests that the model might serve as a useful qualitative tool for assessing operating and system parameters in order to reduce harmful pH conditions in the ECS cell mass and optimize the production of biological products in HFBRs. Furthermore, the model may also be applicable in the field of tissue engineering, where cells could be even more sensitive to pH variations.

One major drawback of this work is the lack of experimental data confirming the model. The axial pH decrease and the ICS-ECS pH difference predicted by the model, using the most likely set of transport and reaction parameters, were similar to data reported by Piret *et al.* (1991), but the radial pH profiles under cell-packed conditions were not measured. In principle, the non-trivial task of measuring ECS pH values could be performed by using a micro-electrode or nuclear magnetic resonance (NMR) imaging. However, NMR studies require access to such a facility and are costly. Micro-electrode measurements may be feasible, but many aspects, such as how to measure the position of the electrode relative to the bundle of fibres , still need to be worked out.

Chapter 6

CONCLUSIONS AND FUTURE WORK

Hollow fibre cartridges are widely used and have many applications. The usefulness of mammalian cell HFBRs in producing monoclonal antibody diagnostic and biopharmaceutical products has been the motivation for many experimental and theoretical studies to better understand the conditions inside hollow fibre cartridges and to improve the productivity of the process. The overall goal of this work was to identify factors that affect cell growth in HFBRs and to determine optimal operating conditions by investigating three separate yet interrelated areas: 1) identifying factors that can cause a prolonged start-up, using TFL-P9 hybridoma cells as an example; 2) investigating the impact of packed cell density on product harvest and the effectiveness of culturing cells that form ECM, using CHO cells; and 3) modelling lactic acid and CO_2 transport to allow estimation of pH variations in HFBRs.

A number of factors associated with the delay in HFBR start-up were identified. The rinsing of the HFBR cartridge prior to inoculation and the loss of inoculum to hypoxic manifolds could directly prolong the start-up. Transient downstream polarization of growth factors could also extend the duration of the start-up. As a result of these factors, the growth of the inoculum would be slowed down, leading to a longer start-up compared to a parallel batch culture. The release of growth inhibiting factors from the settled cells, the possible build-up of ammonium and the decrease in L-glutamine concentration, either

individually or in combination, could lead to further delays in start-up. In some cases, combinations of these effects could explain start-up failure.

Koska *et al.* (1997) used a mathematical model to show that the bulk of high molecular weight product proteins cannot be efficiently harvested from HFBRs when ECM fills the ECS space between cells, because of the resulting increase in ECS flow resistance. Using two t-PA producing CHO cell lines, the observed drop in the product harvest concentration when HFBRs became filled with cells supported the model predictions of Koska *et al.*, indicating that product recovery was significantly hindered for cells that produce ECM. This could explain why HFBRs are so rarely used for recombinant protein production with CHO-type cells lines, while they remain widely used for small-scale hybridoma monoclonal antibody production. For one cell line, t-PA inhibition of t-PA production also influenced the results. In addition, t-PA can bind to the cells. Due to this inhibition and binding, the ability of HFBRs to concentrate products in the ECS can become a disadvantage as the ECS eventually becomes filled with both viable and nonviable cells. The confirmation of the Koska *et al.* (1997) model prediction would be clearer if another protein, without the binding properties of t-PA to lysine residues, was used.

A mathematical model of HFBR mass transport was developed to describe the effects of CO_2 and lactic acid production on the ECS cell culture environment, in particular the pH. This mathematical model, using a set of previously reported diffusion coefficients along with some generalized assumptions for *sLPR* and *sCER*, predicted ICS inlet to outlet pH changes as well as ICS to ECS pH differences that were similar to experimentally

measured values. The model was used to investigate the effects on the axial and radial pH gradients of the ICS flow rate, *sCER*, *sLPR*, charged species diffusion coefficients, ECS cell layer thickness, and inlet ICS pH. The variables that had the greatest impact on the pH gradients were *sLPR*, diffusivity values, ECS thickness and inlet ICS pH. This model could prove very useful in helping to specify the operating and system parameters that reduce harmful ECS pH values and thereby optimize the production of biological products in HFBRs.

Reduction of HFBR start-up delay could be validated by minimizing the factors identified in side-by-side HFBR experiments, where the same inoculum is used for two HFBRs. These factors would all be reduced in one cartridge and not minimized in the other. In this way, the cumulative effect of combining factors associated with start-up delay could be clearly demonstrated. In addition, these side-by-side HFBRs could be operated until they reached the stationary phase, where their productivities could be compared.

A sensitivity analysis could be performed on the diffusion coefficients of all charged species. Only the diffusion coefficients of those charged species that are found to have a significant effect on the radial ECS pH gradient need to be further refined, whereas only approximate values could suffice for the other species.

The CO_2/lactic acid model could be improved by including other species of importance, in particular the ammonia produced by the deamination of L-glutamine. In addition, various parameters for the cell line used in the HFBR could be more accurately determined, such as the cell specific generations rates, *sCER* and *sLPR*, as well as the

effective diffusion coefficients in the cell-packed ECS. Furthermore, the cell specific generation rates as functions of extracellular pH could be incorporated in a future model.

The ECS pH values could be measured by using small pH electrodes in a single-fibre HFBR (Gramer and Poeschl 2000), simulating a Krogh cylinder. The radial ECS pH gradients predicted by the model also could be experimentally verified, possibly with the aid of nuclear magnetic resonance imaging.

Alleviating the problems that contribute to delayed start-up and subsequent culture failure should lead to more efficient and rapid production of proteins from HFBRs. Understanding the problems caused by ECM in packed cell HFBRs should restrict future attempts to use these bioreactors for protein production by ECM forming cell lines. With the assistance of the mass transfer model, the negative effects of pH gradients could be minimized. With the increased use of immobilized cell bioreactors for artificial organs and tissue engineering research, these HFBR results should also provide valuable guidance for more effective biomedical engineering applications of mammalian cell culture.

NOMENCLATURE

Latin letters

$C_{i,j}$	local concentration of species i in region j in eq.(5.1)	(mol m^{-3})
C_{O_2}	oxygen concentration	(mol m^{-3})
d_1	tube inside diameter	(m)
d_2	tube outer diameter	(m)
D	diffusion coefficient in the liquid phase	(m^2 s^{-1})
D_{e,O_2}	effective diffusivity of oxygen through packed cells	(m^2 s^{-1})
D_i	infinite dilution diffusion coefficient of solute i in eq. (5.16)	(cm^2 s^{-1})
$D_{i,w}$	diffusion coefficient of i in water, eq. (5.17)	(cm^2 s^{-1})
$D_{i,T}$	diffusion coefficient of species i at temperature T (K), eq. (5.20)	(cm^2 s^{-1})
D_{O_2}	oxygen diffusivity	(cm^2 s^{-1})
f	correction factor for tubing dimensional changes due to elastic deformation of the silicone rubber when it is pressurized	(-)
H	Henry's law constant for the liquid	(atm m^3 mol^{-1})
H_m	Henry's law constant for the membrane	(atm m^3 mol^{-1})
k_D	dehydration constant	(s^{-1})
k_H	hydration constant	(s^{-1})
k_L	liquid film mass transfer coefficient	(m s^{-1})
k_m	membrane mass transfer coefficient	(mol s g^{-1} m^{-1})
K_{a1}	first acid dissociation constant	(mol m^{-3})
K_{a2}	second acid dissociation constant	(mol m^{-3})
K_H	k_D/k_H	(-)
K_W	water dissociation constant	(mol m^{-3})
L	length of the tube / hollow fibre	(m)
MW_i	molecular weight of solute i in eq. (5.16)	(g mol^{-1})
N	number of fibres	(-)
pH_{new}	pH value calculated from the H^+ concentration at the same location for the new grid size	(-)
pH_{old}	pH value calculated from the H^+ concentration at the same location for the old grid size	(-)
Pe^r_L	radial Peclet number	(-)
Pe^z_L	axial Peclet number	(-)
Q	volumetric oxygen uptake by the cells	(mol m^{-3})
r	radial position	(m)
$r_{i,j}$	kinetic term in eq. (5.1)	(mol m^{-3} s^{-1})
Re	Reynolds number	(-)
R_K	Krogh cylinder radius	(m)
R_L	outer radius of the fibre lumen	(m)

R_M	outer membrane radius	(m)
$sCER$	specific carbon dioxide evolution rate	(mol $cell^{-1}$ s^{-1})
$sLPR$	specific lactic acid production rate	(mol $cell^{-1}$ s^{-1})
Sc	Schmidt number	(-)
T	Temperature	(K)
u	average ICS axial fluid velocity	(m s^{-1})
v_r	radial fluid velocity	(m s^{-1})
v_z	axial fluid velocity	(m s^{-1})
$v_{z,avg}$	average fluid velocity in each fibre lumen	(m s^{-1})
v_r^L	average radial ICS velocity	(m s^{-1})
V_m	molecular volume of the solute at its boiling point	(cm^3 g^{-1} mol^{-1})
X	ECS cells concentration	(cell m^{-3})
z	axial position	(m)

Greek Letters

χ	interaction parameter, eq. (5.16)	(-)
ε	membrane porosity	(-)
μ	solvent viscosity, eq. (5.16)	(cP)
μ_T	viscosity of the solvent at temperature T	
θ_m	tubing void fraction	(-)

Subscripts

ECS	extracapillary space
i	species / solute
ICS	intracapillary space
j	region
MEM	membrane
r	radial direction
z	axial direction

Abbreviations

BHK	baby hamster kidney
BTDM	block tridiagonal matrix
CHO	Chinese hamster ovary
DMEM	Dulbecco's Modified Eagle Medium
ECM	extracellular matrix
EC	extracapillary

ECS	extracapillary space
ELISA	enzyme-linked immunosorbent assay
FBS	fetal bovine serum
HEPES	N-2-hydroxyethylpiperazien-N'-2-ethane sulphonic acid
HFBR	hollow-fibre bioreactor
ICS	intracapillary space
IgG_1	immunoglobulin G
PDE	partial differential equations
PP	polypropylene
PTFE	polytetrafluoroethylene
SFM	serum-free media
t-PA	tissue plasminogen activator
WHO	World Health Organization

REFERENCES

Adamson SR, Behie LA, Gaucher GM, Lesser BH. 1987. Metabolism of Hybridoma Cells in Suspension Culture: Evaluation of Three Commercially Available Media. In: Seaver SS, editor. Commercial Production of Monoclonal Antibodies: A Guide for Scale-Up.

Adema E, Sinsky A. 1987. An Analysis of Intra versus Extracapillary Growth in a Hollow Fiber Reactor. Biotechnol. Prog. 3:74-79.

Al-Baldawi N, Abercrombie R. 1992. Cytoplasmic Hydrogen Ion Diffusion Coefficient. Biophysical J 61(6):1470-1479.

Andersen B, Gruenberg M. 1987. Optimization Techniques for the Production of Monoclonal Antibodies Utilizing Hollow-Fiber Technology. In: Seaver S, editor. Commercial Production of Monoclonal Antibodies: A Guide for Scale-Up. New York: Marcel-Dekker. p 175-195.

Arrua L, McCoy B, Smith J. 1990. Gas-Liquid Mass Transfer in Stirred Tanks. A.I.Ch.E. J. 36(11):1768-1772.

Ashkenas J, Muschler J, Bissell M. 1996. The Extracellular Matrix in Epithelial Biology: Shared Molecules and Common Themes in Distant Phyla. Dev. Biol. 180:433-444.

Aunins J, Goldstein J, Croughan M, Wang D. 1986. Engineering Developments in the Homogeneous Culture of Animal Cells: Oxygenation of Reactors and Scale-Up. Biotechnol. Bioeng. Symp. 17:699.

Aunins JG, Henzler HJ. 1993. Aeration in Cell Culture Bioreactors. In: Rehm HJ, Reed G, editors. Biotechnology. New York: VCH. p 223-281.

Bader A, Knop E, Fruhauf N, Crome O, Boker K, Christians U, Oldhafter K, Burkhard R, Pichlmayr R, Sewing KF. 1995. Reconstruction of Liver Tissue *in vitro*: Geometry of Characteristic Flat Bed, Hollow Fiber, and Spouted Bed Bioreactors With Reference to the *in vivo* Liver. Artificial Organs 19:941-950.

Barnes D. 1984. Attachment Factors in Cell Culture. In: Mather J, editor. Mammalian Cell Culture: The Use of Serum-Free Hormone-Supplemented Media. New York: Plenum Press. p 195-237.

Batt DC, Kompala DS. 1989. A Structure Kinetic Modeling Framework for the Dynamics of Hybridoma Growth and Monoclonal Antibody Production in Continuous Culture. Biotechnol. Bioeng. 34:515-531.

Bosch JP, Setin JH. 1993. High-efficiency Treatments. New York: Churchill Livingstone.

Breslau BR, Testa AJ, Milnes BA, Medjanis G. 1980. Advances in Hollow Fiber Ultrafiltration Technology. Polymer Sci. Technol 13:109-127.

Brotherton JD, Chau PC. 1995. Protein-Free Human-Human Hybridoma Cultures in an Intercalated-Spiral Alternate-Dead-Ended Hollow Fiber Bioreactor. Biotechnol. Bioeng. 47:384-400.

Brown BL. 1987. Reducing Costs Upfront: Two Methods for Adapting Hybridoma Cells to an Inexpensive, Chemically Defined Serum-Free Medium. In: Seaver SS, editor. Commercial Production of Monoclonal Antibodies: A Guide for Scale-Up. New York: Marcel-Dekker. p 35-48.

Bruining WJ. 1989. A General Description of Flows and Pressures in Hollow Fiber Membrane Modules. Chem. Eng. Sci. 44:1441-1447.

Butler M. 1987. Animal Cel Technology: Principles and Products. New York: Taylor and Francis.

Butler M, Dawson M. 1992. Cell Culture Labfax. Oxford: BIOS Scientific Publishers.

Butler M, Imamura T, Thomas J, Thilly W. 1983. High Yields from Microcarrier Cultures by Medium Perfusion. J. Cell Sci. 61:351-363.

Cartwright T. 1994. Animal Cells as Bioreactors. New York: Cambridge University Press.

Carvalho A, Malcata X. 2001. Transfer of Carbon Dioxide within Cultures of Microalgae: Plain Bubbling versus Hollow-Fiber Modules. Biotechnol Prog 17(2):265-272.

Casciari J. 1989. The Effects of the Diffusion and Reaction of Nutrients and Metabolic Waste Products on the Growth and Microenvironment of Multicellular Tumor Spheroids [Ph.D. Thesis]. Rochester: University of Rochester. 188 p.

Catapano G. 1996. Mass Transfer Limitations to the Performance of Membrane Bioartificial Liver Support Devices. International J. Art. Organs 19:18-35.

Chick WL, Like AA, Lauris V. 1975. Beta Cell Culture on Synthetic Capillaries: An Artificial Endocrine Pancreas. Science 187:847-849.

Chresand T, Dale B, Hanson S. 1988a. A Stirred Bath Technique for Diffusivity Measurement in Cell Matrices. Biotech Bioeng 32:1029-1036.

Chresand TJ, Gillies RJ, Dale BE. 1988b. Optimum Fibre Spacing in a Hollow Fiber Bioreactor. Biotechnol. Bioeng. 32:983-992.

Colton CK, Lowrie EG. 1981. Kinetics of Hemodiafiltration, I. In: Brenner BM, Reactor FCJ, editors. The Kidney. Philadelphia: Saunders.

Colton CK, Smith KA, Merill WE, Farrell PC. 1971. Permeability Studies with Cellulosic Membranes. J. Biomed. Material Res. 5:459-488.

Cussler E. 1984. Diffusion: Mass Transfer in Fluid Systems. Cambridge: Cambridge University Press.

Czirbik RJ, Rosen SM, Trunfio DM, Fischberg-Bender EW, Palmer SM. 1996. Factors Affecting Antibody Production Efficiency in Hollow-Fiber Bioreactors. IVD Technol. July/August:56-63.

Davis JM, Hanak JAJ, Lewis GM, Chung R, Faulkner J. 1991. Long Term Serum-Free Hollow-Fibre Culture of Cell Lines Producing Monoclonal Antibodies: Metabolic Aspects. In: Spier RE, Griffiths JB, Meignier B, editors. Production of Biologicals from Animal Cells in Culture. Oxford: Butterworth-Heinemann. p 130-133.

Davis M, Watson L. 1985. Analysis of a Diffusion Limited Hollow Fiber Reactor for the Measurement of Effective Substrate Diffusivities. Biotechnol Bioeng 27:182-186.

Deutsch DG, Mertz ET. 1970. Plasminogen: Purification from Human Plasma by Affinity Chromatography. Science 170(962):1095-1096.

deZengotita V, Kimura R, Miller W. 1998. Effects of CO2 and Osmolality on Hybridoma Cells: Growth, Metabolism and Monoclonal Antibody Production. Cytotechnol 28:213-227.

Dowd JE, Kwok KE, Piret JM. 2000. Increased t-PA Yields Using Ultrafiltration of an Inhibitory Product from CHO Fed-Batch Culture. Biotech Prog 16(5):786-794.

Eagle H. 1973. The Effect of Environmental pH on the Growth of Normal and Malignant Cells. J. Cell Physiol. 82:1-8.

Easteal A, Lawrence A. 1986. Diffusion of Protonic Species in Aqueous NaOH as a Function of Concentration, Temperature, and Pressure, and Diffusion of Water in

Aqueous NaF, NaBr, $NaClO_4$, $NaBF_4$,$NaNO_3$, $NaNO_2$, and $NaBrO_3$ at 298 K and 0.1 MPa. J. Phys. Chem. 90:2441-2445.

Edsall J. 1969. CO_2: Chemical, Biochemical, and Physiological Aspects. In: Forster R, Edsall J, Otis A, Roughton F, editors. Washington, D.C.: National Aeronautics and Space Administration. p 15-27.

Evans TL, Miller RA. 1990. Evaluation of Hollow-Fiber Bioreactor Systems for Large-Scale Production of Murine Monoclonal Antibodies. Targeted Diagnosis and Therapy 3:25-43.

Fann CH, Guirgis F, Chen G, Lao MS, Piret JM. 2000. Limitations to the Amplification and Stability of Human Tissue-Type Plasminogen Activator Expression by Chinese Hamster Ovary Cells. Biotech Bioeng 69(2):204-212.

Fatt I, Giasson C, Mueller T. 1998. Non-Steady State Diffusion in a Multilayered Tissue Initiated by Manipulation of Chemical Activity at the Boundaries. Biophysical J 74(1):475-486.

Ferreira B, Fernandes H, Reis A, Mateus M. 1998. Microporous Hollow Fibers for Carbon Dioxide Absorption: Mass Transfer Model Fitting and the Supplying of Carbon Dioxide to Microalgae Cultures. J Chem. Technol. Biotechnol 71(1):61-70.

Fleischaker R, Sinskey A. 1981. Oxygen Demand and Supply in Cell Culture. Eur. J. Appl. Microbiol. Biotechnol. 12:193.

Forsythe GE, Wasow WR. 1960. Finite-Difference Method for Partial Differential Equations. Sokolnikoff IS, editor. New York: John Wiley and Sons, Inc. 444 p.

Freedman RS, Edwards CL, Kavanagh JJ, Kudelka AP, Katz RL, Carrasco CH, Atkinson EN, Scott W, Tomasovic B, Templin S and others. 1994. Intraperitoneal Adoptive Imunotherapy of Ovarian Carcinoma with Tumor-Infiltrating Lymphocytes and Low-Dose Recombinant Interleukin-2: a Pilot Trial. J. Immun. Emphasis Tumor Immunol. 16(3):198-210.

Freshney RI. 1994. Culture of Animal Cells: A Manual of Basic Techniques. New York: Marcel-Dekker.

Glacken MW. 1987. Development of Mathematical Descriptions of Mammalian Cell culture Kinetics for the Optimization of Fed-Batch Bioreactors [Ph.D.]. Cambridge, MA: Massachusetts Institute of Technology.

Glacken MW, Adema E, Sinskey AJ. 1988. Mathematical Descriptions of Hybridoma Culture Kinetics: I. Initial Metabolic Rates. Biotechnol. Bioeng. 32:491-506.

Glacken MW, Fleishaker RJ, Sinskey AJ. 1986. Reduction of Waste Product Excretion via Nutrient Control: Possible Strategies for Maximizing Product and Cell Yields on Serum in Cultures of Mammalian Cells. Biotechnol. Bioeng. 28:1376-1389.

Gorenflo VM, Angepat S, Bowen BD, Piret JM. 2003. Optimization of an Acoustic Cell Filter with a Novel Air-Backflush System. Biotech Prog 19(1):30-36.

Gramer M, Poeschl D. 2000. Comparison of cell growth in t-flasks, in micro hollow fiber bioreactors and in an industrial scale hollow fiber bioreactor system. Cytotechnol 34:111-119.

Gramer M, Poeschl D, Conroy M, Hammer B. 1999. Effect of Harvesting Protocol on Performance of a Hollow Fiber Bioreactor. Biotech Bioeng 65(3):334-340.

Gramer MJ, Poeschl DM. 1998. Screening Tool for Hollow-Fiber Bioreactor Process Development. Biotechnol. Prog. 14:204-209.

Gray D, Chen S, Howarth W, Inlow D, Maiorella B. 1996. CO2 in Large-Scale and High Density CHO Cell Perfusion Culture. Cytotechnol 22:65-78.

Griffiths B. 1986. Scaling-up of Animal Cell Cultures. In: Freshney R, editor. Animal Cell Culture: A Practical Approach. Oxford: IRL Press. p 33-69.

Griffiths B. 1990. Perfusion Systems for Cell Cultivation. In: Lubiniecki A, editor. Large-Scale Mammalian Cell Culture Technology. New York: Marcel-Dekker. p 217-250.

Griffiths JB, Racher AJ. 1994. Cultural and Physiological Factors Affecting Expression of Recombinant Proteins. Cytotechnol 15:3-9.

Gros G, Moll W. 1974. Facilitated diffusion of CO_2 accross albumin solution. J. Gen. Physiol 64:356-371.

Handa-Corrigan A, Nikolay S, Jeffery D, Heffernan B, Young A. 1992a. Controlling and Predicting Monoclonal Antibody Production in Hollow-Fiber Bioreactors. Enzyme Microb. Technol. 14(January):58-63.

Handa-Corrigan A, Nikolay S, Spier R. 1992b. Biochemical Control of Monoclonal Anitbody Secretion in Hollow Fibre Bioreactors. In: Spier R, Griffiths J,

MacDonald C, editors. Animal Cell Technology: Development, Processes and Products. Oxford: Butterworth-Heinemann. p 489-493.

Harlow E, Lane D. 1988. Antibodies - A Laboratory Manual. New York: Cold Spring Harbor Press.

Harned H, Davis R. 1943. The Ionization Constant of Carbonic Acid in Water and the Solubility of Carbon Dioxide in Water and Aqueous Salt Solution from 0 to 50 Degrees. J Amer Chem Soc 65:2030-2037.

Hazel J, Sidell B. 1987. A Method for the Determination of Diffusion Coefficients for Small Molecules in Aqueous Solution. Anal. Biochem. 166:335-341.

Heath C, Belfort G. 1987. Immobilization of Suspended Mammalian Cells: Analysis of Hollow Fibre and Microcapsule Bioreactors. Adv Biochem Eng Biotechnol 34:2-31.

Heifetz AH, Braatz JA, Wolfe RA, Barry RM, Miller DA, Solomon BA. 1989. Monoclonal Antibody Production in Hollow-Fiber Bioreactors Using Serum-Free Medium. BioTechniq. 7(2):192-199.

Henderson LW, Quellhorst EA, Baldamus CA, Lysaght MJ. 1986. Hemofiltration. Berlin: Springer Verlag.

Henry O. 2000. Kinetic Study of Hybridoma Growth and Antibody Production [M. Appl. Sc.]. Vancouver: The University of British Columbia. 93 p.

Henzler H-J, Kauling DJ. 1993. Oxygenation of Cell Cultures. Bioprocess Eng. 9:61-75.

Hillman GG, Wolf ML, Montecillo E, Younes E, Ali E, Pontes JE, Haas GP. 1994. Expansion of Activated Lymphocytes Obtained from Renal Cell Carcinoma in an Automated Hollow Fiber Bioreactor. Cell Transplantation 3(4):263-271.

Inoue Y, Kawamoto S, Seki K, Teruya K, Mochizuki K, Kato M, Hashizume S, Yasumoto K, Nagashima A, Nakahashi H and others. 1996a. Production of Recombinant Human Monoclonal Antibody Using a Novel Hollow Fiber Bioreactor System. J. Ferment. Bioeng. 81(5):466-469.

Inoue Y, Lopez LB, Kawamoto S, Arita N, Teruya K, Seki K, Shoji M, Kamei M, Hashizume S, al. e. 1996b. Production of Recombinant Human Monoclonal Antibody Using *ras*-Amplified BHK-21 Cells in a Protein Free Medium. Biosci. Biotechnol. Biochem. 60(5):811-817.

Jacangelo JG, Aieta EM, Carns KE, Cummings EW, Mallevialle J. 1989. Assessing Hollow-Fiber Ultrafiltration for Particulate Removal. J. AWWA 81:68-75.

Jackson LR, Trudel LJ, Fox JG, Lipman NS. 1996. Evaluation of Hollow Fiber Bioreactors as an Alternative to Murine Ascites Production for Small Scale Monoclonal Antibody Production. J. Immunol. Methods 189:217-231.

Jaffrin MY, Reach G, Notelet D. 1988. Analysis of Ultrafiltration and Mass Transfer in a Bioartificial Pancreas. Trans ASME J Biomech Acta 27:229-246.

Jager V. 1991. Serum-Free Media Suitable for Upstream and Downstream Processing. In: Spier RE, Griffiths JB, Meignier B, editors. Production of Bilogicals from Animal Cells in Culture. Oxford: Butterworth-Heinemann. p 155-164.

Jobses I, Zutphen P, Oomens J, van Os A, Schonherr O. Scaling-Up of a Hollow Fibre Reactor for Animal Cell Cultivation. In: Spier RE, Griffiths JB, MacDonald C, editors. Animal Cell Technology: Developments, Processes and Products; 1992 1992; Brighton, United Kingdom. Butterworth-Heinemann. p 517-522.

Junqueira L, Carneiro J, Long J. 1986. Basic Histology. Norwalk: Appleton-Century-Crofts.

Jurlander B, Thim L, Klausen N, Persson E, Kjalke M, Rexen P, Jorgensen T, Ostergaard P, Erhardtsen E, Bjorn S. 2001. Recombinant Activated Factor VII (rFVIIa): Characterization, Manufacturing, and Clinical Development. Seminars in Thrombosis and Hemostasis 27(4):373-383.

Kamen A, Tom R, Caron A, Chavarie C, Massie B, Archambault J. 1991. Culture of Insect Cells in a Helical Riboon Impeller Bioreactor. Biotech Bioeng 38:619-26.

Kang W, Shukla R, Frank G, Sirkar K. 1988. Evaluation of Oxygen and Carbon Dioxide Transfer Coefficients in a Loclly Integrated Tubular Hollow Fiber Bioreactor. Appl. Biochem. Biotechnol 18:35-51.

Keehan W, Barnes D, Reid L, Stanbridge E, Murakami H, Sato G. 1990. Frontiers in Mammalian Cell Culture. In Vitro Cell. Dev. Biol. 26(1):9-23.

Kelsey L, Pillarella M, Zydney A. 1990. Theoretical Analysis of Convective Flow Profiles in a Hollow-Fiber Membrane Bioreactor. Chem Eng Sci 45:3211-3220.

Kidwell W, Knazek R, Wu Y. 1989. Effect of Fiber Pore Size on Performance of Cells in Hollow Fiber Bioreactors. In: Murakami H, editor. Trends in Animal Cell Culture Technology. Tokyo: Kodansha. p 29-33.

Kigoshi K, Hashitani T. 1963. Self-Diffusion Coefficients of Carbon Dioxide, Hydrogen Carbonate Ions, and Carbonate Ions in Aqueous Solutions. Bulletin Chem Soc Japan 36(10):1372.

Knazek RA, Gullino PM, Kohler PO, Dedrick RL. 1972. Cell Culture on Artificial Capillaries: An Approach to Tissue Growth *in vitro*. Science 178:65-67.

Knazek RA, Wu Y-W, Aebersold PM, Rosenberg SA. 1990. Culture of Human Tumor Infiltrating Lymphocytes in Hollow Fiber Bioreactors. J. Immunol. Methods 127:29-37.

Kohler G, Milstein C. 1975. Continuous Cultures of Fused Cells Secreting Antibody of Predefined Speficity. Nature 256:495-497.

Koska J, Bowen BD, Piret JM. 1997. Protein Transport in Packed-Bed Ultrafiltration Hollow-Fibre Bioreactors. Chem. Eng. Sci. 52:2251-2263.

Kretzmer G, Buch T, Konstantinov K, Naveh D. 1998. The Temperature Effect in Mammalian Cell Culture: an Arrhenius Interpretation. In: Merten O, Perrin P, Griffiths B, editors. New Developments and New Applications in Animal Cell Technology. Dordrecht: Kluwer Academic Publishers. p 363-366.

Krogh A. 1919. The Number and Distribution of Capillaries in Muscles with Calculations of the Oxygen Pressure Head Necessary for Supplying the Tissue. J Physiol 52:409-415.

Kubala L, Ciz M, Soska V, Cerny J, Lojeck A. 2002. Influence of Polysulfone and Hemophan Hemodialysis Membranes on Phagocytes. Gen. Physiol. Biophys. 21:367-380.

Kumar RA, Modak JM. 1997. Transient Analysis of Mammalian Cell Growth in Hollow Fibre Bioreactor. Chem. Eng. Sci. 52(12):1845-4860.

Kurkela R, Fraune E, Vihko P. 1993. Pilot-Scale Production of Murine Monoclonal Antibodies in Agitated, Ceramic-Matrix or Hollow-Fiber Cell Culture Systems. BioTechniq. 15(4):674-683.

Labecki M, Bowen B, Piret JM. 2001. Protein Transport in Ultrafiltration Hollow-Fibre Bioreactors for Mammalian Cell Culture. In: Wang W, editor. Membrane Separation in Biotechnology. New York: Marcel-Dekker. p 1-62.

Labecki M, Bowen BD, Piret JM. 1996. Two-Dimensional Analysis of Protein Transport in the Extracapillary Space of Hollow-Fibre Bioreactors. Chem. Eng. Sci. 51(17):4197-4213.

Labecki M, Piret JM, Bowen B. 2004. Effects of Free Convection on Three-Dimensional Protein Transport in Hollow-Fiber Bioreactors. AIChE Journal 50(8):1974-1990.

Labecki M, Piret JM, Bowen BD. 1995. Two-Dimensional Analysis of Fluid Flow in Hollow-Fibre Modules. Chem. Eng. Sci. 50(21):3369-3384.

Labecki M, Weber I, Dudal Y, Koska J, Piret JM, Bowen BD. 1998. Hindered Transmembrane Protein Transport in Hollow-Fibre Devices. J. Membr. Sci. 146:197-216.

Lamers CHJ, Gratama JW, Luider-Vrieling B, Bolhuis RLH, Bast EJ. 1999. Large-Scale Production of Natural Cytokines During Activation and Expansion of Human T Lymphocytes in Hollow Fiber Bioreactor Cultures. J Immunotherapy 22(4):229-307.

Leveque MA. 1928. Les lois de la Transmission de Chaleur par Convection. Ann. Mines 12:202.

Levick J. 1987. Flow through Interstitium and Other Fibrous Matrices. Quart J Experim Physiol 72:409-438.

Li AP, Barker G, Beck D, Colburn S, Monsell R, Pellegrin C. 1993. Culturing of Primary Hepatocytes as Entrapped Aggregates in a Packed Bed Bioreactor: A Potential Bioartificial Liver. In Vitro Cell Dev. Biology 29A:249-254.

Lide DR. 2004. Handbook of Physics and Chemistry. Cleveland, Ohio: CRC Press. 2656 p.

Liu JJ, Chen B-S, Tsa TF, Wu Y-J, Pang VF, Hsieh A, Hsieh J-H, Chang TH. 1991. Long Term and Large-Scale Cultivation of Human Hepatoma Hep G2 Cells in Hollow Fiber Bioreactor. Cytotechnol 5:129-139.

Livingston E, Miller J, Engel E. 1995. Bicarbonate Diffusion Through Mucus. Amer. J. Physiol 269(3):G453-457.

Lovrecz G, Gebert C, Gray P. On-line qO_2 and qCO_2 Determination for Recombinant Mammalian Cell Fermentation; 1992; Palm Coast, FL.

Lowrey D, Murphy S, Goffe RA. 1993. The Effect of Intracapillary Media Feed Protocols on Hollow Fiber Cell Culture. Biotechnol. Lett. 15:1025-1030.

Lowrey D, Murphy S, Goffe RA. 1994. A Comparison of Monoclonal Antibody Productivity in Different Hollow Fiber Bioreactors. J. Biotechnol. 36:35-38.

Lund P. 1985. L-gutamine and L-glutamate. UV-Method with Glutaminase and Glutamate Dehydrogenase. Methods Enzym. Anal.(8):357-63.

Lynch MP, Nawaz S, Gerschenson LE. 1986. Evidence for Soluble Factors Regulating Cell Death and Cell Proliferation in Primary Cultures of Rabbit Endometrial Cells Grown on Collagen. Proc. Natl. Acad. Sci. USA 83:4784-4788.

Ma RP, Gooding CH, Alexander WK. 1985. A Dynamic Model for Low-Pressure, Hollow-Fibre Ultrafiltration. A.I.Ch.E.J. 31:1728-1732.

Markov S, Bazin M, Hall D. 1995. Hydrogen Photoproduction and Carbon Dioxide Uptake by Immobilized *Anabaena variabilis* in a Hollow-Fiber Photobioreacotr. Enzyme Micro. Technol. 17(4):306-310.

Marshall C, Boraston R, Browne M. 1991. The Effect of Osmolarity on Hybridoma Cell Growth and Antibody Production in Serum-Free Media. In: Spier R, Griffiths J, Meignier B, editors. Produciton of Biologicals from Animal Cells in Culture. Oxford: Butterworth-Heinemann. p 259-261.

Martial A, Dardenne M, Engasser JM, Marc A. 1991. Influence of Inoculum Age on Hybridoma Culture Kinetics. Cytotechnol 5:165-171.

Mather JP, Tsao M. 1990. Expression of Cloned Proteins in Mammalian Cells: Regulation of Cell-Associated Parameters. In: Lubiniecki AS, editor. Large-Scale Mammalian Cell Culture. New York: Marcel-Dekker. p 161-177.

McQueen A, Bailey JE. 1990. Effect of Ammonium Ion and Extracellular pH on Hybridoma Cell Metabolism and Antibody Production. Biotechnol. Bioeng. 35:1067.

Michaels AS. 1980. Fifteen Years of Ultrafiltration: Problems and Future Promises of an Adolescent Technology. Polymer Sci. Technol. 13:1-19.

Miller WM, Blanch HW, Wilke CR. 1988. A Kinetic Analysis of Hybridoma Growth and Metabolism in Batch and Continuous Suspension Culture: Effect of Nutrient Concentration, Dilution Rate, and pH. Biotechnol. Bioeng. 32(10):947-965.

Miltenburger H, David P. 1980. Mass Production of Insect Cells in Suspension. Dev. Biol. Stand. 46:183.

Montagnon B. 1985. Inactivated Polio Vaccine: Industrial Production from Micro-Carrier Vero Cell Culture. Tropical and Geographical Medicine 37(3):s40-1.

Montagnon B. 1989. Polio and Rabies Vaccines Produced in Continuous Cell Lines: a Reality for Vero Cell Line. Develop Biol Standard 70:27-47.

Mueller-Klieser W, Sutherland R. 1982. Oxygen Tension in Multicell Spheroids of Two Cell Lines. Br. J. Cancer 45:256-263.

Noda I, Gryte CC. 1979. Mass Transfer in Regular Arrays of Hollow Fibers in Countercurrent Dialysis. A.I.Ch.E.J. 25:113-122.

Nyberg SL, Shatford RA, Peshwa MV, White JG, Cerra FB, Hu W-S. 1993. Evaluation of a Hepatocyte-Entrapment Hollow Fiber Bioreactor: a Potential Bioartificial Liver. Biotechnol. Bioeng. 41:194-203.

Oetzel GR. Introduction to Ruminal Acidosis in Dairy Cattle; 2003; Columbus, Ohio.

Ohshima N. 1997. Tissue Engineering Aspects of the Development of Bioartificial Livers. Journal of the Chinese Institute of Chemical Engineers 28(6):441-453.

Omasa T, Kobayashi M, Nishikawa T, Shioya S, Suga K, Uemura S, Kitani Y, Imamura Y. 1995. Enhancement of Antibody Production by Growth Factor Addition in Perfusion and Hollow-Fiber Culture System. Biotech Bioeng 48:673-680.

Ong C, Portner R, Markl H, Yamazaki Y, Yasuda K, Matsumura M. 1994. High Density Cultivation of Hybridoma in Charged Porous Carriers. J Biotechnol 34:259-268.

Ozturk SS, Blackie J, Thrift J, Naveh D. Engineering Aspects of Oxygen Mass Transfer, CO_2 Accumulation, and pH Control for Mammalian Cell Culture Bioreactors; 1995; Anaheim, California.

Ozturk SS, Palsson BO. 1990. Chemical Decomposition of Glutamine in Cell Culture Media: Effect of Media Type, pH, and Serum Concentration. Biotechnol. Progress 6(2):121-128.

Ozturk SS, Palsson BO. 1991. Examination of Serum and Bovine Serum Albumin as Shear Protective Agents in Agitated Cultures of Hybridoma Cells. J. Biotechnol. 18:13-28.

Ozturk SS, Riley MR, Palsson BO. 1992. Effects of Ammonia and Lactate on Hybridoma Growth, Metabolism, and Antibody Production. Biotechnol. Bioeng. 39:418-431.

Pankow JF. 1991. Aquatic Chemistry Concepts. Chelsea, Michigan: Lewis Publishers. 673 p.

Pardridge WM, Davidson MB, Casanello-Ertl D. 1978. Glucose and Amino Acid Metabolism in an Established Line of Skeletal Muscle Cells. J. Cell Physiol. 96(3):309-318.

Patkar AY, Koska J, Taylor DG, Bowen BD, Piret JM. 1995. Protein Transport in Ultrafiltration Hollow-Fiber Bioreactors. AIChE J. 41(2):415-425.

Pillarella MR, Zydney AL. 1990. Theoretical Analysis of the Effect of Convective Flow on Solute Transport and Insulin Response in a Hollow Fiber Bioartificial Pancreas. Trans ASME, J Biomech Eng 112:220-228.

Pinton H, Lourenco da Silva A, Goergen J, Marc A, Engasser J, Rabaud J, Pierry G. 1994. Control of the Maixmal Cell Density in a Membrane Perfusion Reactor. In: Spier R, Griffiths B, Berthold W, editors. Animal Cell Technology. Products of Today, Prospects for Tomorrow. Oxford: Butterworth-Heinemann. p 470-475.

Piret JM, Cooney C. 1990a. Mammalian Cell and Protein Distributions in Ultrafiltration Hollow Fiber Bioreactors. Biotechnol. Bioeng. 36:902-910.

Piret JM, Cooney CL. 1990b. Immobilized Mammalian Cell Cultivation in Hollow Fiber Bioreactors. Biotechnol. Adv. 8:763-783.

Piret JM, Cooney CL. 1991. Model of Oxygen Transport Limitations in Hollow Fiber Bioreactors. Biotechnol. Bioeng. 37:80-92.

Piret JM, Devens DA, Cooney CL. 1991. Nutrient and Metabolite Gradients in Mammalian Cell Hollow Fiber Bioreactors. Can. J. Chem. Eng. 69(April):1991.

Press WH, Vetterling WT, Teukolsky SA, Flannery BP. 1986. Numerical Recipes in Fortran, the Art of Scientific Computing IV. Cambridge: Cambridge University Press.

Puck T, Cieciura S, Robinson A. 1958. Genetics of Somatic Mammalian Cells. J. Exp. Med. 108:945-959.

Randy M, Wallen P. 1981. A Sensitive Parabolic Rate Assay for the Tissue Plasminogen Activator. In: Davidson JF, Nilsson IM, Astedt B, editors. Progress in Fibrinolysis. Edinburgh: Churchill Livingstone. p 233-235.

Reif O, Solkner P, Rupp J. 1996. Analysis and Evaluation of Filter Cartridge Extractables for Validation in Pharmaceutical Downstream Processing. PDA J Pharm Sci Tech 50(6):399-410.

Reuveny S, Velez D, Riske F, Macmillan J, Miller L. 1985. Production of monoclonal antibodies in culture. Develop Biol Standard 60:185-197.

Robb WL. 1968. Thin Silicone Membranes- Their Permeation Properties and Some Applications. Ann. NY Acad. Sci. 37:1680.

Rony PR. 1971. Multiphase Catalysis, II. Hollow Fiber Catalysts. Biotechnol. Bioeng. 13:431-447.

Ross PR. 1974. A Mathematical Model of Mass Transfer in a Long Permeable Tube with Radial Convection. J. Fluid Mech. 63:157-175.

Rozga J, Williams F, Ro M-S, Neuzil DF, Giorgio TD, Backfisch G, Moscioni AD, Hakim R, Demetriou AA. 1993. Development of a Bioartificial Liver: Properties and Function of a Hollow-Fiber Module Inoculated with Liver Cells. Hepatology 17(2):258-265.

Ruff I, Friedrich V. 1972. Transfer Diffusion. IV. A Numerical Test of the Correlation between Prototrope Mobility and Proton Exchange Rate of H_3O^+ and OH^- Ions with Water. J. Phys. Chem. 76(21):2954-2957.

Ryan GB, Simpson MT, Jones WT, Nicol MJ, Reynolds PHS. Effect of Dissolved Oxygen on Monoclonal Antibody Production from Hybriodma Cultured in Haemodialysers. In: Spier RE, Griffiths JB, Berthold W, editors. Animal Cell Technology: Products of Today, Prospects for Tomorrow; 1994. Butterworth-Heinemann.

Ryll T, Lucki-Lange M, Jager V, Wagner R. 1990. Production of Recombinant Human Interleukin-2 with BHK Cells in a Hollow Fibre and a Stirred Tank Reactor with Protein-Free Medium. J. Biotechnol. 14:377-392.

Salmon PM, Libicki SB, Robertson CR. 1988. A Theoretical Investigation of Convective Transport in the Hollow-Fiber Reactor. Chem. Eng. Commun. 66:221-248.

Sardonini C, DiBiasio D. 1992. An Investigation of the Diffusion-Limited Growth of Animal Cells around Single Hollow Fibers. Biotechnol Bioeng 40:1233-1242.

Sardonini CA, DiBiasio D. 1993. Growth of Animal Cells Around Hollow Fibers: Multifiber Studies. AIChe J. 39:1415-1419.

Schonberg J, Belfort G. 1987. Enhanced Nutrient Transport in Hollow Fiber Perfusion Bioreactors. Biotechnol Prog 3:80-89.

Seigel GM, Liu L. 1997. Inducible Apoptosis-Promoting Activity in Retinal Cell-Conditioned Medium. Molecular Vision 3(14).

Shatford RA, Nyberg SL, Meier SJ, White JG, Payne WD, Hu W-S, Cerra FB. 1992. Hepatocyte Function in a Hollow Fiber Bioreactor: a Potential Bioartificial Liver. J. Surg. Res. 53(6):549-557.

Sheil AGR, Sun J, Mears DC, Waring M, Woodman K, Johnston B, Horvat M, Watson KJ, Koutalistras N, Wang L-S. 1996. Preclinical Trial of a Bioartificial Liver Support System in a Porcine Fulminant Hepatic Failure Model. Austral. New Zeal. J. Surg. 66:547-552.

Sigdell JE. 1981. Comparison of Hollow-Fiber Dialyzers. Artif. Organs 5:401-409.

Soli A, Byrne R. 2002. CO_2 system Hydration and Dehydration Kinetics and the Equilibrium CO_2/H_2CO_3 Ratio in Aqueous NaCl Solution. Marine Chemistry 78:65-73.

Sowter HM, Ratcliffe PJ, Watson P, Greenberg AH, Harris AL. 2001. HIF-1-dependent Regulation of Hypoxic Induction of the Cell Death Factors BNIP3 and NIX in Human Tumors. Cancer Res 61:6669-6673.

Sperandio M, Paul E. 1997. Determination of Carbon Dioxide Evolution Rate Using On-Line Gas Analysis During Biodegradation Experiments. Biotechnol. Bioeng. 53(3):243-252.

Sueoka A, Takakura K. 1991. Hollow Fiber Membrane Application for Blood Treatment. Polym. J. 23:561-571.

Swabb E, Wei J, Gullino P. 1974. Diffusion and Convection in Normal and Neoplastic Tissues. Cancer Res 34:2814-2822.

Tabouy L, Chauvet-Monges A, Brunet P, Braguer D, Garcia P, Berland Y, Crevat A. 1997. *In vitro* Mitochondrial Test to Assess Haemodialyser Biocompatibility. Nephrol. Dial. Transplant 12:1635-1639.

Takagi M, Fukuda N, Yoshida T. 1997. Comparison of Different Hepatocyte Cell Line for Use in a Hybrid Artificial Liver Model. Cytotechnol 24:39-45.

Tanase T, Ikeda Y, Iwama K, Hashimoto A, Kataoka T, Tokushima Y, Kobayashi T. 1997. Comparison of Micro-Filtration Hollow Fiber Bioreactors for Mammalian Cell Culture. J. Ferment. Bioeng. 83(5):499-501.

Tannock I. 1968. The Relationship between Cell Proliferation and the Vascular System in a Transplanted Mouse Mammory Tumor. Br. J. Cancer 22:258-273.

Taylor DG, Piret JM, Bowen BD. 1994. Protein Polarization in Isotropic Membrane Hollow-Fiber Bioreactors. AIChE Journal 40(2):321-333.

Tharakan J, Chau P. 1986. A Radial Flow Hollow Fiber Bioreactor for the Large-Scale Culture of Mammalian Cells. Biotechnol Bioeng 28:329-342.

Tharakan JP, Gallagher S, Chau PC. 1988. Hollow Fiber Bioreactors in Mammalian Cell Culture. Adv. Biotechnol. Process 7:153-184.

Thelwall PE, Brindle K. 1999. Analysis of CHO-K1 Cell Growth in a Fixed Bed Bioreactor Using Magnetic Resonance Spectroscopy and Imaging. Cytotechnol 30:121-132.

Thomas JN. 1990. Mammalian Cell Physiology. In: Lubiniecki AS, editor. Large-Scale Mammalian Cell Culture Technol. New York: Marcel-Dekker. p 93-145.

Thomlinson R, Gray L. 1955. The Histological Structure of Some Human Lung Cancers and the Possible Implications for Radiotherapy. Br. J. Cancer 9:539-549.

Treat JC, Sandelin KK, Beiderman BC, Kirschner RJ. 1997. Low- and High-Producing Animal Cell Cultures in Perfused, Packed Beds of Non-Woven Fabric. Animal Cell Technol. (M.J.T. Carrondo et al. eds.):313-318.

Uchida K, Doi K. 1992. Measurements of Carbon Dioxide Diffusivity and Buffering Capacity in Myoglobin Solutions. Jap. J. Physiol 42(1):89-100.

Uchida K, Mochizuki M, Niizeki K. 1983. Diffusion Coefficients of Carbon Dioxide Molecule and Bicarbonate Ion in Hemoglobin Solution Measured by Fluorescence Technique. Jap. J. Physiol 33(4):619-634.

van Erp R, Adorf M, van Sommerren APG, Gribnau TCJ. 1991b. Monitoring of the Production of Monoclonal Antibodies by Hybridomas: Part II: Charaterization and Purification of Acid Proteases Present in Cell Culture Supernatant. J. Biotechnol. 20:249-262.

van Erp R, Adorf M, van Sommerren APG, Schonherr OT, Gribnau TCJ. 1991a. Monitoring of the Production of Monoclonal Antibodies by Hybridomas: Part I: Long-Term Cultivation in Hollow Fibre Bioreactors Using Serum-Free Medium. J. Biotechnol. 20:235-248.

Vanysek P. 1999. Ionic Conductivity and Diffusion at Infinite Dilution. In: D. L, editor. CRC Handbook of Chemistry and Physics. 79 ed. London: CRC Press.

Verheihen JH, Mullaart E, Chang G, Kluft C, Wijngaards G. 1982. A Simple, Sensitive Spectrophotometric Assay for Extrinsic (Tissue-Type) Plasminogen Activator Applicable to Measurements in Plasma. Thromb. Haemostas. 48:266-269.

Vilker VL, Colton CK, Smith KA. 1981. Concentration Polarization in Protein Ultrafiltration. AIChE. J 27(632).

Wang SK, Hwang NH. 1992. On Transport of Suspended Particulates in Tube Flow. Biorheology 29(2-3):353-377.

Waterland LR, Michaels AS, Robertson CR. 1975. Enzymatic Catalysis Using Asymmetric Hollow Fiber Membranes. Chem. Eng. Comm. 2:37-47.

Webster I, Shuler M. 1979. Whole-Cell Hollow Fiber Reactor: Effectiveness Factors. Biotechnol Bioeng 21:1725-1748.

Webster I, Shuler M. 1981. The Measurement of Effective Substrate Diffusivities within Whole Cell Suspensions Using a Diffusion-Limited Hollow Fiber Reactor. J. Chem. Tech. Biotechnol. 31:226-234.

Webster IA, Shuler ML. 1978. Mathematical Models for Hollow-Fiber Enzyme Reactors. Biotechnol. Bioeng. 20:1541-1556.

Wei J, Russ M. 1977. Convection and diffusion in tissues and tissue cultures. J. Theoret. Biol. 66:775-787.

Wu FJ, Friend JR, Lazar A, Mann HJ, Remmel RP, Cerra FB, Wu WS. 1996. Hollow Fiber Bioartificial Liver Utilizing Collagen-Entrapped Porcine Hepatocyte Spheroids. Biotechnol. Bioeng. 52:34-44.

Yoshikawa S, Ogawa K, Minegishi S, Eguchi T, Nakatani Y, Tani N. 1992. Experimental Study of Flow Mechanics in a Hollow-Fiber Membrane Module for Plasma Separation.

Zanghi J, Schmeizer A, Mendoza T, Knop R, Miller W. 1999. Biocarbonate Concentration and Osmolality Are Key Determinants in the Inhibition of CHO Cell Polysialylation Under Elevated pCO2 or pH. Biotech. Bioeng. 65(2):182-191.

Zeilke HR, Zeilke CL, Ozand PT. 1984. Glutamine: A Major Energy Source for Cultured Mammalian Cells. Federation Proc. 43:121-125.

Zupke C, Green J. Modeling of CO_2 Concentration in Small and Large Scale Bioreactors; 1998; San Diego, California.

Zydney AL, Colton CK. 1982. Continuous Flow Membrane Plasmapheresis: Theoretical Models for Flux and Hemolysis Prediction. Trans. Am. Soc. Intern. Organs 28:408-412.

Appendix A

This model estimates the concentration profiles in various regions, i.e. the ECS, the membrane, and the ICS of the HFBR, and also provides predictions of the concentrations of carbon dioxide and its related species at the outlet of the HFBR. The differential equations that govern the concentration distributions were solved using a finite difference method known as the implicit difference method. The entire Krogh cylinder can be represented as a m x n grid (Figure A.1), where the subscript i represents the radial direction and k represents the axial direction.

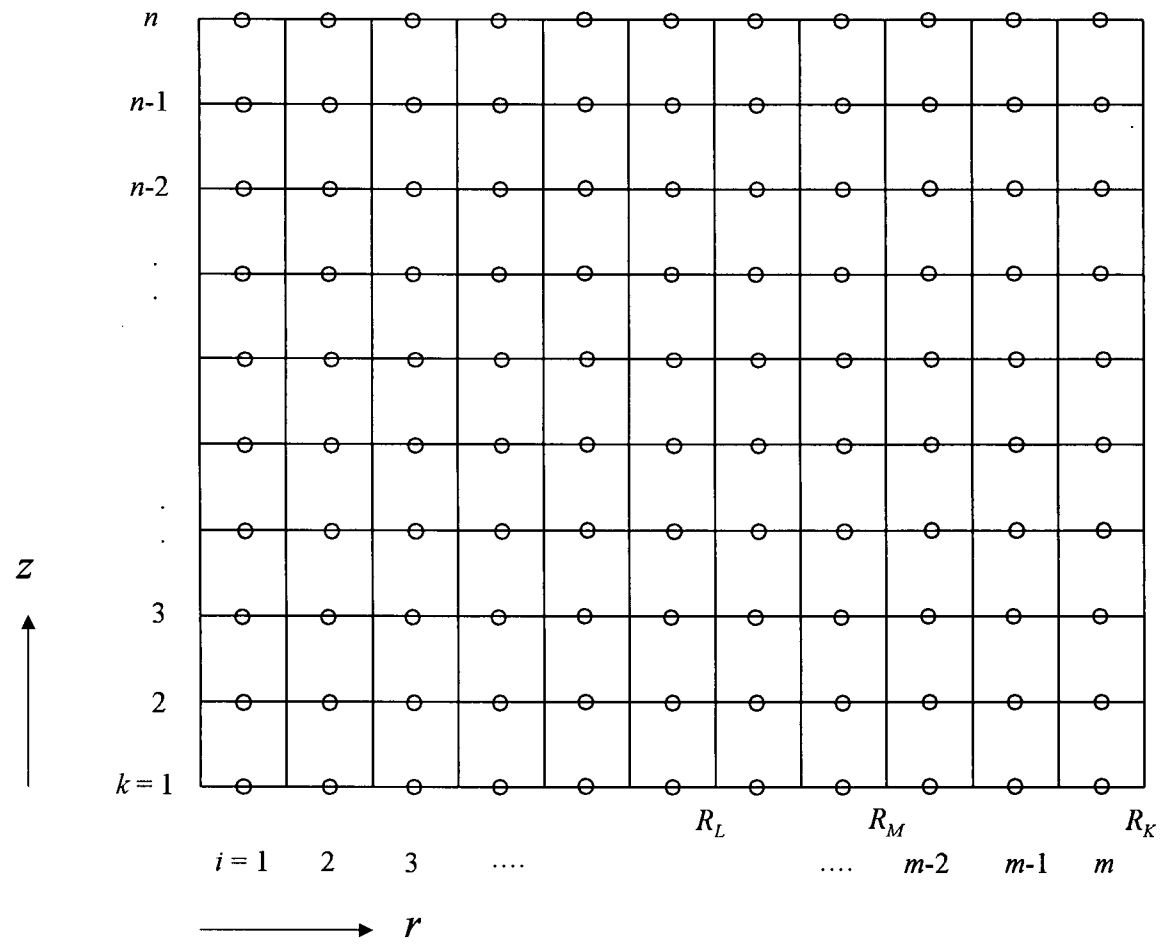

Figure A.1 Staggered grid

Each node (*i*, *k*) was assumed to have its own characteristic velocity in the *z*-direction, v_i, species diffusivity in the *r*-direction, D_i, and species volumentric production rate, R_i. Using the implicit difference method, the PDEs (Equation 5.2) were approximated by a central difference in the radial direction and backward difference in the axial direction at any position (*i*, *k*+*1*) (see Figure A.2).

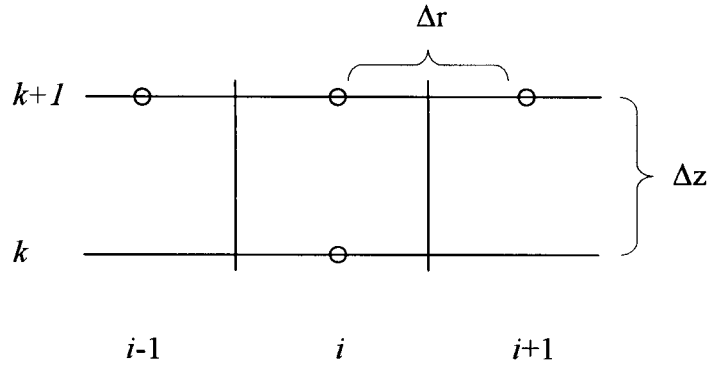

Figure A.2 Control volume surrounding the node (*i*,*k*+*1*)

Using the species CO_2 at node (*i*,*k*+*1*) as an example, Equation 5.2 becomes

$$v_i\left[(r_i+\Delta r/2)^2-(r_i-\Delta r/2)^2\right]\left(C_{CO_2,i,k}-C_{CO_2,i,k+1}\right)\cdot\pi+$$

$$\frac{C_{CO_2,i-1,k+1}-C_{CO_2,i,k+1}}{\frac{\ln\left((r_i+\Delta r/2)/r_{i-1}\right)}{2\cdot\pi\cdot\Delta z\cdot D_{CO_2,i-1}}+\frac{\ln\left(r_i/(r_i-\Delta r/2)\right)}{2\cdot\pi\cdot\Delta z\cdot D_{CO_2,i}}}-\frac{C_{CO_2,i,k+1}-C_{CO_2,i,k+1}}{\frac{\ln\left((r_i+\Delta r/2)/r_{i-1}\right)}{2\cdot\pi\cdot\Delta z\cdot D_{CO_2,i}}+\frac{\ln\left(r_{i+1}/(r_{i+1}-\Delta r/2)\right)}{2\cdot\pi\cdot\Delta z\cdot D_{CO_2,i+1}}}+$$

$$\left(X_i\cdot sCER-k_H\cdot C_{CO_2,i,k+1}+k_D\cdot C_{H_2CO_3,i,k+1}\right)\left[\pi\cdot\Delta z\left((r_i+\Delta r/2)^2-(r_i-\Delta r/2)^2\right)\right]=0 \qquad \textbf{(A.1)}$$

At position *i*, let $\gamma=r_i\cdot\Delta r$, $R^{+}_{CO_2,i}=\gamma\ln\left((r_i+\Delta r/2)/r_{i-1}\right)/D_{CO_2,i}$,

$R^{-}_{CO_2,i}=\gamma\ln\left(r_i/(r_i-\Delta r/2)\right)/D_{CO_2,i}$

Also, $(r_i+\Delta r/2)^2-(r_i-\Delta r/2)^2=2\cdot r_i\cdot\Delta r$

Equation A.1 can then be simplified to

$$\frac{v_i}{\Delta z}\left(C_{CO_2,i,k}-C_{CO_2,i,k+1}\right)+\frac{C_{CO_2,i-1,k+1}-C_{CO_2,i,k+1}}{R^+_{CO_2,i-1}+R^-_{CO_2,i}}-\frac{C_{CO_2,i,k+1}-C_{CO_2,i,k+1}}{R^+_{CO_2,i}+R^-_{CO_2,i+1}}+$$
$$X_i\cdot sCER-k_H\cdot C_{CO_2,i,k+1}+k_D\cdot C_{H_2CO_3,i,k+1}=0 \qquad \textbf{(A.2)}$$

Similarly, for H_2CO_3 at node (i,k) , the PDE becomes,

$$\frac{v_i}{\Delta z}\left(C_{H_2CO_3,i,k}-C_{H_2CO_3,i,k+1}\right)+\frac{C_{H_2CO_3,i-1,k+1}-C_{H_2CO_3,i,k+1}}{R^+_{H_2CO_3,i-1}+R^-_{H_2CO_3,i}}-\frac{C_{H_2CO_3,i,k+1}-C_{H_2CO_3,i,k+1}}{R^+_{H_2CO_3,i}+R^-_{H_2CO_3,i+1}}+$$
$$k_H\cdot C_{CO_2,i,k+1}-k_D\cdot C_{H_2CO_3,i,k+1}=0 \qquad \textbf{(A.3)}$$

It was assumed that there is no transport at $r=R_K$, and, hence, at the node $(m, k+1)$ the grid becomes that shown in Figure A.3,

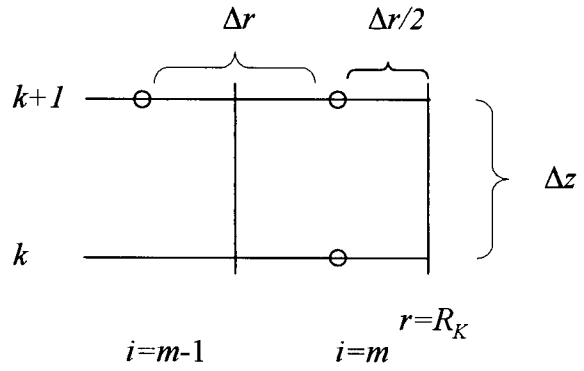

Figure A.3 Control volume surrounding the node $(m,k+1)$

Equation 5.2 for CO_2 now becomes

$$v_m\left[(r_m+\Delta r/2)^2-(r_m-\Delta r/2)^2\right]\left[C_{CO_2,m,k}-C_{CO_2,m,k+1}\right)\cdot\pi+$$
$$\frac{C_{CO_2,m-1,k+1}-C_{CO_2,m,k+1}}{\frac{\ln\left((r_m+\Delta r/2)/r_{m-1}\right)}{2\cdot\pi\cdot\Delta z\cdot D_{CO_2,m-1}}+\frac{\ln\left(r_m/(r_m-\Delta r/2)\right)}{2\cdot\pi\cdot\Delta z\cdot D_{CO_2,m}}}+ \qquad \textbf{(A.4)}$$
$$\left(X_m\cdot sCER-k_H\cdot C_{CO_2,m,k+1}+k_D\cdot C_{H_2CO_3,m,k+1}\right)\left[\pi\cdot\Delta z\left((r_m+\Delta r/2)^2-(r_m-\Delta r/2)^2\right)\right]=0$$

Rearranging and substituting as previously shown for CO_2, Equation A.4 becomes

$$\frac{v_m}{\Delta z}\left(C_{CO_2,m,k}-C_{CO_2,m,k+1}\right)+\frac{C_{CO_2,m-1,k+1}-C_{CO_2,m,k+1}}{R^+_{CO_2,m-1}+R^-_{CO_2,m}}+X_m\cdot sCER-k_H\cdot C_{CO_2,m,k+1}+ \quad \textbf{(A.5)}$$
$$k_D\cdot C_{H_2CO_3,m,k+1}=0$$

Similarly, the PDE for species H_2CO_3 at node $(m,k+1)$ becomes

$$\frac{v_m}{\Delta z}\left(C_{H_2CO_3,m,k}-C_{H_2CO_3,m,k+1}\right)+\frac{C_{H_2CO_3,m-1,k+1}-C_{H_2CO_3,m,k+1}}{R^+_{H_2CO_3,m-1}+R^-_{H_2CO_3,m}}+k_H\cdot C_{CO_2,m,k+1}- \quad \textbf{(A.6)}$$
$$k_D\cdot C_{H_2CO_3,m,k+1}=0$$

Note that, unless $C_{CO_2,i,k+1}$ and $C_{H_2CO_3,i,k+1}$ appear in the source terms, then the CO_2 and H_2CO_3 equations are not linked and BTMA method is not needed.

At r=0, it was assumed that there is no transport, and at the node (0, $k+1$) the grid becomes that shown in Figure A.4,

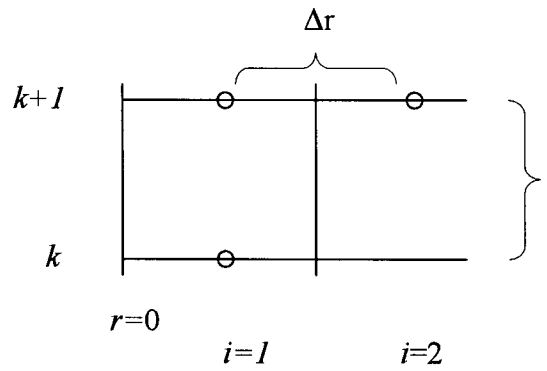

Figure A.4 Control volume surrounding the node $(1,k+1)$

Equation 5.2 for CO_2 becomes

$$v_1\cdot\pi\cdot\Delta r^2\left(C_{CO_2,1,k}-C_{CO_2,1,k+1}\right)-\frac{C_{CO_2,1,k+1}-C_{CO_2,2,k+1}}{\frac{\ln\left((r_1+\Delta r/2)/r_1\right)}{2\cdot\pi\cdot\Delta z\cdot D_{CO_2,1}}+\frac{\ln\left(r_2/(r_2-\Delta r/2)\right)}{2\cdot\pi\cdot\Delta z\cdot D_{CO_2,2}}}+ \quad \textbf{(A.7)}$$
$$\left(X_1\cdot sCER-k_H\cdot C_{CO_2,1,k+1}+k_D\cdot C_{H_2CO_3,1,k+1}\right)\left[\pi\cdot\Delta z\cdot\Delta r^2\right]=0$$

Rearranging and substituting as previously shown for CO_2, Equation A.7 becomes

$$\frac{v_1}{\Delta z}\left(C_{CO_2,1,k} - C_{CO_2,1,k+1}\right) - \frac{C_{CO_2,1,k+1} - C_{CO_2,2,k+1}}{R^+_{CO_2,1} + R^-_{CO_2,2}} + X_1 \cdot sCER - k_H \cdot C_{CO_2,1,k+1} + k_D \cdot C_{H_2CO_3,1,k+1} = 0 \quad \textbf{(A.8)}$$

Similarly, the PDE for species H_2CO_3 at node $(1,k+1)$ becomes

$$\frac{v_1}{\Delta z}\left(C_{H_2CO_3,1,k} - C_{H_2CO_3,1,k+1}\right) - \frac{C_{H_2CO_3,1,k+1} - C_{H_2CO_3,2,k+1}}{R^+_{H_2CO_3,1} + R^-_{H_2CO_3,2}} + k_H \cdot C_{CO_2,1,k+1} - k_D \cdot C_{H_2CO_3,1,k+1} = 0 \quad \textbf{(A.9)}$$

The initial conditions for the PDEs are shown in Equation 5.3. At $z=0$, the ICS inlet concentrations for all species are known. In order to solve for all the species concentrations in the membrane and ECS, it was assumed that a very small z was used to approximate the initial concentrations at the inlet. Using a control volume approach similar to Equation A.1, the PDEs for CO_2 and H_2CO_3 for $R_L < r < R_K$ at $z=0$ are

$$f_{CO_2,i} = \frac{C_{CO_2,i-1,1} - C_{CO_2,i,1}}{R^+_{CO_2,i-1} + R^-_{CO_2,i}} - \frac{C_{CO_2,i,1} - C_{CO_2,i+1,1}}{R^+_{CO_2,i} + R^-_{CO_2,i+1}} + X_i \cdot sCER - k_H \cdot C_{CO_2,i,1} + k_D \cdot C_{H_2CO_3,i,1} = 0 \quad \textbf{(A.10)}$$

$$f_{H_2CO_3,i} = \frac{C_{H_2CO_3,i-1,1} - C_{H_2CO_3,i,1}}{R^+_{H_2CO_3,i-1} + R^-_{H_2CO_3,i}} - \frac{C_{H_2CO_3,i,1} - C_{H_2CO_3,i+1,1}}{R^+_{H_2CO_3,i} + R^-_{H_2CO_3,i+1}} + k_H \cdot C_{CO_2,i,1} - k_D \cdot C_{H_2CO_3,i,1} = 0 \quad \textbf{(A.11)}$$

At $r=R_L$ and $z=0$, $i = (R_L / \Delta r) + 1 = l$ (see Figure A.5)

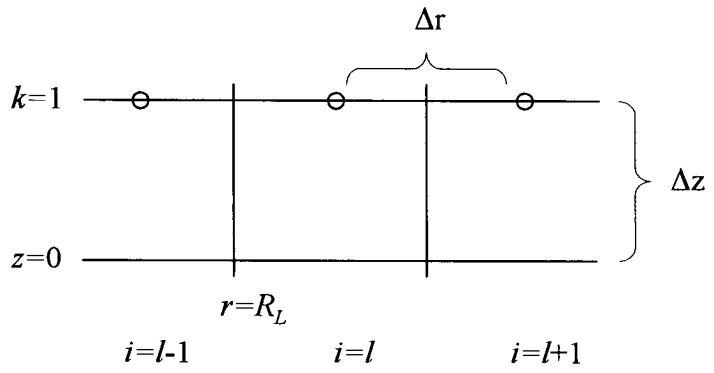

Figure A.5 The grid at r=R_L and z=0

The interface concentration is set as

$$C_{CO_2,l-1,1} = 2 \cdot C_{CO_2,0,1} - C_{CO_2,l,1}$$
$$C_{H_2CO_3,l-1,1} = 2 \cdot C_{H_2CO_3,0,1} - C_{H_2CO_3,l,1}$$

where $C_{CO_2,0,1}$ and $C_{H_2CO_3,0,1}$ are the constant inlet ICS values at z=0. Thus, the PDEs at $r=R_L$ and z=0 for CO_2 and H_2CO_3 become

$$f_{CO_2,1} = \frac{2 \cdot C_{CO_2,0,1} - 2 \cdot C_{CO_2,l,1}}{R^+_{CO_2,l-1} + R^-_{CO_2,l}} - \frac{C_{CO_2,l,1} - C_{CO_2,l+1,1}}{R^+_{CO_2,l} + R^-_{CO_2,l+1}} + X_l \cdot sCER - k_H \cdot C_{CO_2,l,1} + k_D \cdot C_{H_2CO_3,l,1} = 0 \quad \textbf{(A.12)}$$

$$f_{H_2CO_3,1} = \frac{2 \cdot C_{H_2CO_3,0,1} - 2 \cdot C_{H_2CO_3,l,1}}{R^+_{H_2CO_3,l-1} + R^-_{H_2CO_3,l}} - \frac{C_{H_2CO_3,l,1} - C_{H_2CO_3,l+1,1}}{R^+_{H_2CO_3,l} + R^-_{H_2CO_3,l+1}} + k_H \cdot C_{CO_2,l,1} - k_D \cdot C_{H_2CO_3,l,1} = 0 \quad \textbf{(A.13)}$$

At $r=R_K$ and z=0, $i = R_K / \Delta r = m$. The PDEs at $r=R_L$ and z=0 become

$$f_{CO_2,m} = \frac{C_{CO_2,m-1,1} - C_{CO_2,m,1}}{R^+_{CO_2,m-1} + R^-_{CO_2,m}} + X_m \cdot sCER - k_H \cdot C_{CO_2,m,1} + k_D \cdot C_{H_2CO_3,m,1} = 0 \quad \textbf{(A.14)}$$

$$f_{H_2CO_3,m} = \frac{C_{H_2CO_3,m-1,1} - C_{H_2CO_3,m,1}}{R^+_{H_2CO_3,l-1} + R^-_{H_2CO_3,l}} + k_H \cdot C_{CO_2,m,1} - k_D \cdot C_{H_2CO_3,m,1} = 0 \quad \textbf{(A.15)}$$

To solve for the initial conditions (i.e. at z=0), Newton's method was used to find the ICS equilibrium concentration of all species. For CO_2 and H_2CO_3, a block tridiagonal matrix (BTDM) can be formed for the nodes from $r=R_L$ to $r=R_K$ as shown below.

$$\begin{bmatrix} \frac{\partial f_{CO_2,i}}{\partial C_{CO_2,i-1,1}} & \frac{\partial f_{CO_2,i}}{\partial C_{H_2CO_3,i-1,1}} \\ \frac{\partial f_{H_2CO_3,i}}{\partial C_{CO_2,i-1,1}} & \frac{\partial f_{H_2CO_3,i}}{\partial C_{H_2CO_3,i-1,1}} \end{bmatrix} \cdot \begin{bmatrix} \Delta C_{CO_2,i-1,1} \\ \Delta C_{H_2CO_3,i-1,1} \end{bmatrix} + \begin{bmatrix} \frac{\partial f_{CO_2,i}}{\partial C_{CO_2,i,1}} & \frac{\partial f_{CO_2,i}}{\partial C_{H_2CO_3,i,1}} \\ \frac{\partial f_{H_2CO_3,i}}{\partial C_{CO_2,i,1}} & \frac{\partial f_{H_2CO_3,i}}{\partial C_{H_2CO_3,i,1}} \end{bmatrix} \cdot \begin{bmatrix} \Delta C_{CO_2,i,1} \\ \Delta C_{H_2CO_3,i,1} \end{bmatrix}$$
$$+ \begin{bmatrix} \frac{\partial f_{CO_2,i}}{\partial C_{CO_2,i+1,1}} & \frac{\partial f_{CO_2,i}}{\partial C_{H_2CO_3,i+1,1}} \\ \frac{\partial f_{H_2CO_3,i}}{\partial C_{CO_2,i+1,1}} & \frac{\partial f_{H_2CO_3,i}}{\partial C_{H_2CO_3,i+1,1}} \end{bmatrix} \cdot \begin{bmatrix} \Delta C_{CO_2,i+1,1} \\ \Delta C_{H_2CO_3,i+1,1} \end{bmatrix} = \begin{bmatrix} -f_{CO_2,i} \\ -f_{H_2CO_3,i} \end{bmatrix} \quad \textbf{(A.16)}$$

To calculate the initial concentration from $i=l$ to $i=m$ (from membrane to ECS), all concentrations at z=0 were first set equal to the ICS inlet concentrations. For CO_2 and H_2CO_3, the matrices shown in Equation A.16 can be generated. Using the BTDM method, the differences between the calculated concentrations and the initial estimated, e.g., ΔC, can be obtained. The maximum error of the change in the concentrations was calculated (where error=|max(ΔC)/max(C)|). If the maximum error is greater than 10^{-6}, the concentrations estimated in the first iteration will be incorporated into the re-evaluation of the matrix elements (Equation A.16) and the BTDM method will be used to solve for a new set of concentration values. This process will continue until the maximum error is less than 10^{-6}.

Once the initial concentrations were solved, the species concentrations at the next Δz step was calculated similarly, where i = 1 to i = m (compared to i = l to i = m at z=0). This process was repeated until the entire axial length, L, was traversed.

Appendix B

```
%%%      function co2data.m
%%%%%%%%%%%%%%%%%%%%%%%%%%%%%%%%%%%%%%%%%%%%%%%%%%%%%%%%%%%%%%%%%%
%%%                    Parameters for Gambro 16 Plus Cartridge                  %%%
%%%%%%%%%%%%%%%%%%%%%%%%%%%%%%%%%%%%%%%%%%%%%%%%%%%%%%%%%%%%%%%%%%
%%%
%%%   Physical dimensions of cartridge
%%%
rl = 1.05e-4;               % lumen radius [m] original=1.05e-4
rm = 1.13e-4;               % outer radius of fibre [m] original=1.13e-4
rk = 1.61e-4;               % Krogh cylinder radius [m] original=1.61e-4
L = 0.21;                   % effective length of hollow fibre [m]
num = 10500;                % number of fibres
%
%    Physical properties
%
D1= 2.4e-9;                 % diffusivity of carbon dioxide in water [m^2/s] from Aunin and Henzler, 1993
D1eff = D1*0.5;             % effective diffusivity of carbon dioxide in cell [m^2/s] non-charged species 50%
D2 = 4.23e-9;               % diffusivity for H2CO3 calculated from eq.
D2eff = D2*0.5;             % effective diffusivity using non-charged species 50%
D3 = 1.25e-8;               % H+ from Vanysek P., 2001
D3eff = D3*0.5;             % H+ charged species 50%
D4 = 1.48e-9;               % OH- in salt solution from Easteal and Lawrence, 1986
D4eff = D4*0.5;             % OH- charged species 50%
D5 = 1.52e-9;               % HCO3- for saline at 37 degrees, Livingston et al. 1995
D5eff = D5*0.5;             % HCO3- charged species 50%
D6 = 1.15e-9;               % for water at 37 degrees, Kigoshi and Hashitani, 1963
D6eff = D6 *0.5;            % using Swab et al. 1974 correlation
D7 = 0.75e-9;               % in water at 37 degrees, Hazel and Sidell, 1987
D7eff = D7 * 0.5;           % using Swab et al. 1974 correlation
epsilon = 0.8;              % porosity of membrane sponge wall
flowrate = 300/6e7;         % ICS recirculation flow rate [m^3/s] or 300 [mL/min]
rgrid = 1e-6;               % radial grid size [m]
zgrid = 5e-6;               % axial grid size [m]
%
%     Rate Constants
%
Kw = 1e-14*1000000;         % water dissociation constant for [H+] and [OH-] in [mol/m^3]
Ka1 = 10^-2.99*1000;        % first acid dissociaiton constant at 32.5 C [mol/m^3] from Soli and Byrne, 2002
Ka2 = 10^-10.25*1000;       % second acid dissociation constant at 35 C [mol/m^3] from Pankow, 1991
KH = 1/878;                 % CO2 hydration/dehydration at 32.5 C from Soli and Byrne, 2002
kD = 50.2;                  % H2CO3 dehydration rate constant [1/s]
kH = 0.057;                 % Co2 hydration rate constant  [1/s]
%
%    Initial  guesses of species concentrations [mol/m^3]
%
pHo = 7.113;
CO2o = 1.5867e-3*1000;
H2CO3o = 4.5e-6*1000;
Ho = 10^-(pHo)*1000;
OHo = 1e-8/(Ho);
HCO3o = 0.04405*1000;
Nao = (0.04405+ 0.11665)*1000;
CO3o = 2.3776e-6*1000;
Clo = 0.11665*1000;         % included contribution for NaCl and KCl
Laco = 0;
%
%    Cell Specific Rates
%
sCER = 0.03e-12/3600;       % specific carbon dioxide evolution rate [mol/cell s] assuming respiration quotient of 1.0  from Gray et. al., 1995
sGUR = 3*3e-18;             % specific glucose uptake rate [mol/cell s] from batch culture estimation
sLPR = 1.5*sGUR;            % specific lactate production rate assuming 1 glucose -> 1.5 lactate
X = 3e14;                   % cell density [cell/m^3] or 3e8 [cells/mL]



%%%      function  co2model.m
%%%%%%%%%%%%%%%%%%%%%%%%%%%%%%%%%%%%%%%%%%%%%%%%%%%%%%%%%%%%%%%%%%%%%
%%%      7 species 2-D Krogh Cylinder Carbon Dioxide Transport Model                 %%%
%%%      modified saving only at position z = 0, 0.105, 0.21 m                       %%%
%%%%%%%%%%%%%%%%%%%%%%%%%%%%%%%%%%%%%%%%%%%%%%%%%%%%%%%%%%%%%%%%%%%%%
%
%        Load initial parameters
%
%%%%                                             %%%%
%%%%  using C(k-1)=2*Co-C(k)
%%%%  see June 4, 2003 hand-written notes
%%%%  specie 1 = CO2(aq)
%%%%  specie 2 = H2CO3
%%%%  specie 3 = H+
%%%%  specie 4 = OH-
%%%%  specie 5 = HCO3-
%%%%  specie 6 = CO3--
%%%%  specie 7 = Lac-
%%%%  assume lactate is converted to lactate ion and hydrogen ion
```

```
%%%%
%
format long e
tic
%
%  declaring global variables
%
global Kw Ka1 Ka2 KH Ct Nao Clo
%
%            Call up Gambro 16 Plus Cartridge parameters and equilibrium constants from
%            file co2modeldata.m
%
co2data
%
%            Set grid
%
m = round(rk/rgrid);                          % number of grids in r-direction
n = round(L/zgrid);                           % number of grids in z-direction
l = round(rl/rgrid)+1;                        % border to the lumen/membrane
k = round(rm/rgrid)+1;                        % border to the membrane/cell layer
Vavg = flowrate/(pi*num*(rl^2));              % average axial velocity
%
%            Df, diffusivity matrix,
%            Q, cell specific carbon dioxide production rate
%            Rdist, radial distance
%            gamma = radial distance * radial rgrid size
%            V, characteristic velocity in the z-direction
%
Df = zeros(8,m);
Q = zeros(m,1);
Qlac = zeros(m,1);
Rdist = zeros(m,1);
gamma = zeros(m,1);
V = zeros(m,1);
count = zeros(n,1);
for i = 1:l-1
  Df(:,i) = [D1; D2; D3; D4; D5; D6; D7; D1];
  %%%       assume diffusivities for carbon dioxide, bicarbonate ion, hydrogen ion, etc. are all the same          %%%
  Rdist(i,1) = rgrid*i - (rgrid/2);
  gamma(i,1) = rgrid*Rdist(i,1);
  %%%       assume parabolic axial velocity profile       %%%
  V(i,1) = 2*Vavg*(1-(Rdist(i,1)/rl)^2);
end
for i = l:k-1
  Df(:,i) = [D1*epsilon; D2*epsilon; D3*epsilon; D4*epsilon; D5*epsilon; D6*epsilon; D7*epsilon; D1*epsilon];
  Rdist(i,1) = rgrid*i - (rgrid/2);
  gamma(i,1) = rgrid*Rdist(i,1);
end
for i = k:m
  Df(:,i) = [D1eff; D2eff; D3eff; D4eff; D5eff; D6eff; D7eff; D1eff];
  Q(i,1) = sCER*X;
  Qlac(i,1) = sLPR*X;
  Rdist(i,1) = rgrid*i - (rgrid/2);
  gamma(i,1) = rgrid*Rdist(i,1);
end
%%%%%%%%%%%%%%%%%%%%%%%%%%%%%%%%%%%%%%%%%%%%%%%%%%%%%%%%%%%%%%
%%%          Find radial oxygen concentration at z=0                          %%%
%%%%%%%%%%%%%%%%%%%%%%%%%%%%%%%%%%%%%%%%%%%%%%%%%%%%%%%%%%%%%%
%
%            Rplus and Rminus are defined on written sheet, where there's no difference between species A,B,C
%
Rplus = zeros(8,m);
Rminus = zeros(8,m);
for j = 1:8
   for i = 1:m
      if i == 1
         Rminus(j,1) = 0;
         Rplus(j,1) = (log((Rdist(i,1)+(rgrid/2))/Rdist(i,1))) / Df(j,1);
      else
         Rminus(j,i) = (log(Rdist(i,1)/(Rdist(i,1)-(rgrid/2)))) / Df(j,i);
         Rplus(j,i) = (log((Rdist(i,1)+(rgrid/2))/Rdist(i,1))) / Df(j,i);
      end
   end
end
%
%  Cminus and Cplus are the denominator terms where
%       Cminus = gamma(i) * (Rplus(i-1) + Rminus(i))
%       Cplus = gamma(i) * (Rplus(i) + Rminus (i+1))
%
Cminus = zeros (8,m);
Cplus = zeros (8,m);
for j = 1:8
   for i = 2:m
      Cminus(j,i) = (gamma(i,1) * (Rplus(j,i-1) + Rminus(j,i)));
   end
   for i = 1:m-1
      Cplus(j,i) = (gamma(i,1) * (Rplus(j,i) + Rminus(j,i+1)));
   end
end
%%%
%%%      Note: CO2(aq) and H2CO3 will be solve using block tridiagonal matrix
%%%            and the remaining species will be solved by Thomas algorithm
%%%
```

```
%%
%%                Setting block tridiagnoal matrix
%%
Acoeff = zeros(2,2,m-l+1);
Bcoeff = zeros(2,2,m-l+1);
Ccoeff = zeros(2,2,m-l+1);
Dcoeff = zeros(2,m-l+1);
C1 = zeros(m-l+1,1);
C2 = zeros(m-l+1,1);
D1 = zeros(m-l+1,1);
D2 = zeros(m-l+1,1);
%
%  finding the ICS equilibrium concentrations in ICS at z=0
%  using EquilCO2funv7.m
%
temp=EquilCO2funv7([CO2o;H2CO3o;Ho;OHo;HCO3o;CO3o],Laco);
CO2o = temp(1,1);
H2CO3o = temp(2,1);
Ho = temp(3,1);
OHo = temp(4,1);
HCO3o = temp(5,1);
CO3o = temp(6,1);
%
%  Initial guess of concentrations
%
for i = 1:m-l+1
   C1(i,1) = CO2o;
   C2(i,1) = H2CO3o;
end
%
%  Initial guess for functions FA, FB
%
D1(1,1) = -Q(l,1)-2*(CO2o /(Cminus(1,l)));
D2(1,1) = -2*H2CO3o/(Cminus(2,l));
D1(m-l+1,1) = -Q(m,1);
D2(m-l+1,1) = 0;
for i=2:m-l
   D1(i,1) = -Q(l+i-1,1);
   D2(i,1) = 0;
end
%
%                First matrix
%
Bcoeff(:,:,1) = [(-2/(Cminus(1,l))) - 1/Cplus(1,l) - kH, kD;
                 kH, (-2/(Cminus(2,l))) - 1/Cplus(2,l) - kD];
Ccoeff(:,:,1) = [(1)/(Cplus(1,l)), 0;
                  0, (1)/(Cplus(2,l))];
Dcoeff(:,1) = [D1(1,1); D2(1,1)];
%
%  Last matrix
%
Acoeff(:,:,m-l+1) = [1/(Cminus(1,m)), 0;
                     0, 1/(Cminus(2,m))];
Bcoeff(:,:,m-l+1) = [(-1/(Cminus(1,m))) - kH, kD;
                     kH, (-1/(Cminus(2,m))) - kD];
Dcoeff(:,m-l+1) = [D1(m-l+1,1); D2(m-l+1,1)];
for i=2:m-l
   Acoeff(:,:,i) = [ 1/(Cminus(1,l+i-1)), 0;
                     0, 1/(Cminus(2,l+i-1))];
   Bcoeff(:,:,i) = [(-1/(Cminus(1,l+i-1))) - (1/(Cplus(1,l+i-1))) - kH , kD;
                     kH , (-1/(Cminus(2,l+i-1))) - (1/(Cplus(2,l+i-1))) - kD];
   Ccoeff(:,:,i) = [1/(Cplus(1,l+i-1)), 0, ;
                     0, 1/(Cplus(2,l+i-1))];
   Dcoeff(:,i) = [D1(i,1); D2(i,1)];
end
%
%  Finding the change in the concentratios from the first guess using block tridiagonal matrix solver, BTDMA3.m
%
C=btdma3(Acoeff,Bcoeff,Ccoeff,Dcoeff);
temp=C';
C1=temp(:,1);
C2=temp(:,2);
%
%  setting the intial concentration
%  from 0 to Rk
%
for i = 1:1:m
   C1(i,1)=C1(i-l+1,1);
   C2(i,1)=C2(i-l+1,1);
end
for i=1:l-1
   C1(i,1)=CO2o;
   C2(i,1)=H2CO3o;
end
%%%
%%%      Note: Solving H+ concentration at z = 0 by Thomas algorithm
%%%
%%
%%                Setting tridiagnoal matrix
%%
Acoeff = zeros(m-l+1,1);
Bcoeff = zeros(m-l+1,1);
Ccoeff = zeros(m-l+1,1);
```

```
Dcoeff = zeros(m-l+1,1);
%
%  First matrix
%
Bcoeff(1,1) = -2/(Cminus(3,l)) - 1/(Cplus(3,l));
Ccoeff(1,1) = 1/(Cplus(3,l));
Dcoeff(1,1) = -2*Ho/(Cminus(3,l))-Qlac(l,1);
%
%  Remaining matrix
%
for i=2:m-l
   Acoeff(i,1) = 1/(Cminus(3,l+i-1));
   Bcoeff(i,1) = -(1/Cminus(3,l+i-1)+1/Cplus(3,l+i-1));
   Ccoeff(i,1) = 1/Cplus(3,l+i-1);
   Dcoeff(i,1) = -Qlac(l+i-1,1);
end
%
%  Last matrix
%
Acoeff(m-l+1,1) = 1/(Cminus(3,m));
Bcoeff(m-l+1,1) = -1/Cminus(3,m);
Dcoeff(m-l+1,1) = -Qlac(m,1);
C3=tdmsolve(Acoeff,Bcoeff,Ccoeff,Dcoeff);
for i = l:1:m
   C3(i,1)=C3(i-l+1,1);
end
for i=1:l-1
   C3(i,1)=Ho;
end
%%%
%%%      Note: Solving OH concentration at z = 0 by Thomas algorithm
%%%
%%
%%               Setting tridiagnoal matrix
%%
%
%  First matrix
%
Bcoeff(1,1) = -2/(Cminus(4,l)) - 1/(Cplus(4,l));
Ccoeff(1,1) = 1/(Cplus(4,l));
Dcoeff(1,1) = -2*OHo/(Cminus(4,l));
%
%  Remaining matrix
%
for i=2:m-l
   Acoeff(i,1) = 1/(Cminus(4,l+i-1));
   Bcoeff(i,1) = -(1/Cminus(4,l+i-1)+1/Cplus(4,l+i-1));
   Ccoeff(i,1) = 1/Cplus(4,l+i-1);
   Dcoeff(i,1) = 0;
end
%
%  Last matrix
%
Acoeff(m-l+1,1) = 1/(Cminus(4,m));
Bcoeff(m-l+1,1) = -1/Cminus(4,m);
Dcoeff(m-l+1,1)=0;
C4=tdmsolve(Acoeff,Bcoeff,Ccoeff,Dcoeff);
for i = l:1:m
   C4(i,1)=C4(i-l+1,1);
end
for i=1:l-1
   C4(i,1)=OHo;
end
%%%
%%%      Note: Solving HCO3 concentration at z = 0 by Thomas algorithm
%%%
%%
%%               Setting tridiagnoal matrix
%%
%
%  First matrix
%
Bcoeff(1,1) = -2/(Cminus(5,l)) - 1/(Cplus(5,l));
Ccoeff(1,1) = 1/(Cplus(5,l));
Dcoeff(1,1) = -2*HCO3o/(Cminus(5,l));
%
%  Remaining matrix
%
for i=2:m-l
   Acoeff(i,1) = 1/(Cminus(5,l+i-1));
   Bcoeff(i,1) = -(1/Cminus(5,l+i-1)+1/Cplus(5,l+i-1));
   Ccoeff(i,1) = 1/Cplus(5,l+i-1);
   Dcoeff(i,1) = 0;
end
%
%  Last matrix
%
Acoeff(m-l+1,1) = 1/(Cminus(5,m));
Bcoeff(m-l+1,1) = -1/Cminus(5,m);
C5=tdmsolve(Acoeff,Bcoeff,Ccoeff,Dcoeff);
for i = l:1:m
   C5(i,1)=C5(i-l+1,1);
end
```

```
for i=1:l-1
  C5(i,1)=HCO3o;
end
%%%
%%%      Note: Solving CO3= concentration at z = 0 by Thomas algorithm
%%%
%%
%%              Setting tridiagnoal matrix
%%
%
%  First matrix
%
Bcoeff(1,1) = -2/(Cminus(6,l)) - 1/(Cplus(6,l));
Ccoeff(1,1) = 1/(Cplus(6,l));
Dcoeff(1,1) = -2*CO3o/(Cminus(6,l));
%
%  Remaining matrix
%
for i=2:m-1
  Acoeff(i,1) = 1/(Cminus(6,l+i-1));
  Bcoeff(i,1) = -(1/Cminus(6,l+i-1)+1/Cplus(6,l+i-1));
  Ccoeff(i,1) = 1/Cplus(6,l+i-1);
  Dcoeff(i,1) = 0;
end
%
%  Last matrix
%
Acoeff(m-l+1,1) = 1/(Cminus(6,m));
Bcoeff(m-l+1,1) = -1/Cminus(6,m);
C6=tdmsolve(Acoeff,Bcoeff,Ccoeff,Dcoeff);
for i = l:1:m
  C6(i,1)=C6(i-l+1,1);
end
for i=1:l-1
  C6(i,1)=CO3o;
end
%%%
%%%      Note: Solving Lac- concentration at z = 0 by Thomas algorithm
%%%
%%
%%              Setting tridiagnoal matrix
%%
%
%  First matrix
%
Bcoeff(1,1) = -2/(Cminus(7,l)) - 1/(Cplus(7,l));
Ccoeff(1,1) = 1/(Cplus(7,l));
Dcoeff(1,1) = -2*Laco/(Cminus(7,l))-Qlac(l,1);
%
%  Remaining matrix
%
for i=2:m-1
  Acoeff(i,1) = 1/(Cminus(7,l+i-1));
  Bcoeff(i,1) = -(1/Cminus(7,l+i-1)+1/Cplus(7,l+i-1));
  Ccoeff(i,1) = 1/Cplus(7,l+i-1);
  Dcoeff(i,1) = -Qlac(l+i-1,1);
end
%
%  Last matrix
%
Acoeff(m-l+1,1) = 1/(Cminus(7,m));
Bcoeff(m-l+1,1) = -1/Cminus(7,m);
Dcoeff(m-l+1,1) = -Qlac(m,1);
C7=tdmsolve(Acoeff,Bcoeff,Ccoeff,Dcoeff);
for i = l:1:m
  C7(i,1)=C7(i-l+1,1);
end
for i=1:l-1
  C7(i,1)=Laco;
end
%%%
%%%   Calculating the equilibrium concentrations of all 7 species at z=0 using
%%%   EquilCO2funv7.m solving at each "i" position assuming CO2
%%%   doesn't change
%%%
species = zeros(6,m,4);
for i=1:m
  speciestemp = [C1(i,1); C2(i,1); C3(i,1); C4(i,1); C5(i,1); C6(i,1)];
  species(:,i,1) = EquilCO2funv7(speciestemp, C7(i,1));
end
lactate(:,1)=C7;
sptemp=species(:,:,1);
%
%
%%%
%%%
%%%
%%%   Calculation CO2(aq) and H2CO3 Concentrations at z>0
%%%
%%%
%%%
%
%  initializing the species
```

```
%
D1 = zeros(m,1);
D2 = zeros(m,1);
C7N=C7;
for j=2:n+1
  C1 = sptemp(1,:,1)'; C2 = sptemp(2,:,1)'; C3 = sptemp(3,:,1)'; C4 = sptemp(4,:,1)';
  C5 = sptemp(5,:,1)'; C6 = sptemp(6,:,1)';  C7=C7N;
  Acoeff = zeros(2,2,m);
  Bcoeff = zeros(2,2,m);
  Ccoeff = zeros(2,2,m);
  Dcoeff = zeros(2,m);
  %
  %  Initial guess for functions FA, FB
  D1(1,1) = -V(1,1)/zgrid*C1(1,1) - Q(1,1);
  D2(1,1) = -V(1,1)/zgrid*C2(1,1);
  D1(m,1) = -Q(m,1);
  D2(m,1) = 0;
  for i=2:m-1
    D1(i,1) = -V(i,1)/zgrid*C1(i,1) - Q(i,1);
    D2(i,1) = -V(i,1)/zgrid*C2(i,1);
  end
  %
  %              First matrix
  %
  Bcoeff(:,:,1) = [-V(1,1)/zgrid - 1/Cplus(1,1) - kH, kD;
                   kH, -V(1,1)/zgrid - 1/Cplus(2,1) - kD];
  Ccoeff(:,:,1) = [(1)/(Cplus(1,1)), 0;
                    0, (1)/(Cplus(2,1))];
  Dcoeff(:,1) = [D1(1,1); D2(1,1)];
  %
  %  Last matrix
  %
  Acoeff(:,:,m) = [1/(Cminus(1,m)), 0;
                    0, 1/(Cminus(2,m))];
  Bcoeff(:,:,m) = [(-1/(Cminus(1,m))) - kH, kD;
                   kH, (-1/(Cminus(2,m))) - kD];
  Dcoeff(:,m) = [D1(m,1); D2(m,1)];
  for i=2:m-1
    Acoeff(:,:,i) = [ 1/(Cminus(1,i)), 0;
                      0, 1/(Cminus(2,i))];
    Bcoeff(:,:,i) = [-V(i,1)/zgrid + (-1/(Cminus(1,i))) - (1/(Cplus(1,i))) - kH , kD;
                      kH , -V(i,1)/zgrid + (-1/(Cminus(2,i))) - (1/(Cplus(2,i))) - kD];
    Ccoeff(:,:,i) = [1/(Cplus(1,i)), 0, ;
                     0, 1/(Cplus(2,i))];
    Dcoeff(:,i) = [D1(i,1); D2(i,1)];
  end
  %
  %  Finding the change in the concentratios from the first guess using block tridiagonal matrix solver, BTDMA3.m
  %
  C=btdma3(Acoeff,Bcoeff,Ccoeff,Dcoeff);
  temp=C';
  C1N=temp(:,1);
  C2N=temp(:,2);
  %%%
  %%%       Note: Solving H+ concentration at z > 0 by Thomas algorithm
  %%%
  %%
  %%              Setting tridiagnoal matrix
  %%
  Acoeff = zeros(m,1);
  Bcoeff = zeros(m,1);
  Ccoeff = zeros(m,1);
  Dcoeff = zeros(m,1);
  %
  %  First matrix
  %
  Bcoeff(1,1) = -V(1,1)/zgrid - 1/(Cplus(3,1));
  Ccoeff(1,1) = 1/(Cplus(3,1));
  Dcoeff(1,1) = -V(1,1)/zgrid*C3(1,1) - Qlac(1,1);
  %
  %  Remaining matrix
  %
  for i=2:m-1
    Acoeff(i,1) = 1/(Cminus(3,i));
    Bcoeff(i,1) = -V(i,1)/zgrid - 1/Cminus(3,i) - 1/Cplus(3,i);
    Ccoeff(i,1) = 1/Cplus(3,i);
    Dcoeff(i,1) = -V(i,1)/zgrid*C3(i,1) - Qlac(i,1);
  end
  %
  %  Last matrix
  %
  Acoeff(m,1) = 1/(Cminus(3,m));
  Bcoeff(m,1) = -1/Cminus(3,m);
  Dcoeff(m,1) = -Qlac(m,1);
  C3N=tdmsolve(Acoeff,Bcoeff,Ccoeff,Dcoeff);
  %%%
  %%%       Note: Solving OH concentration at z > 0 by Thomas algorithm
  %%%
  %%
  %%              Setting tridiagnoal matrix
  %%
  %
  %  First matrix
```

```
%
Bcoefff(1,1) = -V(1,1)/zgrid - 1/(Cplus(4,1));
Ccoefff(1,1) = 1/(Cplus(4,1));
Dcoefff(1,1) = -V(1,1)/zgrid*C4(1,1);
%
%  Remaining matrix
%
for i=2:m-1
   Acoefff(i,1) = 1/(Cminus(4,i));
   Bcoefff(i,1) = -V(i,1)/zgrid - 1/Cminus(4,i) - 1/Cplus(4,i);
   Ccoefff(i,1) = 1/Cplus(4,i);
   Dcoefff(i,1) = -V(i,1)/zgrid*C4(i,1);
end
%
%  Last matrix
%
Acoefff(m,1) = 1/(Cminus(4,m));
Bcoefff(m,1) = -1/Cminus(4,m);
Dcoefff(m,1) = 0;
C4N=tdmsolve(Acoefff,Bcoefff,Ccoefff,Dcoefff);
%%%
%%%      Note: Solving HCO3 concentration at z = 0 by Thomas algorithm
%%%
%%
%%            Setting tridiagnoal matrix
%%
%
%  First matrix
%
Bcoefff(1,1) = -V(1,1)/zgrid - 1/(Cplus(5,1));
Ccoefff(1,1) = 1/(Cplus(5,1));
Dcoefff(1,1) = -V(1,1)/zgrid*C5(1,1);
%
%  Remaining matrix
%
for i=2:m-1
   Acoefff(i,1) = 1/(Cminus(5,i));
   Bcoefff(i,1) = -V(i,1)/zgrid - 1/Cminus(5,i) - 1/Cplus(5,i);
   Ccoefff(i,1) = 1/Cplus(5,i);
   Dcoefff(i,1) = -V(i,1)/zgrid*C5(i,1);
end
%
%  Last matrix
%
Acoefff(m,1) = 1/(Cminus(5,m));
Bcoefff(m,1) = -1/Cminus(5,m);
Dcoefff(m,1) = 0;
C5N=tdmsolve(Acoefff,Bcoefff,Ccoefff,Dcoefff);
%%%
%%%      Note: Solving CO3= concentration at z > 0 by Thomas algorithm
%%%
%%
%%            Setting tridiagnoal matrix
%%
%
%  First matrix
%
Bcoefff(1,1) = -V(1,1)/zgrid - 1/(Cplus(6,1));
Ccoefff(1,1) = 1/(Cplus(6,1));
Dcoefff(1,1) = -V(1,1)/zgrid*C6(1,1);
%
%  Remaining matrix
%
for i=2:m-1
   Acoefff(i,1) = 1/(Cminus(6,i));
   Bcoefff(i,1) = -V(i,1)/zgrid - 1/Cminus(6,i) - 1/Cplus(6,i);
   Ccoefff(i,1) = 1/Cplus(6,i);
   Dcoefff(i,1) = -V(i,1)/zgrid*C6(i,1);
end
%
%  Last matrix
%
Acoefff(m,1) = 1/(Cminus(6,m));
Bcoefff(m,1) = -1/Cminus(6,m);
Dcoefff(m,1) = 0;
C6N=tdmsolve(Acoefff,Bcoefff,Ccoefff,Dcoefff);
%%%
%%%      Note: Solving Lac- concentration at z = 0 by Thomas algorithm
%%%
%%
%%            Setting tridiagnoal matrix
%%
%
%  First matrix
%
Bcoefff(1,1) = -V(1,1)/zgrid - 1/(Cplus(7,1));
Ccoefff(1,1) = 1/(Cplus(7,1));
Dcoefff(1,1) = -V(1,1)/zgrid*C7(1,1) - Qlac(1,1);
%
%  Remaining matrix
%
for i=2:m-1
   Acoefff(i,1) = 1/(Cminus(7,i));
```

```
    Bcoeff(i,1) = -V(i,1)/zgrid - 1/Cminus(7,i) - 1/Cplus(7,i);
    Ccoeff(i,1) = 1/Cplus(7,i);
    Dcoeff(i,1) = -V(i,1)/zgrid*C7(i,1) - Qlac(i,1);
  end
  %
  %  Last matrix
  %
  Acoeff(m,1) = 1/(Cminus(7,m));
  Bcoeff(m,1) = -1/Cminus(7,m);
  Dcoeff(m,1) = -Qlac(m,1);
  C7N=tdmsolve(Acoeff,Bcoeff,Ccoeff,Dcoeff);
  %%%
  %%%   Calculating the equilibrium concentrations of all 7 species using
  %%%   EquilCO2funv6.m solving at each "i" position assuming CO2
  %%%   doesn't change
  %%%
  for i=1:m
    speciestemp = [C1N(i,1); C2N(i,1); C3N(i,1); C4N(i,1); C5N(i,1); C6N(i,1)];
    sptemp(:,i,1) = EquilCO2funv6(speciestemp, C7N(i,1));
  end
  C7=C7N;
  if j == (n/3+1)
    species(:,:,2)=sptemp;
    lactate(:,2)=C7N;
  end
  if j == (n*2/3+1)
    species(:,:,3)=sptemp;
    lactate(:,3)=C7N;
  end
  if j==(n+1)
    species(:,:,4)=sptemp;
    lactate(:,4)=C7N;
  end
  j
end
toc



%%%          function EquilCO2funv6.m
%%%%%%%%%%%%%%%%%%%%%%%%%%%%%%%%%%%%%%%%%%%%%%%%%%%%%%%%%%%%%%%%%%%%%%%%%%%%%%%%%%%%%%%%%%%%%%%%%%%%%%%%%%%
%%%          EquilCO2funv6.m is a Matlab function file that calculates the equilibrium          %%%
%%%          concentrations of all 7 species of interest with CO2 set constant                  %%%
%%%%%%%%%%%%%%%%%%%%%%%%%%%%%%%%%%%%%%%%%%%%%%%%%%%%%%%%%%%%%%%%%%%%%%%%%%%%%%%%%%%%%%%%%%%%%%%%%%%%%%%%%%%
function result = EquilCO2funv6(x,lac);
global Kw Ka1 Ka2 KH Ct Nao Clo;
  tol=1e-6; maxit=50;
  iter=0; maxdx=1e10;
  %initialize the matrix that contains the values of the partial differential equations
  a=zeros(6,7);
  %these values remain constant, thus they are assigned as constants
  a(1,3) = -1; a(1,4) = 1; a(1,5) = 1; a(1,6) = 2;
  a(2,2) = Ka1;
  a(3,5) = Ka2;
  a(5,1) = 1;
  a(6,1) = -1; a(6,2) = -1; a(6,5) = -1; a(6,6) = -1;
  %iterate to find the updated solution vector
  while iter<maxit & maxdx>tol;
    iter=iter+1; maxdx=0;
    a(2,3) = -x(5); a(2,5) = -x(3);
    a(3,3)= -x(6); a(3,6) = -x(3);
    a(4,3) = -x(4); a(4,4)= -x(3);
    a(1:6,7) = -Equilfun6(x,lac);
    dx = gauss(a);
     x = x + dx';
    maxdx=max(abs(dx'./x));
  end;
  if maxdx<=tol
    result=[x]; %assign the converged values of the 8 non-linear equations
  else
    error(' Newtons method did not converge')
  end



%%%          function Equilfun6.m
%%%%%%%%%%%%%%%%%%%%%%%%%%%%%%%%%%%%%%%%%%%%%%%%%%%%%%%%%%%%%%%%%%%%%%%%%%%%%%%%%%%%%%
%%%          function that defines 6 non-linear equations to be solved for region z>0    %%%
%%%          with CO2 constant                                                            %%%
%%%%%%%%%%%%%%%%%%%%%%%%%%%%%%%%%%%%%%%%%%%%%%%%%%%%%%%%%%%%%%%%%%%%%%%%%%%%%%%%%%%%%%
function xfun = Equilfun6(x,lac);
%x(1) = CO2
%x(2) = H2CO3
%x(3) = H+
%x(4) = OH-
%x(5) = HCO3-
%x(6) = CO3=
%x(7) = Lac-
global Kw Ka1 Ka2 Ct KH Nao Clo
  Ct = x(1) + x(2) + x(5) + x(6);
  xfun=zeros(6,1);
```

```
  xfun(1,1) = x(5) + x(6)*2 + x(4) - x(3) + lac - Nao + Clo; %electroneutrality balance
  xfun(2,1) = Ka1*x(2) - x(5)*x(3);          %first acid dissociation of carbonic acid
  xfun(3,1) = Ka2*x(5) - x(6)*x(3);          %second acid dissociation of carbonic acid
  xfun(4,1) = Kw - x(3)*x(4);                %water dissociation reaction
  xfun(5,1) =0;                              %CO2 hydration/dehydration
  xfun(6,1) = Ct - x(2) - x(5) -x(6) -x(1);  %total carbon species material balance
```

```
%%%        function EquilCO2funv7.m
%%%%%%%%%%%%%%%%%%%%%%%%%%%%%%%%%%%%%%%%%%%%%%%%%%%%%%%%%%%%%%%%%%%
%%%        EquilCO2funv7.m is a Matlab function file that calculates the equilibrium        %%%
%%%        concentrations of all 7 species of interest                                      %%%
%%%%%%%%%%%%%%%%%%%%%%%%%%%%%%%%%%%%%%%%%%%%%%%%%%%%%%%%%%%%%%%%%%%
function result = EquilCO2funv7(x,lac);
global Kw Ka1 Ka2 KH Ct Nao Clo;
  tol=1e-6; maxit=50;
  iter=0; maxdx=1e10;
  %initialize the matrix that contains the values of the partial differential equations
  a=zeros(6,7);
  %these values remain constant, thus they are assigned as constants
  a(1,3) = -1; a(1,4) = 1; a(1,5) = 1; a(1,6) = 2;
  a(2,2) = Ka1;
  a(3,5) = Ka2;
  a(5,1) = KH; a(5,2)= -1;
  a(6,1) = -1; a(6,2) = -1; a(6,5) = -1; a(6,6) = -1;
  %iterate to find the updated solution vector
  while iter<maxit & maxdx>tol;
    iter=iter+1; maxdx=0;
    a(2,3) = -x(5); a(2,5) = -x(3);
    a(3,3)= -x(6); a(3,6) = -x(3);
    a(4,3) = -x(4); a(4,4)= -x(3);
    a(1:6,7) = -Equilfun7(x,lac);
    dx = Gauss(a);
    x = x + dx';
    maxdx=max(abs(dx'./x));
  end;
  if maxdx<=tol
    result=[x]; %assign the converged values of the 8 non-linear equations
  else
    error(' Newtons method did not converge')
  end
```

```
%%%        function Equilfun7.m
%%%%%%%%%%%%%%%%%%%%%%%%%%%%%%%%%%%%%%%%%%%%%%%%%%%%%%%%%%%%%%
%%%        function that defines 6 non-linear equations to be solved at z=0        %%%
%%%        solving for 7 species                                                  %%%
%%%%%%%%%%%%%%%%%%%%%%%%%%%%%%%%%%%%%%%%%%%%%%%%%%%%%%%%%%%%%%
function xfun = Equilfun7(x,lac);
%x(1) = CO2
%x(2) = H2CO3
%x(3) = H+
%x(4) = OH-
%x(5) = HCO3-
%x(6) = CO3=
%x(7) = Lac-
global Kw Ka1 Ka2 Ct KH Nao Clo
  Ct = x(1) + x(2) + x(5) + x(6);
  xfun=zeros(6,1);
  xfun(1,1) = x(5) + x(6)*2 + x(4) - x(3) + lac - Nao + Clo; %electroneutrality balance
  xfun(2,1) = Ka1*x(2) - x(5)*x(3);          %first acid dissociation of carbonic acid
  xfun(3,1) = Ka2*x(5) - x(6)*x(3);          %second acid dissociation of carbonic acid
  xfun(4,1) = Kw - x(3)*x(4);                %water dissociation reaction
  xfun(5,1) = x(1)*KH - x(2);                %CO2 hydration/dehydration
  xfun(6,1) = Ct - x(2) - x(5) -x(6) -x(1);  %total carbon species material balance
```

```
%%%        function gauss.m
function x = gauss(A)
%          'gauss.m is a function m-file that uses Gauss elimination with
%          partial pivot selection to solve linear equations of the form:
%          [A]*{x} = {c}
%
% Input argument:
% A = augmented coefficient matrix with the column vector of rhs
%    constants, c, included as its n+1st column
%
% Output argument:
% x = array of solution values
  n = size(A,1); nm = n-1; np = n+1;
% Carry out elimination process n-1 times
  for k = 1:nm
    kp = k+1;
%           Search for largest coefficient of x(k) for rows k through
%           n. pivot_row is the row index of the largest coefficient.
    maxAik = abs(A(k,k)); pivot = k;
    for i = kp:n
```

```
      absAik = abs(A(i,k));
      if absAik > maxAik
        maxAik = absAik; pivot = i;
      end
    end
%           Exchange rows k and pivot_row if pivot_row ~= k
    if pivot ~= k
      for j = k:np
        temp = A(pivot,j);
        A(pivot,j) = A(k,j);
        A(k,j) = temp;
      end
    end
%           Check to see if pivot coefficient is zero
    if A(k,k) == 0
      error('Zero pivot coefficient encountered!')
    end
%           Eliminate coefficient of x(k) from rows k+1 through n
    for i = kp:n
      quot = A(i,k)/A(k,k); A(i,k) = 0;
      for j = kp:np
        A(i,j) = A(i,j) - quot*A(k,j);
      end
    end
  end
% Check to see if last pivot coefficient is zero
  if A(n,n) == 0
    error('Zero pivot coefficient encountered in last row!')
  end
% Back substitution
  x(n) = A(n,np)/A(n,n);
  for i = nm:-1:1
    sum = 0;
    for j = i+1:n
      sum = sum + A(i,j)*x(j);
    end
    x(i) = (A(i,np) - sum)/A(i,i);
  end
```

```
%%%         function btdma3.m
  function X=btdma3(A,B,C,D)
% btdma.m
% Uses decomposition to solve mxm block tridiagonal matrices of
% the form:
%                 A(i)*X(i-1) + B(i)*X(i) + C(i)*X(i+1) = D(i), i=1,2,...,n
% (Vectorized version)
%
% Input arguments:
%   A = mxmxn coefficient matrix
%   B = mxmxn coefficient matrix
%   C = mxmxn coefficient matrix
%   D = mxn matrix of rhs constants
%
% Output arguments:
%   X = mxn matrix of solution values
  m=size(A,1); n=size(A,3); mp=m+1; nm=n-1;
  E=zeros(m,m,n); F=zeros(m,n); G=zeros(m,m,n);
  X=zeros(m,n); Einv=zeros(m,m,n);
% Forward sweep
  E(:,:,1)=B(:,:,1);
  F(:,1)=D(:,1);
  for i=2:n
    im=i-1;
    Einv(:,:,im)=matinv(E(:,:,im));
    G(:,:,i)=(Einv(:,:,im)'*A(:,:,i)')';
    E(:,:,i)=B(:,:,i)-G(:,:,i)*C(:,:,im);
    F(:,i)=D(:,i)-G(:,:,i)*F(:,im);
  end
  Einv(:,:,n)=matinv(E(:,:,n));
% Backward sweep
  X(:,n)=Einv(:,:,n)*F(:,n);
  for i=nm:-1:1
    F(:,i)=F(:,i)-C(:,:,i)*X(:,i+1);
    X(:,i)=Einv(:,:,i)*F(:,i);
  end
```

```
%%%         function tdm.m
function [unknown] = tdm(A,B,C,D)
%%%%%%%%%%%%%%%%%%%%%%%%%%%%%%%%%%%%%%%%%%%
%%%         tridiagnol matrix solver        %%%
%%%%%%%%%%%%%%%%%%%%%%%%%%%%%%%%%%%%%%%%%%%
[m,n] = size(A);
        if m<n
          A = A';B = B';C = C';D = D';
          m = n;
        end
        P = zeros(m,1);Q = zeros(m,1);
```

```
unknown = zeros(m,1);
P(1,1) = -C(1,1)/B(1,1);
Q(1,1) = D(1,1)/B(1);
for i = 2:m
  im = i-1;
  den = A(i,1)*P(im,1)+B(i,1);
  P(i,1) = -C(i,1)/den;
  Q(i,1) = (D(i,1)-A(i,1)*Q(im,1))/den;
end
unknown(m,1) = Q(m,1);
for i = m-1:-1:1
  unknown(i,1) = P(i,1)*unknown(i+1,1)+Q(i,1);
end
```